Byrne *et al.*
Progress in Earth and Planetary Science (2024) 11:23
https://doi.org/10.1186/s40645-024-00627-w

Progress in Earth and Planetary Science

REVIEW

Open Access

Tectonic exhumation of a metamorphic core in an arc-continent collision during oblique convergence, Taiwan

Timothy Byrne[1*], Michael Chojnacki[1,2], Jonathan Lewis[3], Jian-Cheng Lee[4], Gong-Ruei Ho[4,10], En-Chao Yeh[5], Yuan-Hsi Lee[6], Chin-Ho Tsai[7], Mark Evans[8] and Laura Webb[9]

Abstract

Observations over the last few decades from a number of orogenic systems have highlighted the possible importance of tectonic exhumation, i.e., ductile thinning and normal faulting, in exhuming rocks once buried in high-pressure conditions. Taiwan is one of the few active orogens in the world where rocks that once experienced high-pressure metamorphism (> 50 km) are exposed at the Earth's surface, providing a natural laboratory for advancing our understanding of exhumation processes. We integrate previously published studies of the Taiwan orogen with new structural, geochronological, and fluid inclusion microthermometry data to argue that tectonic extrusion and structural thinning played a critical role in exhuming the metamorphic core of the orogen until very recently, ca. 0.7 Ma. We propose a two-stage process for exhuming the high-pressure metamorphic rocks of the Yuli Belt: an initial stage where exhumation is driven primarily by pressure gradients in a subduction channel and a second stage that is initiated as an orogen-parallel regional-scale strike-slip zone, the Tailuko shear zone, is offset by an orogen-normal strike-slip zone. The offset generates an extensional bend that is filled with extruding high-pressure rocks as the upper crust is structurally thinned. Evidence for tectonic thinning comes primarily from a low-angle penetrative foliation that records significant vertical shortening and a suite of sub-vertical late-stage, mineral-filled veins. Isotopic dating indicates that the second stage started ca. 2.4–3.1 Ma and ended at ca. 0.7 Ma when the northern Backbone Range orocline started to form. We propose the low-angle foliation formed in the footwall of a regional-scale extensional shear zone that rooted to the east, beneath the forearc. Combined tectonic and erosional processes may have limited the topographic growth of the orogen from ~3.0 to < 1.0 Ma.

Keywords Exhumation, Arc-continent collisions, Ductile thinning, Extrusion, Taiwan

*Correspondence:
Timothy Byrne
Tim.byrne@uconn.edu
[1] Department of Earth Sciences, University of Connecticut, 354 Mansfield Road, Storrs, CT 06269, USA
[2] USEngineering Solutions, Hartford, CT, USA
[3] Department of Geography Geology Environment and Planning, Indiana University of Pennsylvania, 114 Walsh Hall, Indiana, PA 15705, USA
[4] Institute of Earth Sciences, Academia Sinica, Nankang, Taipei 115, Taiwan
[5] Department of Earth Sciences, National Taiwan Normal University, Taipei 116, Taiwan
[6] Department of Earth and Environmental Sciences, National Chung Cheng University, Chia-Yi 621, Taiwan
[7] Department of Natural Resources and the Environment, Nation Dong Hwa University, Shoufeng 974, Taiwan
[8] Department of Earth and Space Sciences, Central Connecticut State University, New Britain, CT 06053, USA
[9] Department of Geography and Geosciences, University of Vermont, Burlington, VT 05405, USA
[10] Division of Geology, National Museum of Natural Science, Taichung 404023, Taiwan

1 Introduction

Geologic processes that exhume metamorphic rocks to the Earth's surface include erosion, normal faulting, and ductile deformation that thin the Earth's crust. Erosion is relatively well understood and documented in many orogenic systems worldwide and, when integrated with appropriate material flow paths in the orogen, can be the primary exhumation process (Malavieille 2010; Willett et al. 2003). Observations over the last few decades from a number of orogens have highlighted, however, the possible importance of ductile thinning and normal faulting (Platt 1993; Grujic et al. 1996; Ring and Kumerics 2008; Ring and Brandon 1999). These recent observations raise several key questions about the relative importance of tectonic versus erosional processes in orogenesis.

The orogenic belt in Taiwan is well suited to better understand tectonic exhumation because it is relatively accessible, displays both late-stage normal faults and a low-dipping ductile fabric, and is one of the few active orogens in the world where rocks that once experienced high-pressure metamorphism (> 50 km) are exposed at the Earth's surface (Jahn et al. 1981; Lan and Liou 1981; Liou 1981). The nature of on-going and rapid exhumation of the metamorphic core of Taiwan, by either erosion or structural processes, is, therefore, fertile ground for inquiry (e.g., Suppe 1981; Kirstein et al. 2009; Willett et al. 2003; Malavieille and Trullenque 2009; Dadson et al. 2003).

Here, we integrate previously published studies of the Taiwan orogen with new structural, paleotemperature, and geochronological data to argue that tectonic exhumation (e.g., extrusion and tectonic thinning) has been under-appreciated in the Taiwan orogen and propose that it played a critical role in exhuming the metamorphic core of the orogen until very recently, ~0.7 Ma. Specifically, we focus on late-stage structures generally associated with the ductile–brittle transition in the metamorphic core. The primary late-stage structures recognized in the core are a low-dipping penetrative foliation of variable intensity and mineral-filled veins (primarily quartz and calcite and locally adularia) that generally occur perpendicular to the penetrative foliation. Ductile normal-sense shear zones and normal faults lined with pseudotachylite are also included in the suite of late-stage structures associated with the ductile to brittle transition. The veins and low-dipping foliation have been recognized throughout the eastern Backbone Range, including the Tailuko and Yuli Belts and significant portions of their sedimentary covers, the Backbone Slate Belt and the Eastern Slate Belt, respectively. However, the ductile normal faults and pseudotachylite appear restricted to the northern Backbone Range. Structures that may have formed in the shallow crust (< 3–5 km) above the ductile–brittle transition, for example, joints and zones of localized brecciation or cataclasis, are not included.

We propose a two-stage process for exhuming the high-pressure metamorphic rocks of the Yuli Belt. During the initial stage, exhumation is driven primarily by pressure gradients in a subduction channel, possibly enhanced by partial subduction of continental crust. This process causes the rocks to be tectonically extruded up the subduction channel with vertical and horizontal components. The second stage is initiated as a margin-parallel, left-lateral strike-slip system is offset, forming a left-stepping extensional bend or pull-apart zone. The extruding high-pressure rocks fill this extensional zone, as the hanging wall is structurally thinned. The addition of tectonic processes in removing rock from the orogen may explain the unusually fast rates of exhumation preserved in low-temperature thermochronological data, starting at 2.5–2.0 Ma. Combined tectonic and erosional processes may have also limited the topographic growth of the orogen from ~3.0 to < 1.0 Ma.

2 Tectonic setting

The development of the arc-continent collision in Taiwan is commonly described as a propagating collision with the north-trending Luzon arc, sitting on the western edge of the PSP, as it moves toward ~315°, colliding with the ENE-trending passive margin of Eurasia (Teng 1990) (Fig. 1). These geometries and kinematics predict a southwest propagating collision (Suppe 1984), suggesting a space–time equivalence along the strike of the orogen. In this context, the orogenic system in the northeast is interpreted to be older or more mature than the southwest system. Several authors have also used this unique

(See figure on next page.)

Fig. 1 Tectonic and geologic settings of Taiwan. **A** Plate tectonic setting showing northwest convergence between the Philippine Sea and Eurasian Plates (PSP and EUR, respectively) at ~7.8 cm/yr (yellow arrow). Gray triangle in northern Taiwan shows Ryukyu block (RYUK), which is rotating CW ~47°/Myr, red arrow, based on GPS data (Rau et al. 2008). Yellow star represents subduction reversal inflection point. **B** Geologic map of Taiwan (modified from Lin and Chen 2016). Units in color are discussed in the text. Note 50° change in orientation of cleavage and 48° change in orientation of late-stage veins north of the orocline **C** relative to veins south of the orocline **D** is consistent with instantaneous CW rotation of the RYUK block and suggests rotation started ~1 Ma. OT: Okinawa Trough. RA: Ryukyu Arc. LV: Longitudinal Valley. Stereonets and all subsequent nets are equal-area, lower hemisphere projections

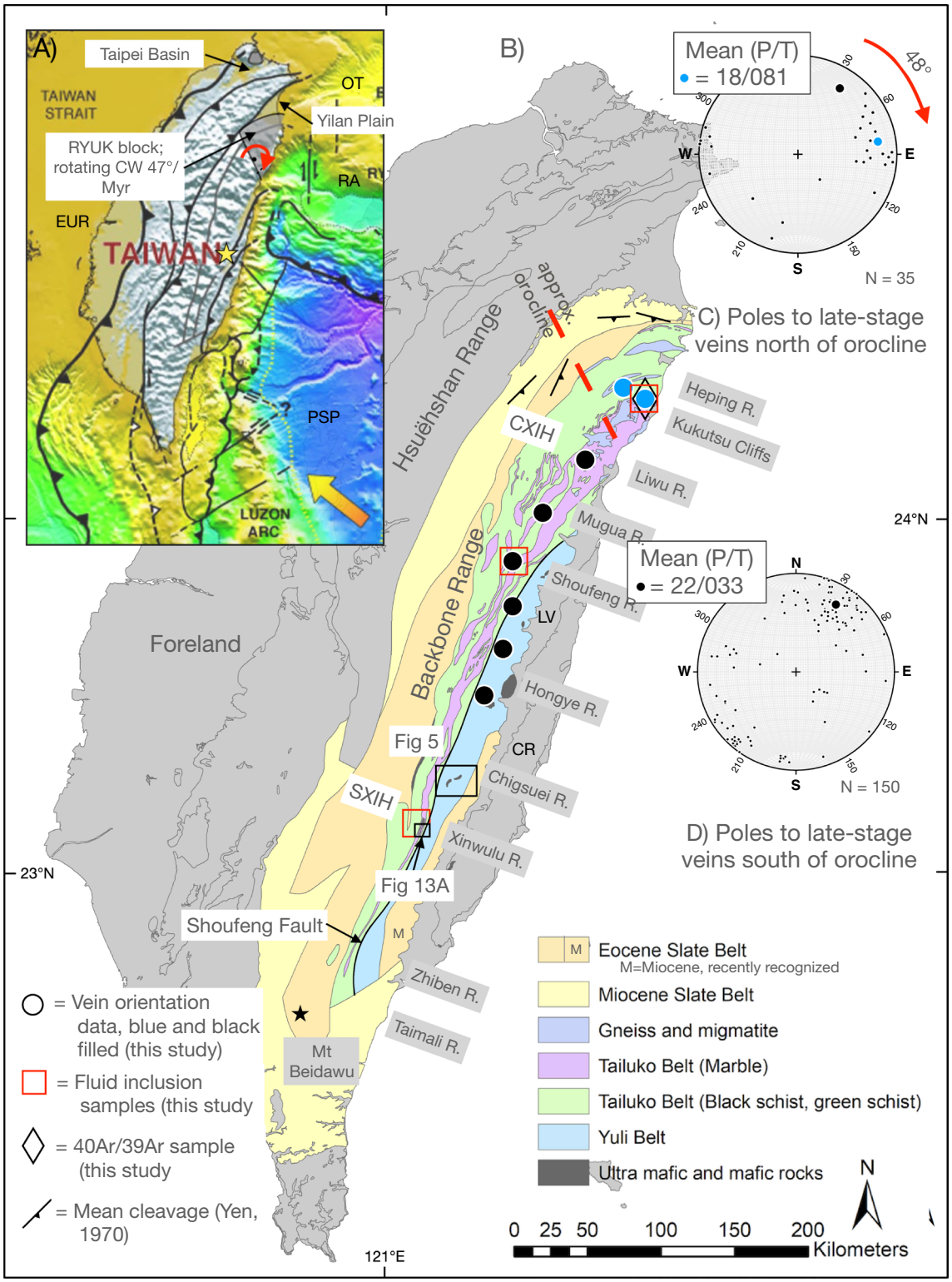

Fig. 1 (See legend on previous page.)

setting and the approximate balance between erosion and accretion to argue that the orogen has achieved a steady size and shape during the last few million years (Willett et al. 2003; Suppe 1981; Fuller et al. 2006).

However, the propagating collision model for Taiwan, interpreted from map patterns and plate kinematics, appears to mask a more complicated collision involving flipping subduction, back-arc spreading, and orogenic oroclines. For example, in the south, the Eurasian Plate dips east and subducts beneath the Philippine Sea Plate, whereas, in the north, the Philippine Sea Plate dips north and subducts beneath the Eurasian Plate and the northern Backbone Range of Taiwan. Refraction data (Van Avendonk et al. 2015; Ustaszewski et al. 2012) and the identification of subducted slabs using global tomography (Wu et al. 2016) show the Eurasian lithosphere dipping approximately 60° beneath southern Taiwan and nearly 90° beneath northern Taiwan. Patterns of seismicity and earthquake focal mechanisms in northern Taiwan also suggest that the PSP is impinging on the subducted Eurasian Plate (Lallemand et al. 1999, 2013; Ustaszewski et al. 2012). Together, these data argue for a reversal in the subduction polarity with the inflection point in central Taiwan (von Hagke et al. 2016) (Fig. 1).

The orientation of the plate boundary relative to the convergence vector also changes dramatically from south to north, adding to the complexity of the orogen. In the south, the plate boundary is at a high angle to the vector, which trends ~315°. In the north, however, the plate boundary trends east–west along the Ryukyu Arc and is at a much lower angle to the convergent vector. Subduction of the Philippine Sea Plate beneath the Ryukyu Arc has also generated back-arc spreading in the Okinawa Trough, starting as recently as 1.5 Ma (Fig. 1) (Osozawa et al. 2012; Sibuet et al. 1998, 2021). After a period of relative quiescence, ending ~1.0 Ma, extension in the back-arc propagated westward to Taiwan (Sibuet et al. 1995). This active rift forms the Yilan Plain in northern Taiwan, separating the northeasterly trending Hsüehshan Range from a more easterly trending Backbone Range (e.g., see change in strike of foliations in Fig. 1).

GPS data north and south of the Yilan Plain are also consistent with propagation of back-arc spreading between the two ranges and clockwise rotation of the northern Backbone Range, forming an active orogenic orocline (Fig. 1B) (Rau et al. 2008; Hu et al. 2002). Rau et al. (2008) used GPS data and a block rotation model (Mccaffrey 2002) to define 11 blocks in northern Taiwan, with the "RYUK" block representing the eastern limb of the orocline (Fig. 1). The block model shows the RYUK block rotating clockwise 47° +/− 7.8°/Myr. Using this modern rotation rate and the ~50° difference in strikes of the southern and northern limbs of the orocline, i.e., the central and northern extents of the Backbone Range (Fig. 1), we propose that the orocline started to form ~1.0 Ma. This age of orocline initiation is consistent with the transition from compression to extension in northern Taiwan at ~0.8 Ma (Teng et al. 2001; Lee and Wang 1988) and the initiation of sediment deposition in the Taipei Basin at 0.4 Ma, an analogous basin to the Yilan Plain (Wei et al. 1998; Teng et al. 2001).

The development of the orocline in the northern Backbone Range < 1 Ma also provides critical temporal constraints on the structural fabrics that occur within and outside of the orocline. The orocline is particularly conspicuous on regional-scale geologic maps of Taiwan, where the strike of the dominant fabric in the Tailuko Belt changes from ~020° to ~070° in the northern part of the range (Fig. 1). A low-velocity crustal root in the northern part of the range mimics the surface geology (Huang et al. 2014), suggesting that the orocline is a crustal-scale feature. In more detail, Ho et al. (2022) proposed that the dominant fabrics in the Tailuko Belt, defined by a penetrative foliation, S_2, and lineation, L_2, follow the map-scale pattern and, therefore, appear to be deformed by the orocline. This interpretation is consistent with $^{40}Ar/^{39}Ar$ ages of syn-kinematic biotite grains from a S_2 mylonite zone that range from 4.1 to 3.0 Ma (Wang et al. 1998). In the following sections, we follow a similar logic and propose that late-stage structures in the metamorphic core formed between 3.0 and 1.0 Ma because they cross-cut D_2 in the Tailuko Belt and are deformed by the orocline. For example, the orientation of late-stage veins north of the orocline axis shows an apparent clockwise rotation of 47° relative to late-stage veins south of the axis (Fig. 1).

3 Geologic background

The steady subduction of the Eurasian lithosphere beneath the Luzon Arc resulted in the progressive imbrication and accretion of rocks with oceanic and continental affinities, forming the Taiwan orogen (Fig. 1) (Ho 1988; Teng 1990). The Tailuko Belt, characterized primarily by phyllites, schists, marble, and granitic bodies, and the Yuli Belt, characterized partly by high-pressure metamorphism, represent the metamorphic core of the orogen. These belts, however, have strikingly different depositional, structural, and metamorphic histories and are separated by the enigmatic Shoufeng Fault (Fig. 1) (Yen 1963; Ho and Lo 2015). The Tailuko Belt is primarily Mesozoic and is overlain by an Eocene to Late Miocene sedimentary cover. The dominant penetrative foliation strikes parallel to the orogen and appears to display a cleavage fan with an east-dipping slaty cleavage in the west and a west-dipping crenulation cleavage in the east. In contrast, the Yuli Belt is Miocene, and its subunits,

locally mapped as members, form gently north-dipping tectonostratigraphic units with complex internal structures. The units may represent stacked thrust sheets, as they appear to pinch out in cross section or are separated by discontinuous lenses of mafic to ultramafic rocks (Lin 1999b; Tan et al. 1978). Both belts of rocks, however, display a suite of late-stage structures that appear to "stitch" the units at the time of their development.

3.1 Tailuko belt and its sedimentary cover

Previous structural studies of the Tailuko Belt and its cover, the Slate Belt of the central Backbone Range, suggested three episodes of deformation during NW-directed convergence, generalized here as D_1, D_2, and D_3 (Lin et al. 1984; Faure et al. 1991; Clark et al. 1992; Ho and Lo 2015; Stanley et al. 1981; Lu and Wang Lee 1986), although Stanley et al. (1981) recognized three additional deformation events. The early deformation episodes, D_1 and D_2 (and D_3 and D_4 of Stanley et al. 1981), included the development of an associated penetrative foliation and a variety of outcrop-scale folds interpreted to be related to the accretion of a passive margin sequence (Lin et al. 1984; Faure et al. 1991; Stanley et al. 1981). The general west dip of the dominant foliation in the eastern part of the belt also motivated interpretations of east-directed thrusting (see, e.g., Ernst 1977; Page and Suppe 1981; Faure et al. 1991). Stanley et al. (1981) elaborated on this concept and proposed that his D_3 and D_4 events formed during the development of a regional-scale, east-verging fold. Most subsequent workers followed Stanley et al. in explaining the west-dipping cleavage in the eastern part of the belt (e.g., Lin et al. 1984; Lu and Wang Lee 1986; Faure et al. 1991). In addition to the change in dip, the regional-scale fold interpretation was based on lithostratigraphic correlations that assumed a Mesozoic age for the Yuli Belt and, therefore, its approximate contemporaneity with the Tailuko Belt. Considering that the Yuli Belt is Miocene rather than Mesozoic (Mesalles et al. 2020), the lithostratigraphic correlations and regional-scale folding merit reevaluation.

More recently, Ho et al. (2022) redefined D_2 in the Tailuko Belt and documented evidence of significant regional-scale, left-lateral ductile shear. In addition, Ho et al. (2022) proposed that strike-slip deformation in the Tailuko Belt was contemporaneous with deformation in the Slate Belt, which crops out west of the Tailuko Belt and records west-directed thrusting. They propose that the two belts formed as highly oblique plate convergence was partitioned into plate-boundary parallel strike-slip in the Tailuko Belt and plate-boundary normal thrusting and imbrication in the Slate Belt to the west closer to the trench. Integrated geochronologic data suggests that partitioning was active from ca 6 to 3 Ma (Ho et al. 2022). The inactivity of D_2 in the Tailuko Belt at ~3 Ma is consistent with the initiation of the orocline in the northern Backbone Range at ~1 Ma because D_2 mylonites are rotated clockwise by the orocline.

A suite of structures that cross-cut S_2 and appear to represent a transition from ductile to brittle deformation have been recognized in the Tailuko Belt (Fig. 2) (Table 1), and a few of the studies suggest a transition from horizontal to vertical shortening. For example, outcrop-scale folds with gently dipping axial surfaces, often with a semi-penetrative, axial planar pressure solution cleavage, have been mapped along the South and Central Cross-Island Highways (SXIH and CXIH, respectively) (Clark et al. 1992; Faure et al. 1991; Stanley et al. 1981; Lu and Wang Lee 1986; Lee 1995) (Fig. 2). Lee and Yang (1994) also documented a set of late-stage quartz veins along the CXIH that record northeast-southwest extension. More recently, Ho et al. (2022) and Ho and Lo (2015) completed a detailed map of the Tailuko Belt along the Shoufeng River and showed that a gently dipping foliation cross-cuts S_2, the dominant foliation in the area, resulting in the formation of outcrop-scale recumbent folds of S_2. They also proposed that the folds and gently dipping foliation formed contemporaneously with horizontal extension. Ho and Lo (2015) labeled the foliation "S_3" (Fig. 2, Site E), consistent with previous studies of the Tailuko Belt (Clark et al. 1992; Faure et al. 1991; Lu and Wang Lee 1986; Lee 1995), excluding Stanley et al. (1981). Stanley et al. recognized three additional deformation events, and, based on their descriptions and our fieldwork along the South Cross-Island Highway, we correlate D_3, as documented by Ho and Lo (2015), to D_6 in Stanley et al. (1981).

Crespi et al. (1996) mapped suites of late-stage normal faults along the South and Central Cross-Island Highways, and showed that the faults locally involved crystal plastic and brittle deformation. Kinematic analyses yielded east–west extension along the CXIH and NE-SW extension along the SXIH (Fig. 2 Site *D* and *D'*, respectively). They also proposed that late-stage extension in the eastern Tailuko Belt along ease-dipping shear zones caused clockwise rotation of the older fabrics, providing an alternative interpretation for the cleavage fan in the Tailuko Belt.

In the northern Tailuko Belt, pseudotachylite-lined normal faults and adularia-filled veins cross-cut the dominant foliation, S_2, and record east–west extension (Korren et al. 2017; Chen et al. 2022), providing temporal and kinematic constraints on the late-stage deformation (Fig. 2, Site B). $^{40}Ar/^{39}Ar$ step-heating analyses of the pseudotachylite and adularia also yield nearly identical dates; 1.55 +/− 0.5 Ma for the pseudotachylite (Chen et al. 2017a) and 1.09 +/− 0.03 Ma and

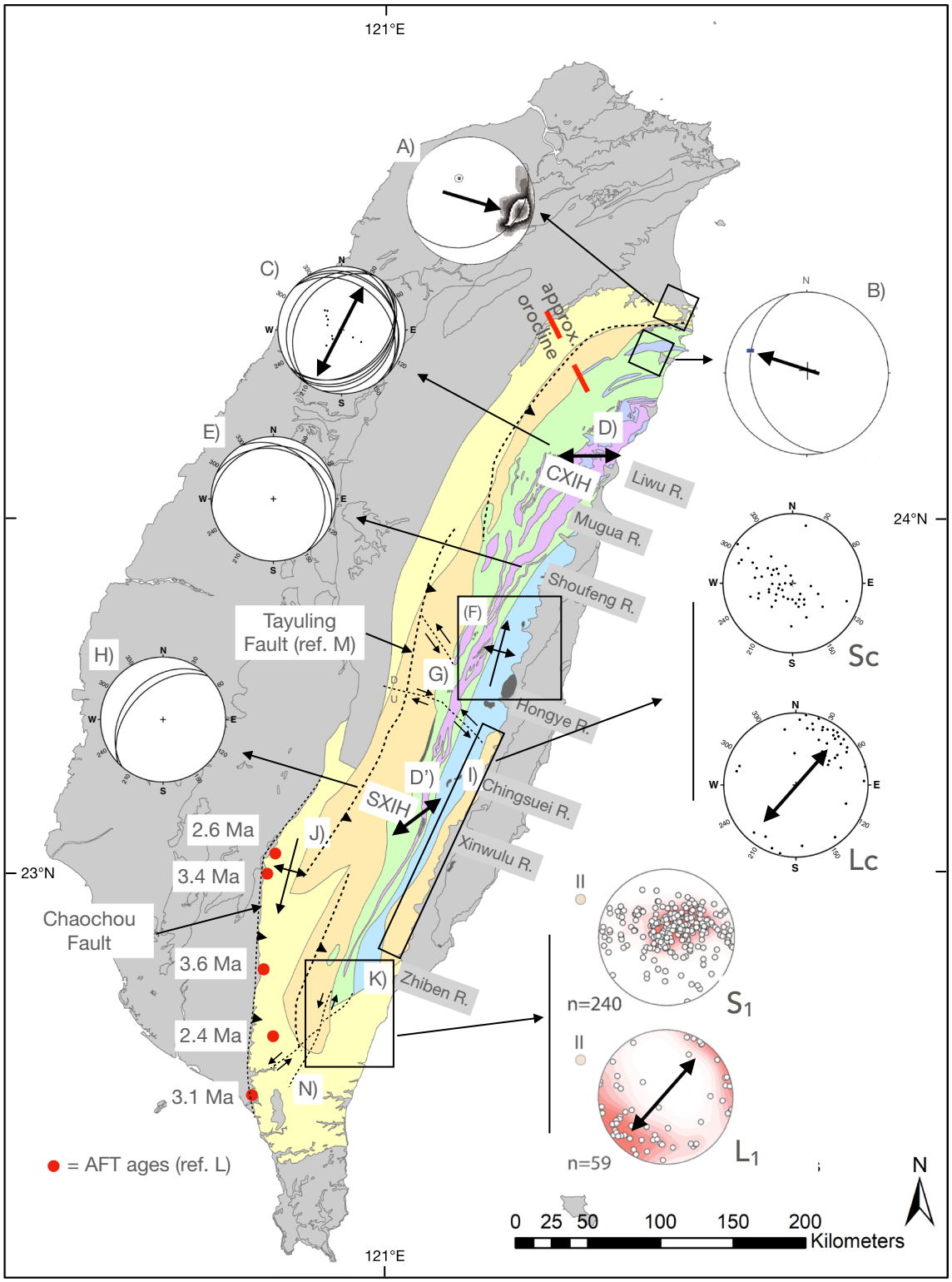

Fig. 2 Summary of previously published structural data interpreted to represent the latest penetrative event in each area. Two northern sites are on the RYUK block, which is rotating clockwise (Rau et al. 2008). Double arrows show extension or stretching directions; single arrows show motion of hanging wall. Geologic map from Chen, 2016. See Table 1 for explanations and references

Table 1 References and descriptions for Fig. 2

	References	Description
(A)	Yeh et al. (2016)	Black great circle and arrow show mean orientation of ductile shear zones and mean slip direction of hanging wall, respectively. $N = 15$. Site is on the RYUK block and is inferred to have rotated ~50° CW
(B)	Korren et al. (2017)	Black great circle and arrow show mean orientation faults lined with pseudotachylite and mean slip direction of hanging wall, respectively $N = 21$. Site is on the RYUK block and is inferred to have rotated ~50° CW
(C)	Lee (1995), Lee and Yang (1994)	Black great circle: mean orientation of late fold axial surfaces from 10 sites along Central Cross-Island Highway (CXIH) and the Tailuko coastline. Black dots: poles to F3 fold axial surfaces. $N = 66$. Black arrows: stretching direction from quartz veins. $N = 100$
(D) (D')	Crespi et al. (1996)	Black arrows: extension direction interpreted from late-stage normal faults along the CXIH and SXIH
(E)	Ho and Lo (2015)	Black great circle: mean orientation of S_3 from 3 domains along the Shoufeng River. $N = 83$
(F)	Yi et al. (2015)	Black arrow shows antiformal structure formed by S_3 in the Yuli Belt
(G)	Lin (1999a, b), Yen (1970), Lin and Chen (2016)	Short dashed lines: intraformational strike-slip faults. Left-lateral faults from Lin (1999a; b) and Lin and Chen (2016). Right-lateral strike-slip fault from Yen (1970)
(H)	Clark et al. (1992)	Black great circles: mean orientation of S_3 from 2 domains along the South Cross-Island Highway (SXIH). $N = 276$
(I)	Mondro et al. (2017)	Poles to composite foliation, Sc, and stretching lineation Lc, from Chulai and Hsinkao Formations (area in box). $N = 46$ and $N = 40$, respectively
(J)	Huang et al. (2014)	Regional-scale, late-stage antiform that deforms tectonic cleavage
(K)	Conand et al. (2020)	Poles to foliation, S_1, and stretching lineation, L_1, from sedimentary rocks south of southern most exposures of the Yuli Belt (area in box). $N = 240$ and $N = 59$, respectively
(L)	Fuller et al. (2006)	Apatite fission track ages of totally reset detrital grains; pooled ages
(M)	Lee et al. (2022a, b)	Major out-of-sequence thrust that carries the metamorphic core
(N)	Usami and Matsumoto (1940)	Late-stage left-lateral strike-slip faults on east and west sides of Tailuko Belt

1.5 +/− 0.3 Ma for two samples of the adularia (Wang 1998; Chen et al. 2022). Korren et al. (2017) estimated the formation of the pseudotachylite at a depth of > 4 km with possible temperatures ranging from 250° to 300 °C.

Further north in the sedimentary cover of the Tailuko Belt, Yeh et al. (2016) mapped a suite of late-stage, ductile shear zones with normal displacements (Fig. 2, Site A). The shear zones cross-cut ductile shear fabrics that record a left-lateral sense of shear that we suggest correlate with D_2 structures documented throughout the Tailuko Belt (Ho et al. 2022). The younger, normal shear zones also strike north–south, indicating east–west extension, consistent with the pseudotachylite-lined faults and adularia-filled veins in this area. We, therefore, propose the normal-sense shear zones (Yeh et al. 2016) formed contemporaneously with the dated extensional structures.

The suite of structures described from the northern Tailuko Belt that record east–west extension crop out in the northern Backbone Range where regional structural fabrics strike east-northeast and represent the northern limb of the Backbone Range orocline (Fig. 1). The rocks are also part of the RYUK tectonic block, which is rotating clockwise ~47°/Myr (Fig. 1, inset) (Rau et al. 2008). Considering the rate of rotation, the curvature of the orocline, and the recent onset of extension in northern Taiwan, we reconstruct these structures to their original orientations with a 47° counterclockwise vertical-axis rotation.

3.2 Yuli belt

The Yuli Belt is characterized by the abundance of metamorphosed clastic sedimentary sequences and the general absence of thick to massive marble units compared to the Tailuko Belt (Wang Lee 1979; Lin et al. 1984; Yen 1963). Tectonic or sedimentary blocks of pillowed lava, mafic and ultramafic bodies, and associated serpentinites and plagiogranites also characterize the Yuli Belt (Yui et al. 1990; Wang Lee and Lu 1984; Lin et al. 1984; Lan and Liou 1981, 1984); many of these blocks also record metamorphic conditions suggesting up to 50 km of burial (Yui et al. 1996, 2009, 2012; Huang et al. 2023; Beyssac et al. 2007; Tsai et al. 2013; Keyser et al. 2016; Baziotis et al. 2016). Early work suggested the belt was Mesozoic and possibly contemporaneous with the Tailuko Belt (Yen 1963; Stanley et al. 1981; Ho 1986, 1988). However, U–Pb ages of detrital zircons from the belt indicate a maximum depositional age of < 15.6 ± 0.3 Ma (Chen et al. 2017b). This new age is consistent with metamorphic ages from the Yuli Belt that range from 12.2 ± 0.5 Ma (Lo and Yui 1996; Chen et al. 2019) for $^{40}Ar/^{39}Ar$ ages on amphiboles to 5.1 ± 1.7 Ma for Lu–Hf ages on garnet (Sandmann et al. 2015). The high-P rocks were then exhumed to the present position starting from ~5–6 Ma (Chen et al. 2019; Huang et al. 2006; Lee et al. 2022b) and

experienced retrograde evolution as recorded by a phlogopite $^{40}Ar/^{39}Ar$ age 4.4 ± 0.1 Ma (Lo and Yui 1996) and a zircon U/Pb age of 3.3 ± 1.7 Ma from a clinozoisite vein in nephrite (Yui et al. 2014). Consequently, the Yuli Belt represents one of the world's youngest and most rapidly exhumed high-pressure belts, with exhumation rates up to 8 km/Myr.

Several field-based studies have outlined the general structural patterns in the Yuli Belt, although detailed kinematic analyses are more limited. For example, Lin et al. (1984) and Lin (1999b) proposed a tectonostratigraphy composed of four gently north-dipping units ("Members" in Lin 1999b) based on field and petrologic data from transects along the Chingsuei and Wanjung Rivers and the area north and south of the Chouchi Fault (Fig. 2, site G). Although all of the units record protracted deformation and metamorphic histories and rarely preserve stratigraphic markers, one of the structurally lowest units, a "spotted" pelitic schist interlayered with greenschists and Mn-rich garnet schists, forms a distinctive regional marker unit throughout the extent of the belt (Yen 1963; Lin et al. 1984; Lin 1999b). Blocks of metamorphosed serpentinite, epidote amphibolite, metaplagiogranite, and metamorphosed pillowed volcanic rocks are also often associated with this unit, suggesting an oceanic origin for the belt (Lin et al. 1984; Liou 1981; Lan and Liou 1984; Lo et al. 2020). Two higher structural units and one lower unit are richer in quartz, including quartz and mica-quartz schists and quartzite, and are conspicuous in the absence of exotic blocks. The proposed tectonostratigraphy is similar to the sequences observed in the Guangfu quadrangle (Yi et al. 2012) in the central part of the Yuli Belt (Fig. 2, site F).

Lin et al. (1984) also completed one of the first detailed structural studies of the Yuli Belt and recognized three deformation stages: D_1, D_2, and D_3. Each stage is associated with a suite of folds and foliations, with subsequent folding events producing distinctive interference patterns. However, none of the deformation stages in the Yuli Belt record significant evidence of left-lateral strike-slip faulting that might correlate with D_2 structures observed in the Tailuko Belt (Ho et al. 2022). Instead, the tectonostratigraphic units in the belt typically form gently, northwest to northeast dipping, structurally bound sheets, suggesting tectonic stacking. The distinctive "spotted schist" unit also appears to pinch out along and across strike (Lin 1999b), consistent with tectonic stacking. Field relations, although limited, also show the exotic blocks as lens-shaped clusters that parallel unit boundaries (Lin 1999b; Lin et al. 1984; Yen 1983; Tan et al. 1978). In some locations, however, the exotic blocks appear locally conformable with surrounding units (Lin et al. 1984) or are mapped as klippe sitting on units mapped as Yuli and the lower-grade sediments (Lin 1999b; Yen 1983).

S_3 appears to have formed relatively late in the deformation history of the Yuli Belt (Lin et al. 1984). Along the Chingsuei River, S_3 deforms S_2, creating a crenulation cleavage or outcrop-scale recumbent folds with gently dipping axial surfaces. S_3 also post-dates the growth of albite porphyroblasts and is associated with elongate quartz, suggesting more limited ductile deformation than associated with the development of S_2 (Lin et al. 1984). Mapping in the central part of the Yuli Belt shows the four tectonostratigraphic layers of the Yuli Belt forming the western half of a north plunging antiform (Yi et al. 2012), and cross sections show the dominant structural fabric, S_2, overprinted by a gently dipping cleavage interpreted as S_3 (Yi et al. 2012, 2015). S_3 also forms a broad antiformal structure that mimics the antiformal structure defined by the tectonostratigraphy, although the interlimb angle is larger, ranging from ~146° to 170° (Fig. 2, site F).

S_3 is also locally deformed by a mylonitic fabric, exposed along the western edge of the Yuli Belt in central Taiwan (Fig. 2, site F). Yi et al. (2015) completed a detailed geochronologic study across the mylonite zone using $^{40}Ar/^{39}Ar$ on fine-grained muscovite grains that form part of the mylonitic foliation and obtained six age populations ranging from 0.68 to 1.16 Ma. The youngest ages come from the middle of the mylonite zone, whereas an older age of 2.65 Ma was obtained from the Yuli Belt about 5 km east of the mylonite zone. The mylonite zone, therefore, appears to have been recently active, although the kinematics of this recent motion remain undefined. However, a late-stage normal fault (Wangwutashan Fault, Yi et al. 2015) crops out a few hundred meters west of the mylonite, suggesting the possibility that the mylonite formed during normal displacements. In any case, the mylonite deforms and locally transposes S_3 in the Yuli (Yi et al. 2015), constraining S_3 to be older than ~0.7 Ma.

Transverse strike-slip faults also developed late in the structural history of the Yuli and Tailuko Belts and may have played a role in their exhumation. For example, detailed mapping north and south of the northwest-striking Chouchi Fault (Fig. 2, site G) indicates oblique left-lateral, normal slip across the fault (Lin 1999a). Lin (1999a) interpreted the net slip to be a few km, with the northern block moving up and to the west relative to the southern block. This interpretation is consistent with observations across a geometrically similar strike-slip fault north of the Chouchi Fault (Lin and Chen 2016), suggesting that the two faults form a right-stepping, left-lateral fault system (Fig. 2) that crosses the metamorphic core of the orogen. A third transverse structure west of the Chouchi Fault strikes approximately east–west

(Fig. 2), and Yen (1970) argued for right-lateral displacement based on contrasting structural geometries on either side of the fault. The geometries and kinematics of the three faults are consistent with formation as a conjugate set during west-northwest shortening, although additional research is needed to show their contemporaneity. In any case, they document late-stage shortening and northeast elongation of the metamorphic core.

3.3 Low-grade sedimentary rocks adjacent to the Yuli belt

The low-grade metasedimentary rocks exposed east and south of the Yuli Belt also preserve late-stage structures that may correlate with structures observed in the higher-grade metamorphic rocks. These rocks were initially interpreted as Eocene (Fig. 1) (Stanley et al. 1981). Recent U–Pb analyses on samples from the northern extent of the metasedimentary rocks, mapped as the Chulai Formation (adopted from Stanley et al. 1981), however, yielded a maximum depositional age of ~11 Ma (Mesalles et al. 2020), consistent with interpretations that the Chulai was in depositional contact with the Yuli (Stanley et al. 1981). Stanley et al. (1981) also proposed that the Chulai Formation was overlain by the Hsinkao Formation south of the town of Yuli. We infer, therefore, that the Hsinkao Formation, which forms the southern extent of the metasedimentary rocks, is also Miocene.

The unconformity between the Chulai and Yuli Belt suggests the Chulai may represent a relatively low-grade sedimentary cover to the Yuli (Stanley et al. 1981), and recent mapping of the metasedimentary rocks east of the Yuli Belt suggests they form part of the Yuli Belt (Chen et al. 2017b). Detailed mapping of the unconformity along the north bank of the Xinwulu River (Fig. 1) (Stanley et al. 1981) also revealed an outcrop-scale, east-verging asymmetric fold (see Fig. 5 in Stanley et al. 1981). Although Stanley et al. (1981) related the fold to regional-scale back (i.e., east-directed) folding, the asymmetry and associated structures are also consistent with the top-to-the-east shear proposed by Crespi et al. (1996). An alternative interpretation is that the sediments east and south of the Yuli Belt represent higher structural levels of a middle to late Miocene accretionary prism (Chen et al. 2017b). We consider this possibility in more detail in the Discussion.

A quantitative strain study of 18 samples from the metasedimentary rocks east of the Yuli Belt, including the Chulai and Hsinkao Formations, shows two stretching events (Fig. 2, site I) (Mondro et al. 2017). Incremental strain histories from syntectonic fibers in strain fringes around pyrite framboids were measured relative to the orientation of the dominant cleavage, interpreted to be associated with multiple strain states, and, therefore, described as a "composite" cleavage. The composite cleavage in the belt dips gently northeast with a pi-diagram showing a broad, gently northeast plunging antiform (Fig. 2, site I). The composite lineation also plunges gently northeast parallel to the regional fold axis. Because the strain history was non-coaxial, incremental strains were measured relative to the dip of cleavage in cleavage-perpendicular sections and relative to the strike of cleavage in cleavage-parallel sections. The results show two stages of progressive extension: an early stage that is generally down dip and a later stage that is generally along strike. In geographic coordinates, the early stage of extension trends generally northwest-southeast, whereas the later extension trends northeast-southwest. Progressive finite stretch values for the late-stage extension (i.e., data collected from cleavage-parallel sections) typically range from 3 to 5, with a few as high as 14 (Mondro et al. 2017). The earlier extension stage records a slightly higher maximum stretch, ranging from 3 to 11, with a few samples below 3 and one sample recording a finite strain magnitude of 33 (Mondro et al. 2017).

One of the first detailed structural studies of the lower-grade sedimentary rocks south of the Yuli Belt suggests that they record three stages of deformation: D_1, D_2, and D_3 (Lu and Lee 2001). The two early stages of deformation are interpreted to be related to west-directed shearing followed by east-directed shearing (Lu and Lee 2001; see also Chang et al. 2009), whereas D_3 includes a gently dipping penetrative cleavage that overprints D_1 and D_2 structures. Strain fringes associated with D_1 and D_2 show a change in stretching directions from generally ENE-WSW to NNW-SSE through time (Lu and Lee 2001). A similar rotation in stretching directions, based on vein sets rather than strain fringes, is also recorded in a more limited area along the coast (Shan et al. 2014), consistent with the identification of late-stage north–south stretching in this area (Chang et al. 2009).

Finally and most recently, extensive mapping of deformation styles along the southern extent of the eastern Backbone Range, including the areas mapped by Chang et al. (2009), Shan et al. (2014), and Liu et al. (2001), suggests three structural domains with a central domain that includes the metasedimentary rocks south of the Tailuko and Yuli Belts (Fig. 2 site K) (Conand et al. 2020). The metasedimentary rocks in the central domain (Domain II of Conand et al. 2020) are characterized by gently southwest-dipping foliation and an associated down-dip (i.e., SW trending) stretching lineation (Fig. 2 site K). Extensional shear bands, S–C structures, and asymmetric pressure shadows in the central domain show increased non-coaxial strain and consistently indicate a top-to-the-SW sense of shear (Conand et al. 2020; Lu and Lee 2001).

Liu et al. (2001) also suggested that top-to-the-SW shear was associated with regional-scale left-lateral shearing.

Overall, the relation between the structures recognized by different studies in the low-grade sedimentary rocks appears complex. The rocks, however, appear to share a change from generally EW to NS stretching, a top-to-the-SW sense of shear associated with a gently southwest-dipping foliation, and a possible role for left-lateral strike-slip deformation.

3.4 Shoufeng fault

The Shoufeng fault generally represents the contact between the Tailuko and Yuli Belts (Fig. 1) but documenting and understanding the origin and slip history of the fault has been challenging. The fault is consistently recognized as a zone of concentrated strain (Stanley et al. 1981; Yen 1963; Yi et al. 2012; Yui et al. 2012; Ho et al. 2022; Chen et al. 2017b), and early work suggested that it originated as a low-angle, west-verging thrust (Stanley et al. 1981). However, the present west dip of foliations in the high-strain zone also motivated interpretations involving east-verging thrust faults (Ernst 1977; Page and Suppe 1981; Liou et al. 1977) or folds (Stanley et al. 1981; Faure et al. 1991; Lin et al. 1984). The west dip may also reflect clockwise rotations (viewing north) of an initially vertical shear zone, as proposed by Crespi et al. (1996) and Pulver et al. (2002).

Along the SXIH, detailed mapping of the boundary between the Tailuko and Yuli Belts suggests at least two stages of deformation (Stanley et al. 1981). The dominant foliation, S_2, dips moderately west and appears to correlate with the main foliation recognized throughout the Tailuko Belt (Ho et al. 2022). This foliation is typically mylonitic and associated with left-lateral strike-slip deformation (Ho et al. 2022). S_2 is cross-cut by a more gently west-dipping foliation associated with west-verging asymmetric folds. The asymmetry indicated by the folds is consistent with the proposal that the Shoufeng fault is an overturned thrust zone that, before overturning, carried the Yuli Belt westward above the Tailuko Belt (Stanley et al. 1981). The Shoufeng fault, therefore, appears to record both strike-slip and thrust deformation, at least in the exposures along the SXIH.

In central Taiwan, the Daguan shear zone dips moderately west-northwest, separating the Tailuko and Yuli Belts ("Takuan shear zone" in Yi et al. 2012)(Fig. 2 site F), and may preserve deformation associated with the Shoufeng Fault. However, the relatively young muscovite ages obtained from mylonites in the shear zone, ranging from 0.68 to 1.16 Ma, suggest, it records only the youngest stages of deformation associated with the fault. The kinematics of this recent motion and the Daguan shear zone are undefined, although the nearby Wangwutashan Fault is parallel to the Daguan shear zone and records normal displacement (Yi et al. 2012).

Finally, recent mapping and map compilations suggest that projections of the Shoufeng Fault and the left-lateral strike-slip shear zones in the Tailuko Belt are poorly constrained south of the latitude of the SXIH (Fig. 1). For example, most geologic maps show the Tailuko and Yuli Belts and the Shoufeng Fault that separates the two belts, continuing to the south-southwest, at least as far south as the Zhiben River (Fig. 1) (Ho 1988; Chen 2000; Lin and Chen 2016). However, more recent mapping shows the fault curving southeast, cutting across the low-grade sedimentary rocks to the Longitudinal Valley where the fault is apparently covered by the Quaternary sediments (Chen et al. 2017b). This interpretation suggests that the Chulai and Hsinkao Formations (Stanley et al. 1981) are part of the Yuli Belt. Similarly, recent map compilations (Lin and Chen 2016; Chen 2000) do not show two regional-scale, left-lateral strike-slip faults mapped along the east and west sides of the southern extent of the belt (Fig. 2 site N) (Usami and Matsumoto 1940). The faults appear to record several kilometers of offset (Usami and Matsumoto 1940), consistent with observations from the Tailuko Belt that show significant left-lateral shear (Ho et al. 2022). These map-scale inconsistencies related to the Shoufeng Fault and the Tailuko and Yuli Belts provide rich opportunities for future research.

3.5 Exhumation cooling of the metamorphic core

Several studies of exhumation cooling in the Tailuko Belt and its sedimentary cover suggest progressively higher exhumation rates since peak metamorphism about 6 Ma (Beyssac et al. 2007; Lee et al. 2022b; Liu et al. 2001). One of the first age-elevation profiles from the belt suggested two periods of accelerated exhumation cooling, from ~3 to 2 Ma and < 1 Ma (Liu 1982). The early cooling period is consistent with thermally reset microcline grains that yield $^{40}Ar/^{39}Ar$ plateau ages of 1.7 and 1.6 Ma (Lo and Onstott 1995). Although these studies were limited to the northern Backbone Range, four additional age-elevation profiles from along the length of the range show a broadly similar pattern with an initial acceleration in cooling at ~2 Ma and a second acceleration < 1 (Hsu et al. 2016; see also recent compilation by Lee et al. 2022b).

The early acceleration in exhumation was also confirmed through an integrated petrographic study of adjacent sedimentary basins that show sediment accumulation rates increasing at ~2 Ma (Chen et al. 2019). The second acceleration of cooling < 1 Ma (Liu 1982; Hsu et al. 2016) has also been substantiated in the northern Tailuko Belt through an additional age-elevation profile incorporating subsurface data (Shen et al. 2020).

Exhumation cooling in the Yuli Belt also appears to have been relatively rapid (Chen et al. 2017b). Although low topographic relief limits constructing age-elevation profiles, totally reset fission track and (U-Th)/He ages of detrital zircon and apatite grains from the eastern Backbone Range, including the Yuli Belt, the eastern part of the Tailuko Belt, and the metasedimentary rocks south of the Yuli Belt, are < 2.0 Myr, indicating rapid cooling very recently (see reviews by Beyssac et al. 2007; Lee et al. 2022b; Simoes et al. 2012; Fuller et al. 2006; Chen et al. 2019). These relatively young ages from multiple low-temperature geochronologic systems occur in both the Tailuko and Yuli Belts, suggesting that these belts preserve similar cooling histories since at least ~2.0 Ma (see also Chen et al. 2019).

Low-temperature geochronologic data from the southern Backbone Range south of the exposures of the Tailuko and Yuli Belts provide additional constraints on the exhumation history of the orogen. For example, Mesalles et al. (2014) took advantage of the topographic relief along the east flank of Mt Beidawu, 3091 m (Fig. 1), and constructed an age-elevation profile using partially reset and totally reset ZrnFT ages. The profile shows an acceleration in exhumation cooling at about 3.2 Ma. A more recent, integrative study that included new and previously published ZrnFT and ZrnHe data, including Mesalles et al. (2014) shows an additional acceleration at ~1.5 Ma (Lee et al. 2022a).

Two periods of accelerated exhumation are also consistent with fission track ages of totally reset detrital apatite from the southern Backbone Range. Available AFT ages, which have a lower annealing temperature than zircon for fission tracks, form two clusters generally distributed on the east and west flanks of the range (Fuller et al. 2006), excluding three older AFT ages of 27.9, 5.5, and 4.0 Ma from the southern tip where erosion has been minimal. Along the eastern flank and the Hengchun Peninsula, AFT ages range from 0.4 to 2.4 Ma, whereas along the western flank, AFT ages are slightly older, ranging from 3.6 to 2.4 Ma. The older ages on the western flank occur in the hanging wall of the Chaochou Fault (Fig. 2, Site L) (Shyu and Sieh 2005; Chen et al. 2005; Yang 1986) and cluster along the map trace of the fault. The fault is an east-dipping thrust and appears to record substantial displacement as mildly metamorphosed slates have been thrust west over Holocene alluvium of the Pingtung Plain (Liu et al. 2009). The limited age range and the distribution of samples in the hanging wall of the thrust suggest the Chaochou was active at about 3.6–2.4 Ma, which coincides with the time of accelerated exhumation cooling in the rocks east of the fault (Mesalles et al. 2014). The cluster of younger apatite ages along the eastern flank may reflect the acceleration in exhumation at ~1.5 Myr proposed by Lee et al. (2022b), which is based primarily on ZrnHe ages of detrital zircon.

4 Methods

4.1 Field data and structural analyses

Our field studies focused on the outcrops previously mapped as the Yuli Belt. However, we also completed reconnaissance excursions in the adjacent Tailuko Belt and the sedimentary cover sequences associated with these belts. Our goals in the Tailuko Belt were to confirm the presence and geometry of the youngest foliation, typically "S_3" in this belt, identify additional late-stage structures associated with the ductile to brittle transition, and collect samples of vein materials for fluid inclusion and dating analyses.

Structural data and samples were collected primarily during four field campaigns in January 2018, July 2018, January 2020, and April 2021. The January 2018 trip was focused on the Dalun River, near its junction with the Xinwulu River. The campaign in July 2018 sampled seven river sites, encompassing over 100 km along the trend of the orogen (Fig. 1), whereas the January 2020 trip was a reconnaissance trip along short stretches of the South Cross-Island Highway, the Heping River, and the Kukutsu Cliffs (Fig. 1). The April 2021 campaign included an eight-day campaign along the lower reaches of the Chingsuei and reconnaissance trips to the Taimali and Zhiben Rivers in southern Taiwan. Fieldwork included making detailed observations of mesoscopic structures and lithologies, collecting structural data (e.g., foliations and lineations), and collecting oriented samples for microscopic analysis.

Field sites were along river systems due to the thick vegetation cover and rugged topographic relief. The island straddles the Tropic of Cancer, and the summer monsoons produce a thriving and diverse biosphere and a thick jungle cover. However, river channels are often sinuous and produce polished exposures of the metamorphic basement rock with both along-strike and cross-strike views. River sites studied here are shown in Figs. 1 and 2.

Correlating a penetrative fabric or deformation event across different lithostratigraphic and tectonostratigraphic units is also challenging (Tobisch and Paterson 1988). These challenges are particularly acute in highly sheared rocks, e.g., S–C mylonites and phyllonites, where multiple foliations can be generated during a single deformation event. The late-stage veins, however, are a common and relatively conspicuous feature in essentially all units studied and, in most cases, led to the identification of additional late-stage structures. At some outcrops, when the number of earlier foliations could not be easily determined, the late-stage structures were tagged

preliminarily as part of Dy (for $Deformation_{youngest}$), with Sy representing the youngest foliation and Ly representing the youngest lineation. We then integrated previous work with the new observations and developed a deformation history for each unit to provide context for the late-stage structures. In most cases, the deformation stages and fabric classifications developed by previous workers were maintained, although this resulted in inconsistent subscripts for the youngest fabric across different units. To resolve these inconsistencies, we propose an accretionary prism model where more deeply buried rocks that may record multiple deformational "events" are juxtaposed next to rocks that are accreted at shallower structural levels that record only the youngest deformational event. We also propose a new deformational event and fabric that appears limited to the Tailuko Belt and the western part of the Yuli Belt near the Tailuko.

Additional details on sample collecting and field and petrographic analyses are provided in Additional file 1: Appendix SI.

4.2 Fluid inclusion microthermometry

Samples used for fluid inclusion microthermometry (FIM) were sourced from three localities representative of the metamorphic basement (red squares, Fig. 1). The northern site is in the Tailuko Belt and is exposed along the Kukutzu Cliffs, Hualien County. The central site is located in the Yuli Belt along the lower reaches of the Shoufeng River. The southern site was situated along the Xinwulu River in the eastern Tailuko Belt, near the contact with the Yuli Belt. Specimens were late-stage veins or single euhedral crystals 1–4 cm in length. Doubly polished thin sections of four quartz crystals and one adularia crystal were produced for petrographic and microthermometric analysis.

A detailed description of the methods used for fluid inclusion microthermometry, including preparation of doubly polished thick sections, is in Additional file 2: Appendix SII.

Once constructed, the thick sections were photographed at low magnification (0.5–4X) and examined for usable fluid inclusions. The fluid inclusion section is then broken into small pieces required for microthermometric measurements, as described by Touret (2001). A delineation of the broken fragments as well as other thermometric data can be visualized on the fluid inclusion map. The map is required to reconstruct the broken fragments in their original position for later SEM-CL analysis. Within each individual chip, fluid inclusion assemblages were classified as primary, secondary, or pseudosecondary. An ideal area of interest was chosen to collect the microthermometric data based on the number and clarity of fluid inclusions in the field of view. Detailed sketches were produced depicting individual fluid inclusions within the area of interest (Shepherd et al. 1985; Touret 2001). Before the heating and cooling experiments were performed, observations of the fluid inclusions were recorded at standard temperature and pressure: the size and shape of the inclusion, the number of type of phases present, and the $L{:}V$ ratio, percent vapor bubble, or degree of fill (Shepherd et al. 1985).

4.3 $^{40}Ar/^{39}Ar$ dating

$^{40}Ar/^{39}Ar$ analyses were performed at the University of Vermont Noble Gas Geochronology Laboratory. Mineral separates were loaded into aluminum foil packets, arranged in a suprasil vial, and placed in an aluminum canister for irradiation. Samples were irradiated at the Oregon State University Radiation Center in the CLOCIT facility for 18 h with multigrain aliquots of Fish Canyon Tuff Sanidine to act as a flux monitor (28.201 ± 0.046 Ma; Kuiper et al. 2008). Laser step heating for $^{40}Ar/^{39}Ar$ dating was conducted with a Santa Cruz Laser Microfurnace 75W diode laser system. Three aliquots of adularia from sample T19HC-01, one crystal each, were loaded directly into wells in a copper sample holder. The gas released during heating was purified with SAES getters, and argon isotopes were analyzed on a Nu Instruments Noblesse magnetic sector noble gas mass spectrometer in peak-hopping mode during step-heating analyses. Data from samples and flux monitors were corrected for blanks, mass discrimination, atmospheric argon, neutron-induced interfering isotopes, and the decay of ^{37}Ar and ^{39}Ar. Correction factors used to account for interfering nuclear reactions for the irradiated samples are from Rutte et al. (2018). Decay constants are from Min et al. (2000) and Stoenner et al. (1965). Mass discrimination was calculated by analyzing known aliquots of atmospheric argon for which the measured $^{40}Ar/^{36}Ar$ value was compared with an assumed atmospheric value of 298.56 (Lee et al. 2006). A linear interpolation was used to calculate J factors for samples based on sample position between flux monitor packets in the irradiation tube. The data analyses were achieved using both an in-house data reduction program and Isoplot 3.0 (Ludwig 2003).

4.4 Strain

We have taken multiple approaches to understanding the strain and strain histories of the youngest deformation, although the difficult access to outcrops limited systematic analysis. At the broadest scale, the orientation of the youngest penetrative fabric and associated late-stage veins consistently show vertical shortening and subhorizontal extension throughout the metamorphic core. The high angle between veins and the youngest foliation

(~90°), and the limited dispersion of the vein orientations also argue for vertical thinning and a low degree of non-coaxial strain (kinematic vorticity < 1.0). Observations of structures in sections parallel to the principal strain axes (i.e., X, Y and Z) provide additional constraints on the kinematics. For example, structural data from a deformed pebble conglomerate along the Mugua River and an extensive exposure of phyllonite along the Chingsuei River provide a preliminary deformation history for the Yuli Belt and, therefore, context for the late-stage structures. Finally, we integrate these new results with a previously published study of the finite and incremental strain histories in the Yuli Belt sedimentary cover, mapped as the "Eastern Slate Belt" (Mondro et al. 2017).

5 Results

Structural mapping of the metamorphic core focused primarily on transects across the Yuli Belt, although reconnaissance studies were also completed in parts of the Tailuko Belt and the lower-grade sedimentary sequences interpreted to represent higher structural levels of the metamorphic rocks. We start with field studies of the lower-grade sedimentary rocks, one from the area of Zhiben River and the second along the eastern Chingsuei River. Four additional but more limited studies focus on the higher-grade rocks exposed along the middle and western reaches of the Chingsuei River and along short sections of the Hongye and Mugua Rivers (Fig. 1). We also re-examined rocks along the Dalun River that expose the Shoufeng fault and rocks along Heping River and Kukutus cliffs where late-stage structures have been dated isotopically. Structural data collected during more limited studies along the Fuyuan, Matian, and Shoufeng Rivers are also included in our compilation. Despite the differences in their structural complexity, the unifying theme of these areas is the apparent progression from west-northwest-directed thrusting and penetrative stretching to northeast extension. Integration of our studies with the available literature suggests that the late northeast extension event is characterized by (1) a low-dipping pressure solution cleavage, (2) mineral-filled veins that formed late in the development of the pressure solution cleavage, and (3) a weak to moderately developed stretching lineation that is generally perpendicular to the veins. The general aspects of these characteristic structures are discussed after the site-specific descriptions.

5.1 Zhiben River

Observations along the Zhiben River, south of exposures of the Yuli Belt (Fig. 1), reveal a relatively mildly deformed sequence of sandstones and shales. Sandstone layers often grade upward from coarse-grained sands to fine, laminated, or convoluted layers, consistent with turbidite deposition. Soft-sediment deformation consisting of slump-like structures, similar style folds, suggesting high ductility, debris deposits that include sections of overturned bedding (e.g., Fig. 3), and isolated fold hinges are also relatively common. The soft-sediment structures are cross-cut by a weak to moderately developed pressure solution cleavage that dips steeply to gently east (Fig. 4). Only one penetrative foliation, S_1, was recognized in this area, consistent with the more regional study by Conand et al. (2020) (Fig. 3C). At one locality along the river's north bank, sandstone layers form a northwest-verging asymmetric fold with the pressure solution cleavage forming an axial planar foliation. Graded bedding (Fig. 3A), however, shows the layers are upside-down with layering in the short limb facing east-southeast rather than west-northwest in the direction of fold vergence. One interpretation is that the outcrop represents the overturned limb of a larger regional-scale fold. The fold asymmetry and cleavage dip suggest a downward-facing, east-dipping, overturned antiform. Alternatively, overturning of the sedimentary units may have occurred before folding and cleavage development. In fact, Pelletier and Hu (1984), Lu et al. (2001) and Chang et al. (2007) have mapped overturned sedimentary units of a similar scale in the area of the Taimali River and argued they had a sedimentary origin. Our observations are consistent with this interpretation.

Kinematics of the asymmetric folds exposed along the Zhiben River can be inferred from the trend of associated fold axes, the dip direction of the axial planar cleavage, and the trend of fibrous strain fringes around rigid objects (probably diagenetic pyrite) (Figs. 3, 4). The fold axes suggest movement to the northwest, whereas the cleavage generally dips east, suggesting a more westerly motion. Strain fringes exposed along the plane of cleavage trend east-northeast to west-southwest, oblique to the movement directions inferred from the dip of cleavage and the fold axes. Conand et al. (2020) also recognized a similar pattern of northeast-trending stretching oblique to the trend of measured fold axes, with a significant portion of the data showing overlapping trends (Fig. 3B, C). They proposed that folding and stretching developed contemporaneously in a left-lateral wrenching environment during oblique convergence (see also Lu and Lee 2001).

5.2 Eastern Chingsuei River and highway 30

Further north, along the north bank of the Chingsuei River and along Highway 30, near the junction with the Lakulaku River (Fig. 5), historical outcrops of the Miocene Chulai Formation initially exposed two decimeter-scale west-to-northwest-verging asymmetry folds similar

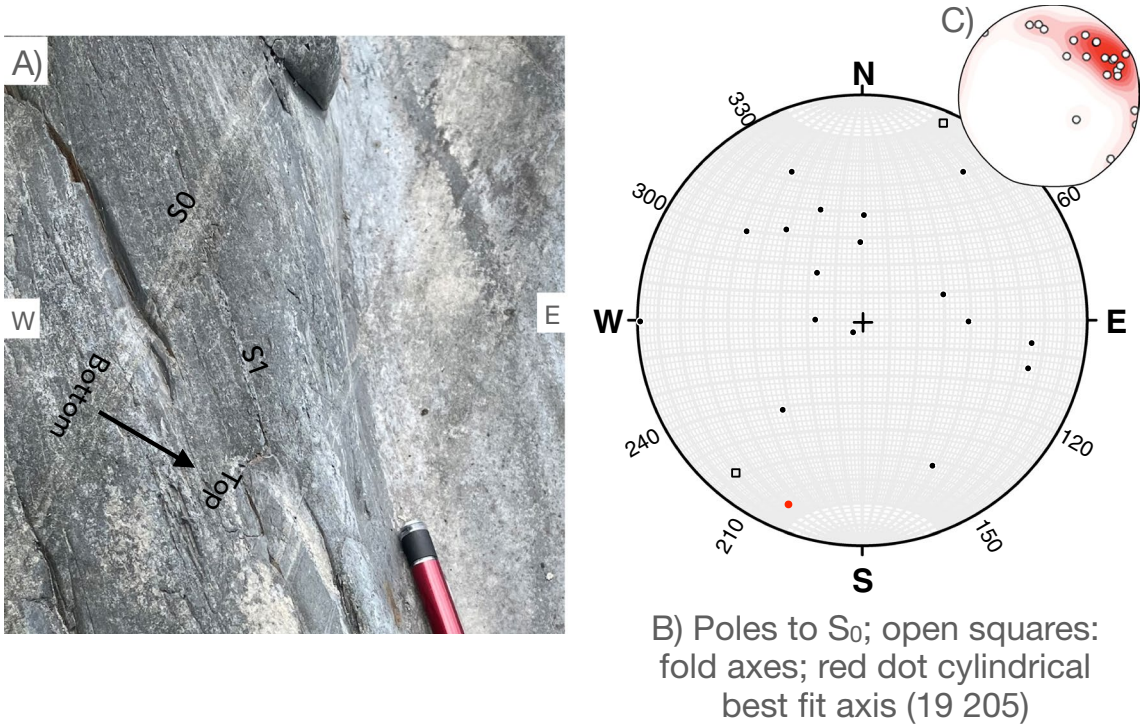

Fig. 3 Outcrop photograph and orientation data from sedimentary rocks along the Zhiben River interpreted to represent higher structural levels of the Yuli Belt. **A** Photograph of cleavage, S_1, dipping east and overturned bedding, S_0, dipping west. **B** Poles to bedding ($n = 16$), cylindrical best fit of bedding, and fold axes ($n = 2$). **C** Fold axes from Domain II of Conand et al. (2020)

to the fold along the Zhiben River. Unfortunately, the fold along Highway 30 that showed clear asymmetry has been covered with concrete and is no longer available for observation. Graded bedding in the inferred short limbs of both folds also shows(ed) younging to the east rather than to the west (Fig. 6), suggesting that the beds were overturned before folding, consistent with observations along the Zhiben River. The top-to-the-west shear is also consistent with outcrop observations in the Chulai Formation to the west (see below). However, the fold asymmetry of the preserved fold along the Chingsuei River (Fig. 6) is less clear than for the concrete-covered fold, allowing alternative interpretations. For example, if the beds were not overturned before folding, the east-facing bedding on the Zhiben River may reflect clockwise rotation associated with top-to-the-east shear.

A few 100 m west of the fold described in Fig. 6, a low-dipping phyllonite is exposed and S–C fabrics confirm the top-to-the-west motion inferred from the asymmetric folds (Fig. 7). The "C" surfaces dip gently east and are approximately parallel to lithologic layering, making it impossible to identify primary sedimentary layering in this area. The "S" surfaces also dip east but at a steeper angle, indicating a top-to-the-west sense of shear (Fig. 7B, C). The S surfaces are locally associated with west-verging folds of C surfaces or "P" shears consistent with west vergence. Multiple S and C surfaces, P shears, and locally extensional shear bands result in an irregular or wavey fabric at an outcrop scale.

The decimeter-scale west-verging folds and the S–C phyllonites in these two areas are cross-cut by a more planar foliation that dips gently northeast (Fig. 8) and appears undeformed by the S–C fabrics. The cross-cutting relations, however, are more conspicuous in the steeply dipping limb of the fold where lithologic layering is at a high angle to the younger fabric. One of the late foliation surfaces also exposes an elliptically shaped reduction halo with its long axis parallel to a weak mineral lineation in the cleavage plane (Fig. 8). Relatively undeformed to mildly deformed quartz veins are also present in this area of the Chingsuei River and show northeast extension (Fig. 8) parallel to the long axis of the reaction halo and mineral lineation.

The decimeter-scale fold and the phyllonites pre-date the low-dipping foliation and primary sedimentary structures in the steep limb of the fold suggests little deformation occurred before folding. We, therefore, interpret the fold and S–C phyllonites as D_1 structures and the

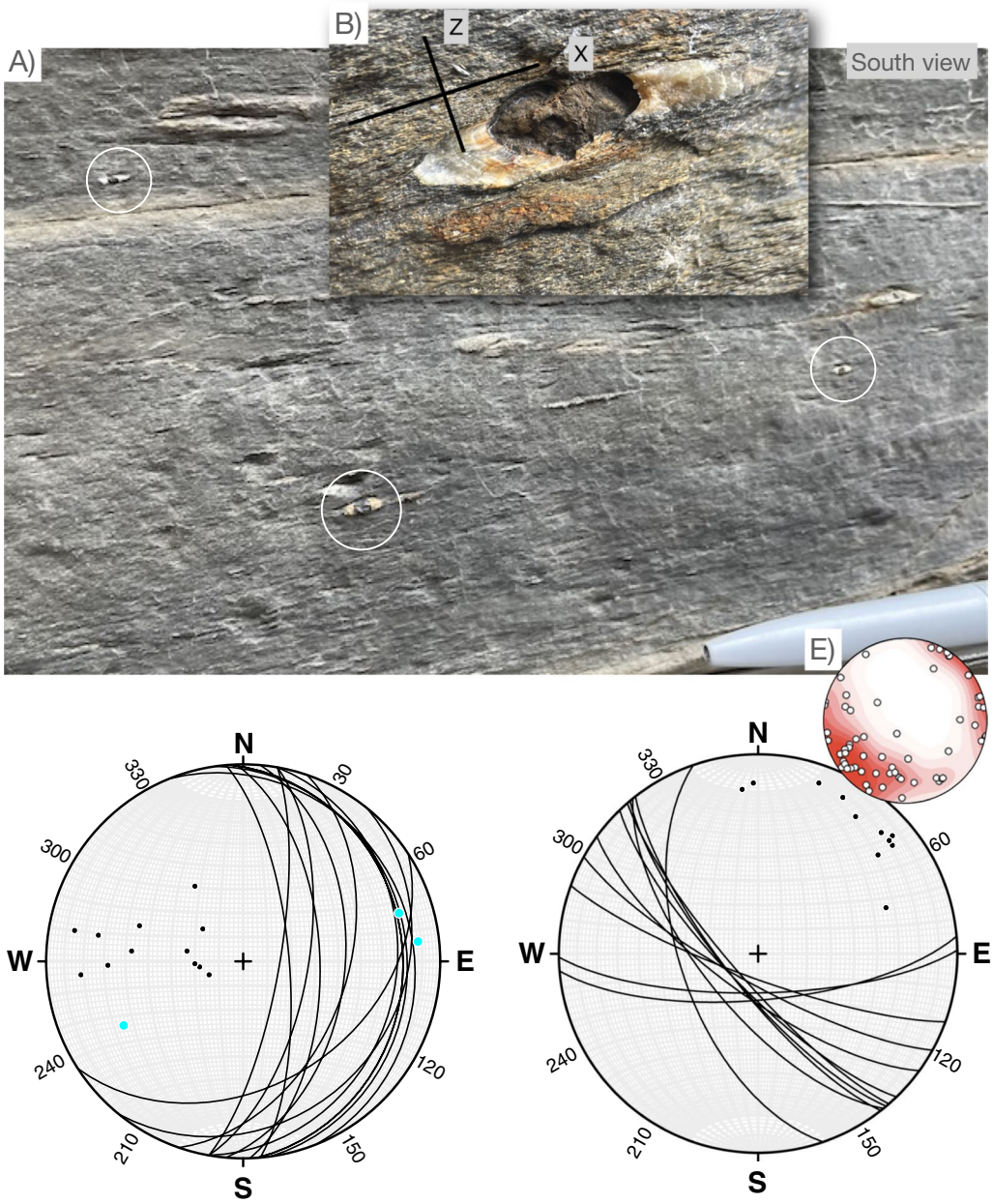

Fig. 4 Photographs of S_1 in sedimentary rocks along the Zhiben River. **A** and **B** are approximately parallel to the *XZ* plane of the strain ellipsoid inferred from strain fringes around pyrite framboids. Framboid diameters average about 0.5 cm. Enlarged framboid and fringe **B** suggest finite stretch (1 + e1) of 3.5. **C** Orientation data for S_1 (planes and poles) stretching lineation from strain fringes. **D** Orientation data for late-stage veins (planes and poles). **E** Orientation data for stretching lineations from Conand et al. (2020)

low-dipping foliation and late-stage veins as representing D_2. This interpretation is consistent with Lin et al. (1984), who proposed that the Chulai Formation recorded two deformation events.

5.3 Middle and western Chingsuei River sites

Further west, more limited studies along the middle and western sections of the Chingsuei River (Fig. 5) reveal excellent exposures of zones of relatively high strain in the Yuli Belt (see, e.g., photographs in Figs. 9, 11). Rocks

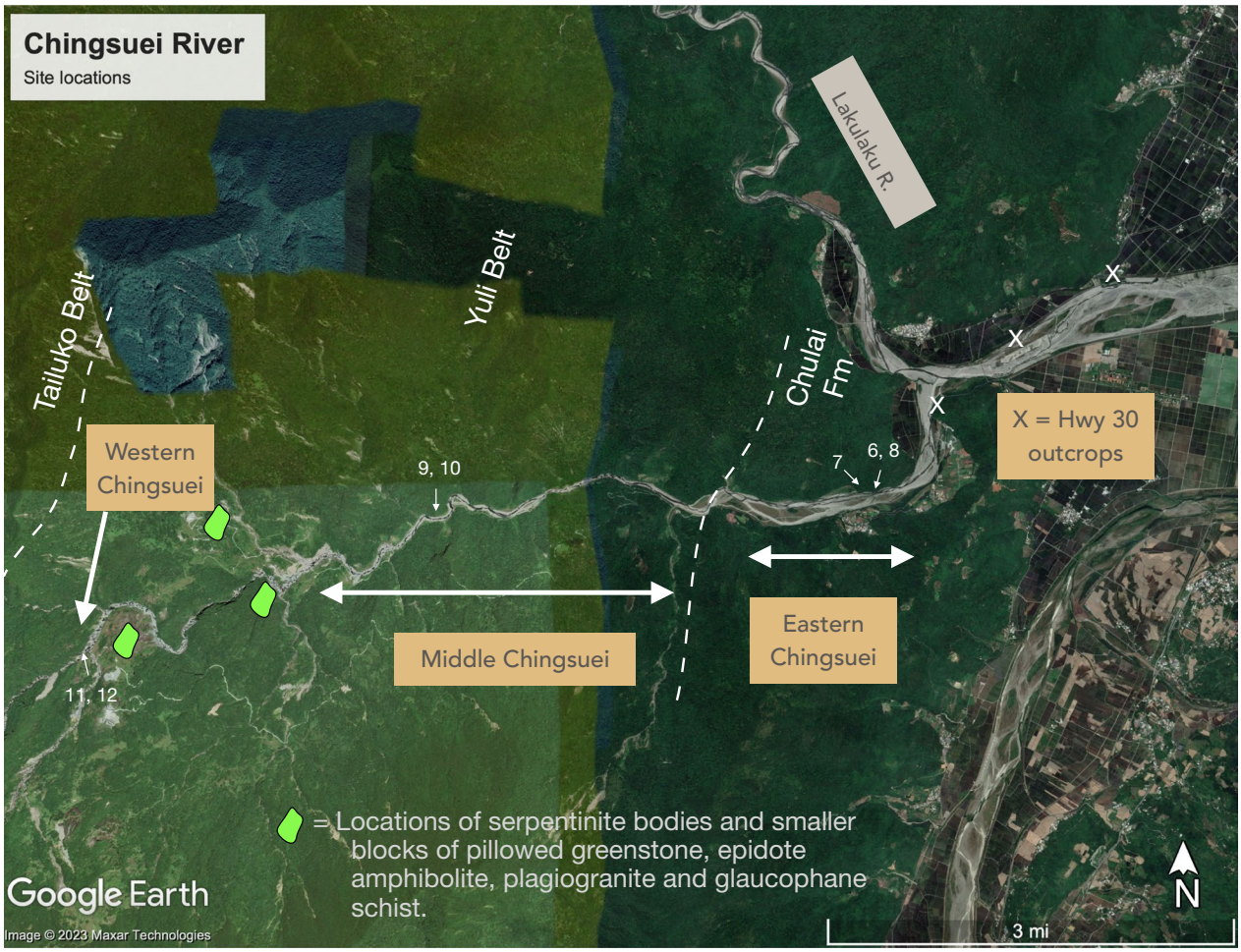

Fig. 5 Location of focus areas along the Chingsuei River. See Fig. 1 for location and text for discussion. Numbers refer to Figure locations; "*X*" to outcrops along Hwy 30

along the middle Chingsuei River comprise alternating layers of quartz-rich and quartz-poor metamorphosed sediments, typical of the Luntienshan member of the Yuli Belt (Lin et al. 1984). However, primary sedimentary structures are completely obliterated, and the outcrops are often dominated by highly strained sedimentary rocks with lenses and stringers of quartz that probably represent early quartz veining. Most of the lenses of quartz have a symmetric shape with respect to the main foliation. However, isolated hinges of isoclinal folds are not uncommon, and a few hinges are suggestive of asymmetric folds (Fig. 9). The isolated hinges are interpreted to be remanent of an earlier foliation, making the main foliation in the outcrop S_2. One elliptical lens of quartz is oriented at an oblique angle to the S_2, suggesting a clockwise rotation, viewed to the north, and a top-to-the-west sense of shear (Fig. 9C). S_2 in these outcrops is also deformed by a set asymmetric folds and an associated spaced crenulation cleavage (Fig. 9). The axial surfaces and cleavage dip moderately east and the fold asymmetries consistently indicate a top-to-the-west sense of shear. Based on cross-cutting relations and relations across Fig. 10A (e.g., western Chingsuei River) and along strike (e.g., Dalun River), we interpret this younger crenulation cleavage to represent S_3.

Exposures along the western Chingsuei River comprise relatively thick quartz- and feldspar-rich metamorphic rocks, including a Mn-rich garnet schist often found in the Chingsuei Planation member of the Yuli Belt (Lin et al. 1984). Like the exposures along the middle Chingsuei River, the units are intensely deformed, with quartz-rich rocks approaching mylonites (Fig. 11A) and quartz-poor rocks displaying phyllonitic textures. However, the main foliation dips steeply to moderately west, in contrast to the foliation in the middle Chingsuei River (Fig. 11B). As in the middle Chingsuei, S–C shear structures suggest a top-to-the-west sense of shear. The main foliation is also deformed by a set of asymmetric

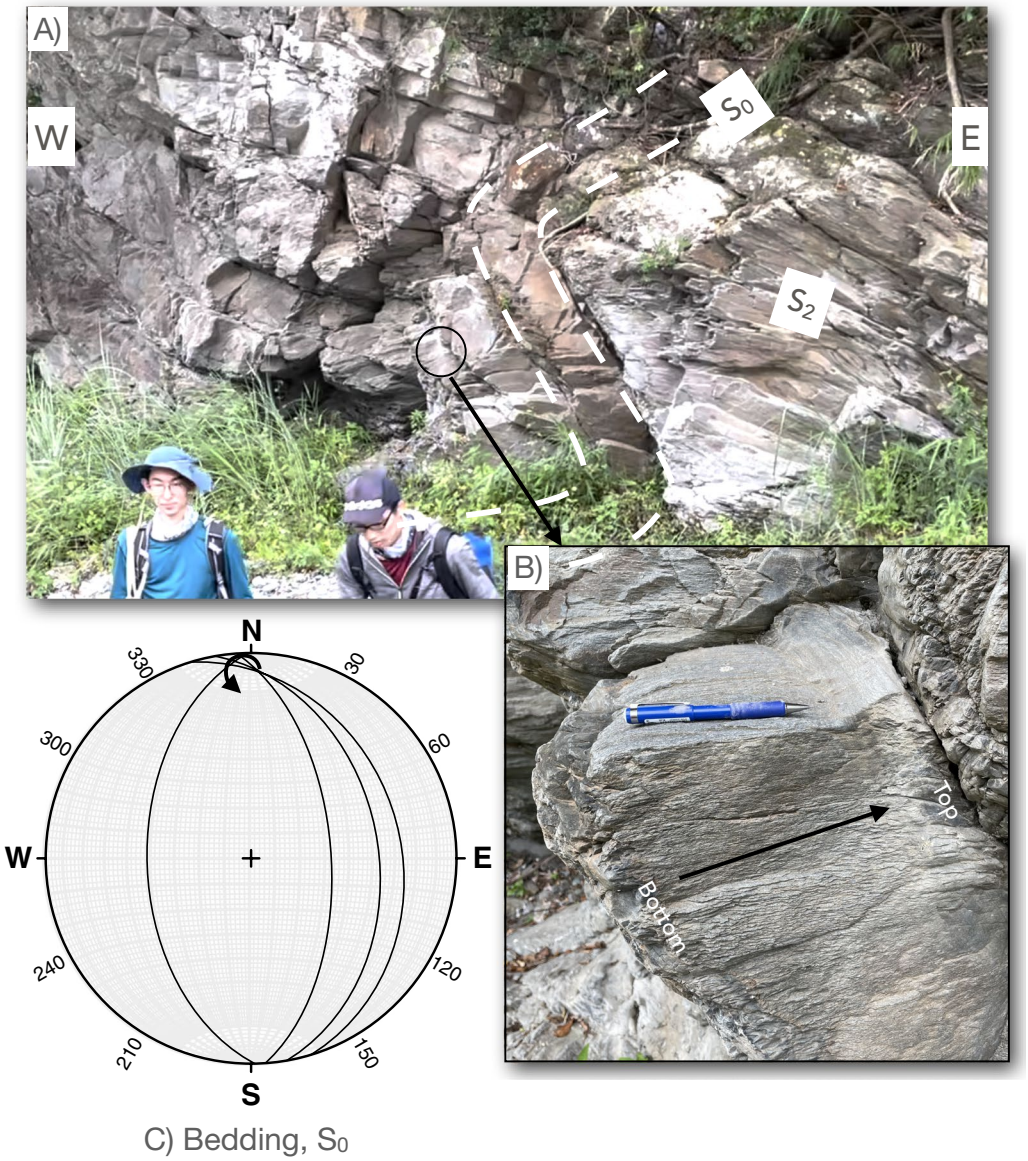

Fig. 6 Outcrop photographs and orientation data for S_0, and S_2 from the Chulai Fm along the north bank of the eastern Chingsuei River (see Fig. 5 for location). **A** Photograph of a recumbent, east-facing syncline and axial planar foliation, interpreted to be S_2. East-facing bedding may reflect CW rotation of upright beds during top-to-the-east folding or CCW rotation of overturned beds during top-to-the-west folding. **B** Inset of **A** shows bedding facing east. **C** Orientation of bedding and interpreted fold axis. Curved arrow shows one interpretation for sense of rotation during folding. See text for discussion

folds that typically have relatively gentle to open interlimb angles. In some cases, the interlimb angle decreases substantially as the amplitude of the fold increases, producing tight to isoclinal folds and suggesting progressive shear approximately parallel to the axial surface (Fig. 11A). The folds consistently verge to the west (i.e., west-side-down) and, based on cross-cutting relations and observations a few km along strike (i.e., Dalun River, discussed below), we interpret this later deformation to D_3 and label associated folds and associated foliations, F_3 and S_3, respectively.

The eastern, middle and western sections of the Chingsuei also display differences in the dip direction of the dominant foliation, typically lithologic layering which is subparallel to "C". Along the eastern Chingsuei the dominant fabric dips northeast (Fig. 7B), whereas along the middle Chingsuei, the dominant fabric dips north gently (Fig. 10A), and along the western Chingsuei, the

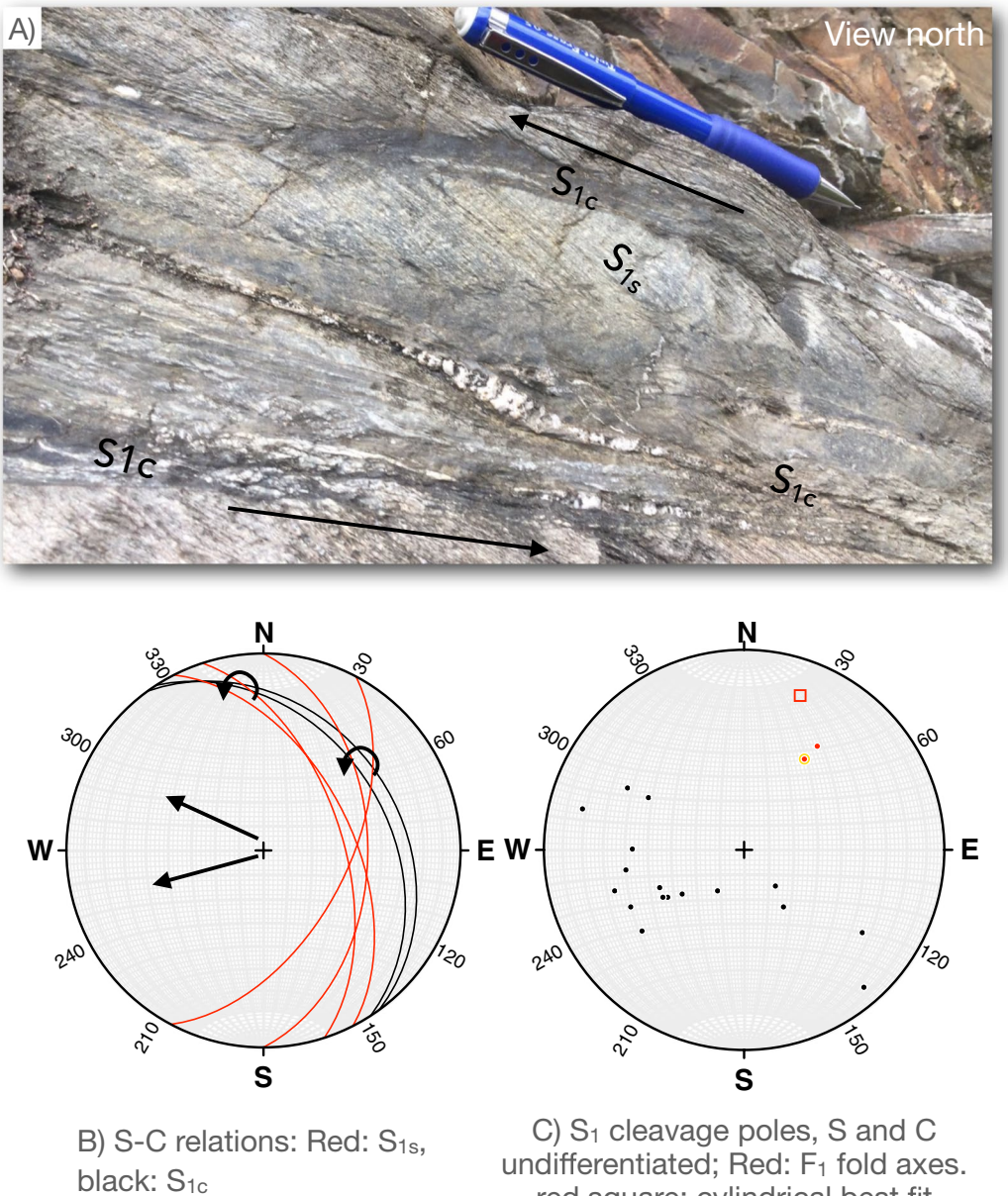

Fig. 7 Outcrop photograph of S–C phyllonite in the Chulai Fm along the north bank of the eastern Chingsuei River. This location is west of Fig. 6 and may represent a transition from the Chulai Fm to the Yuli Belt. See text for discussion. Sense of shear inferred from the S–C mylonite fabric shown with two opposing arrows. **B** S–C relations with curved arrows showing sense of rotation. **C** S_1 and S–C planes, undifferentiated

dominant fabric dips west or northwest steeply (Fig. 11B). This regional-scale change in dip direction across strike suggests a regional-scale antiform. The middle and western sections also crop out on the east and west sides, respectively, of relatively large bodies of serpentinite and smaller blocks of pillowed greenstone, epidote amphibolite, plagiogranite, and glaucophane schist (Fig. 5), consistent with an antiform. East–west cross sections constructed by Lin et al. (1984) and Lin (1999a) also show an antiformal structure centered on the middle and western sections of the Chingsuei. A similar north–northeast-trending antiform occurs along strike in the Yuli Belt (Yi et al. 2012) (Fig. 2 site F). However, the data from the western Chingsuei site is constrained by only two foliation data points (Fig. 11B). Without facing indicators, we are also not able distinguish between a regional-scale antiform or an overturned, east-facing synform between the middle and western Chingsuei sites. The exposures

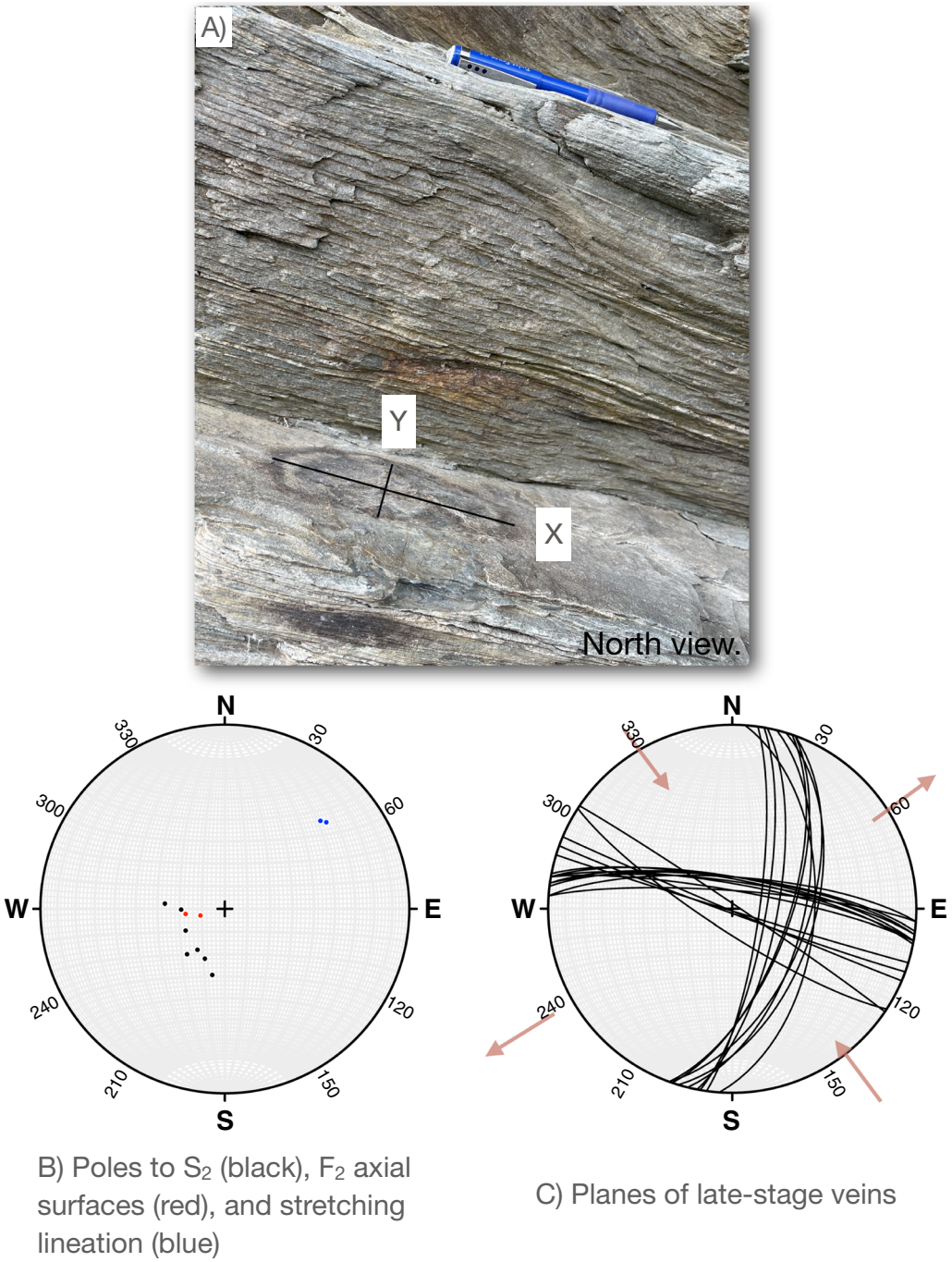

Fig. 8 **A** Outcrop photograph of a stepped exposure that provides an oblique view (lower) and profile view (upper) of S_2. The oblique view includes a reduction halo on S_2. Long and intermediate axes suggest a finite stretch (1 + e1) of 3.0. **B** Orientation data for S_2, F_2 axial surfaces, and L_2. **C** late-stage veins; brown arrows show interpreted kinematic axes based on observed slip-along veins

along the western Chingsuei near the trace of the Shoufeng fault may have also been rotated CW (viewed north) as proposed by Crespi et al. (1996) for rocks along the SXIH and CXIH.

Finally, the penetrative foliations exposed along both the middle and western sites, S_2 and S_3, are cross-cut by mildly deformed quartz and calcite-filled veins that dip steeply southwest (Figs. 10C, 12C) and are slightly

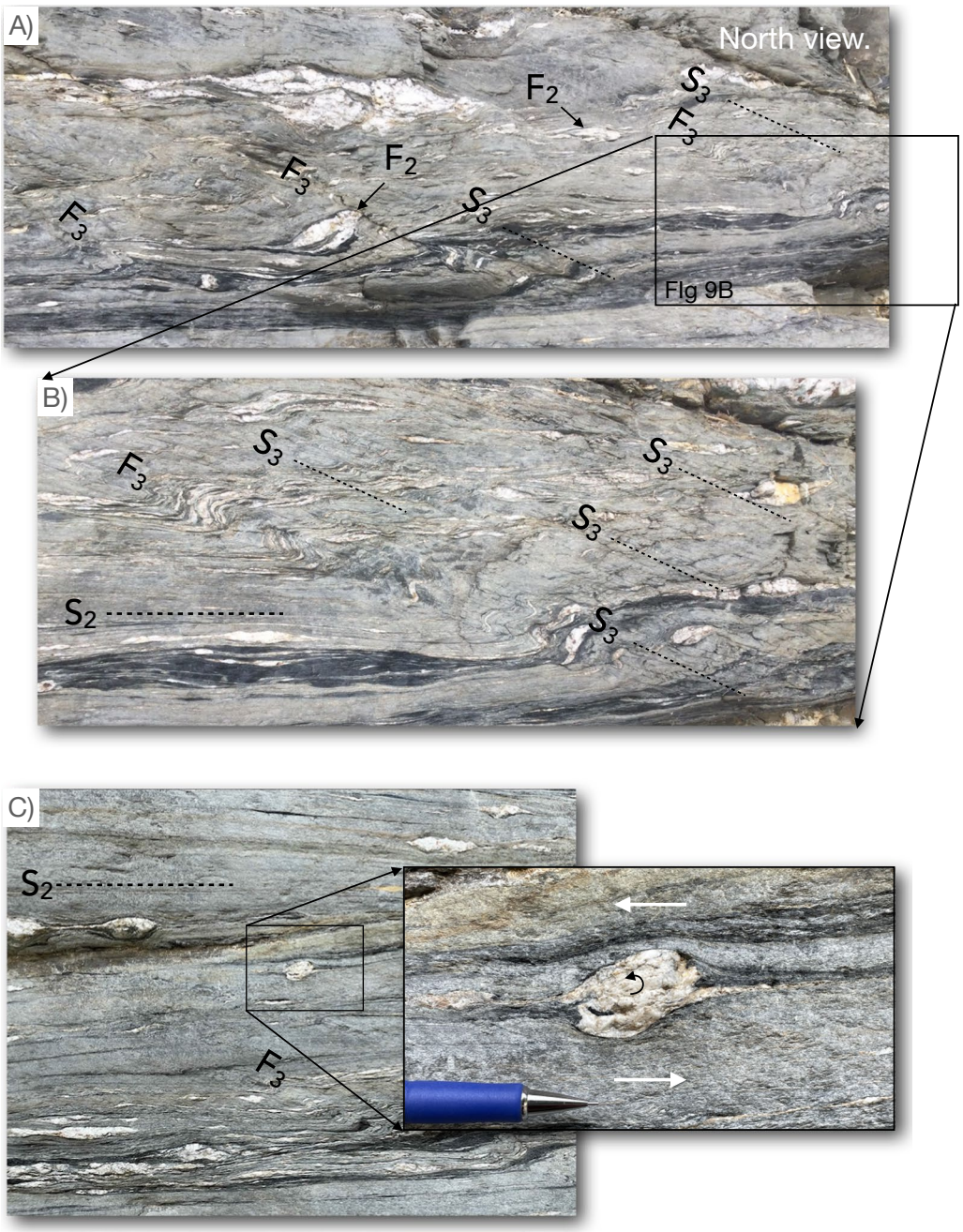

Fig. 9 Outcrop photographs of S–C phyllonite in the Yuli Belt along the north bank of the middle Chingsuei River (see Fig. 5 for location). Main foliation, S_2, dips gently north (Fig. 10A and is horizontal in the photographs. Isolated isoclinal fold hinges with one suggesting an S-shaped asymmetry (black arrows) indicate a pre-existing foliation. Elliptical quartz inclusion oblique to S_2 (**C**, inset) suggests a top-to-the-west sense of shear during S_2. D_3 fold axial surfaces, F_3, and crenulation cleavage, S_3, dip east (Fig. 10A). Scale, shear sense and view direction are the same in all photographs

wrinkled or folded by a moderately developed foliation that dips gently northeast (Figs. 10B, 12C). Along the western Chingsuei, strain fringes around euhedral pyrite crystals are parallel to a weak mineral lineation on the late foliation and appear related to the development of the late, low-dipping foliation (Fig. 12B). The fringes and mineral lineation record northeast stretching parallel to the extension direction inferred from the late quartz veins (Fig. 12C). Based on cross-cutting relations and observations along strike (i.e., Dalun River, discussed

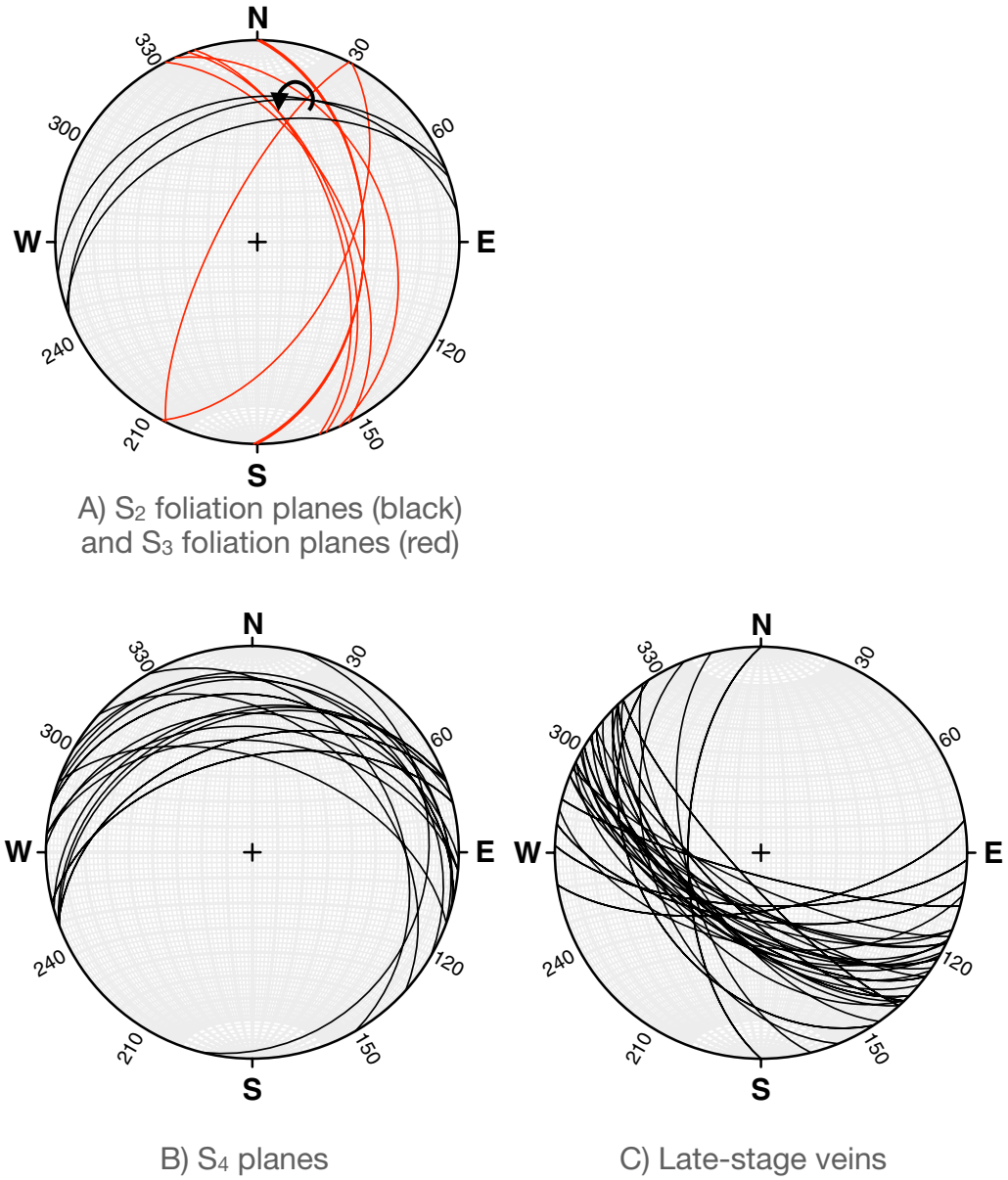

Fig. 10 Structural orientation data from the S–C phyllonites in the Yuli Belt along north bank of the middle Chingsuei River. **A** Orientation of S_2 and S_3. Late-stage foliation, S_4, and associated late-stage veins dip gently north and steeply southwest, respectively (**B** and **C**)

below), we interpret the late-stage veins and associated foliation to represent D_4.

5.4 Dalun and Xinwulu Rivers

The Dalun River hosts a series of meanders subparallel to the Shoufeng Fault (Stanley et al. 1981) and joins the Xinwulu River near the eastern end of the SXIH (Fig. 13A). In this area, the Tailuko comprises a marble-rich unit composed of various quartz and mica schists, chert, and discontinuous white and light gray marble layers. Outcrops along the Dalun and closest to the Xinwulu show a moderately west-dipping mylonitic foliation that Stanley et al. (1981) and Ho et al. (2022) labeled S_2, based on cross-cutting relations and regional patterns. Ho et al. (2022) also recognized a sub-horizontal stretching lineation and well-developed asymmetric folds and lenses of quartz and marble, consistent with left-lateral shearing. Our mapping along the Dalun River south of the junction with the Xinwulu shows S_2 having a moderate to steep northwest dip (Fig. 13B), consistent with Stanley et al. (1981) and Ho et al. (2022). We also mapped a moderately west-dipping foliation (Fig. 13B) that deforms S_2

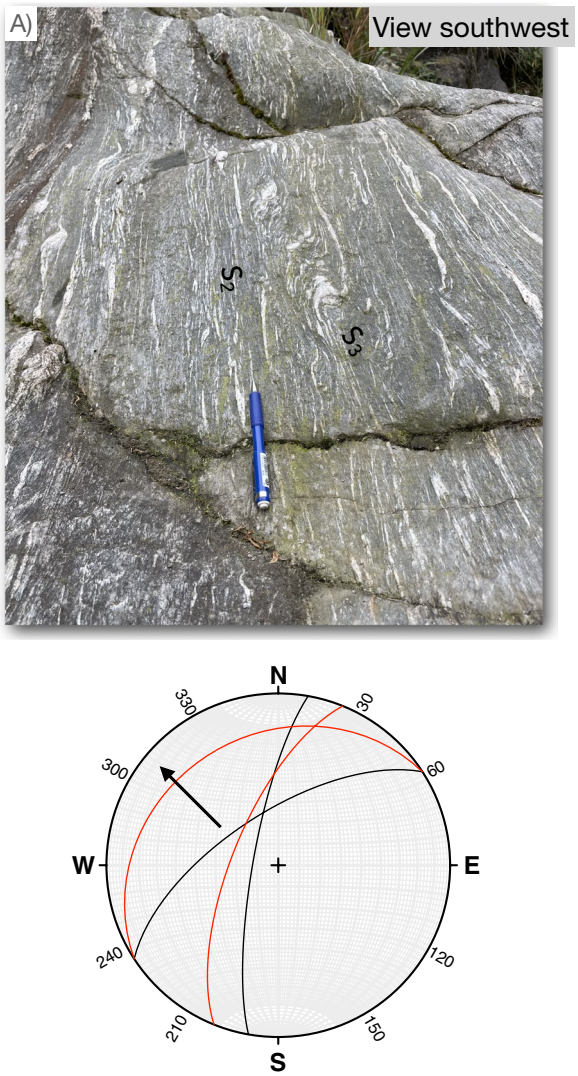

Fig. 11 Outcrop photograph and structural data of phyllonite in the Yuli Belt along south bank of the western Chingsuei River (see Fig. 5 for location). **A** Photograph of well-developed phyllonite, parallel to pencil and later shear zone interpreted to be S_3. View southwest. **B** Orientation data for S_2, and S_3, fabrics in A. Movement direction (black arrows) is inferred from asymmetric folds associated with S_3 and shows west-side down

and is axially planar to west-verging asymmetric folds of S_2 This foliation is equivalent to S_3 of Stanley et al. (1981) and may have been included as part of D_2 in Ho et al. (2022). The S_3-related folds typically have relatively gentle to open interlimb angles. However, in many cases, the interlimb angle decreases substantially as the amplitude of the fold increases, producing tight to isoclinal folds and suggesting progressive shear approximately parallel to S_3. Although these structures were not studied in detail, we interpret the asymmetric folds and progressive shear zones as D_3 "*P*" shears (Fossen 2010) related to the westward thrusting of the Yuli above the Tailuko rather than part of D_2.

Finally, exposures along the Dalun and Xinwulu Rivers also show a younger, gently dipping foliation (Fig. 13D) that appears to have formed contemporaneously with the development of late-stage quartz and calcite veins that dip steeply northeast (Fig. 13C). This late fabric appears undeformed by S_3 and we have labeled it S_4. However, this late fabric is significantly different from S_4, as defined by Stanley et al. (1981) and is more similar to Stanley's F_6 event, which includes a weak, gently dipping cleavage associated with late-stage veins that dip steeply northeast. This gently dipping late-stage foliation is also geometrically and temporally similar to S_3 recognized by Ho et al. (2022) and Ho and Lo (2015) in their studies of the Tailuko Belt, and S_3 recognized by Lin et al. (1984) in the Yuli Belt along the Chingsuei River. To reconcile these different interpretations and maintain consistency across units, we follow Stanley and use S_3 for low to moderately dipping foliation associated with west-verging asymmetric folds along the Dalun River and S_4 for the more gently dipping and younger foliation associated with late-stage steeply dipping veins. That is, we recognize S_3, as defined by Stanley et al. (1981), as a penetrative fabric that formed in association with west-directed thrusting of the Yuli Belt above the Tailuko Belt. We apply a similar interpretation to the asymmetric folds along the western Chingsuei (see above and Fig. 11A) near the map trace of the Shoufeng fault and suggest that similar interpretations may apply to other structures near the Shoufeng. However, some areas may also preserve a transition from dominantly strike-slip, D_2, to dominantly west-directed thrusting, D_3.

5.5 Hongye River

Exposures along the Hongye River are more limited, although one outcrop near an abandoned outwash control structure exposes the core of an overturned synform (Fig. 14) cut by a gently dipping foliation associated with steeply dipping late-stage quartz veins. The fold and associated minor folds trend northeast and displays an axial surface that dips moderately southeast (Fig. 14A, B), consistent with early formed folds in the Yuli Belt. The fold geometry suggests that its part of a northwest-verging asymmetric fold, again similar to other folds in the Yuli Belt.

The late-stage structures that cross-cut the outcrop-scale fold are interpreted to represent D_4 structures and include a penetrative foliation, S_4, lineation, L_4, and shear bands (Fig. 15). A suite of relatively late veins, generally perpendicular to stretching lineation on S_4, are also

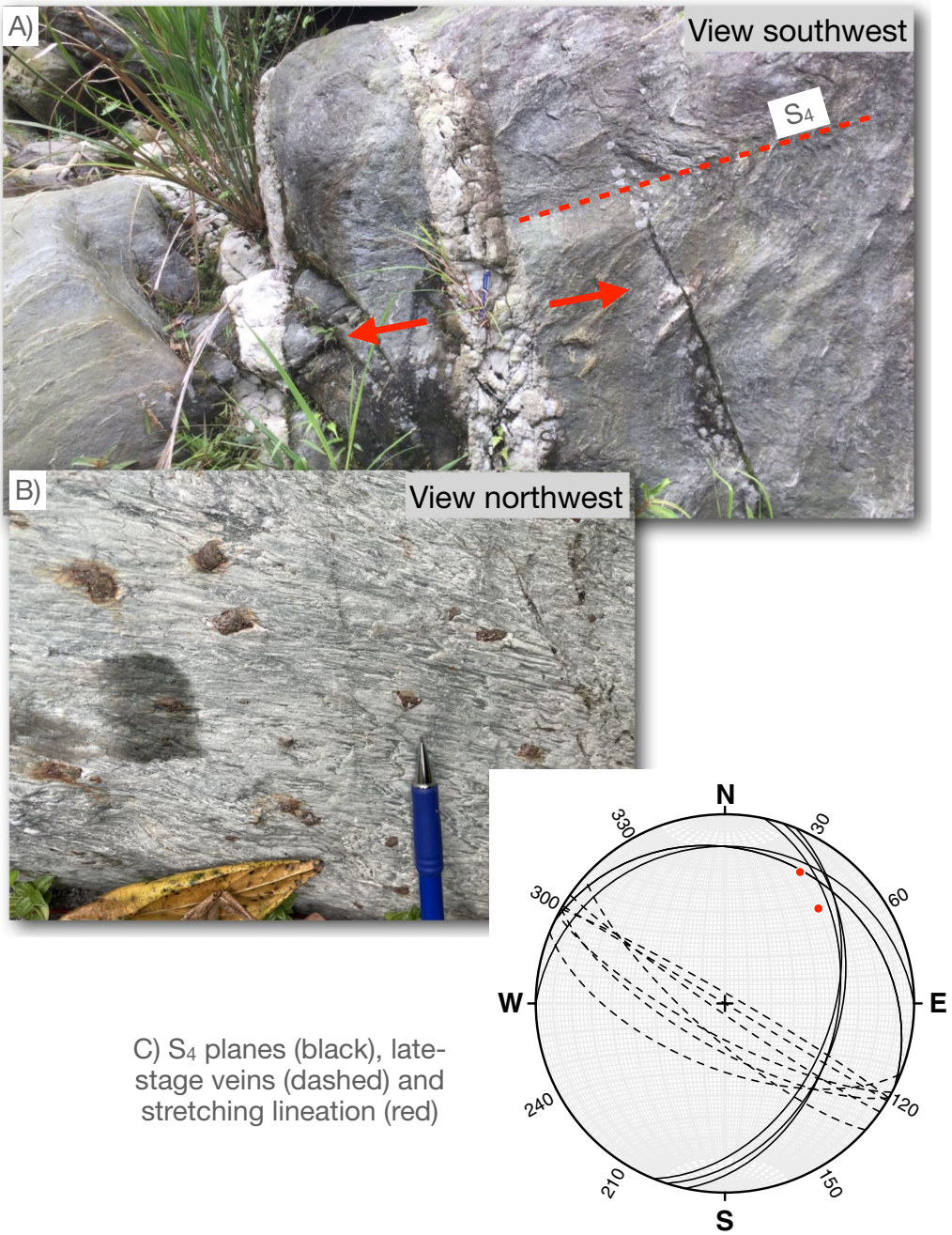

Fig. 12 Outcrop photographs and orientation data along the south bank of the western Chingsuei River (see Fig. 5 for location). **A** Two late-stage quartz veins and F_4 axial surface (red dashed line). **B** Quartz-mica schists with quartz-filled strain fringes around euhedral pyrite. **C** Orientation data for S_4 cleavage, L_4 stretching lineation, from the strain fringes, and late-stage veins

present (Fig. 15A, C). The geometry of S_4 and the shear bands suggest they represent either extensional shears or planes of penetrative shortening. The former would indicate a top-to-the-north sense of shear, whereas the latter would indicate the opposite sense of shear.

Thin-section observations in X–Z sections of S_4 provide additional information in resolving the kinematics. For example, albite porphyroblasts record an interior foliation observed by linear arrays of opaque minerals, including graphite (Fig. 16). The interior foliation is characterized by gentle to open folds, but the host

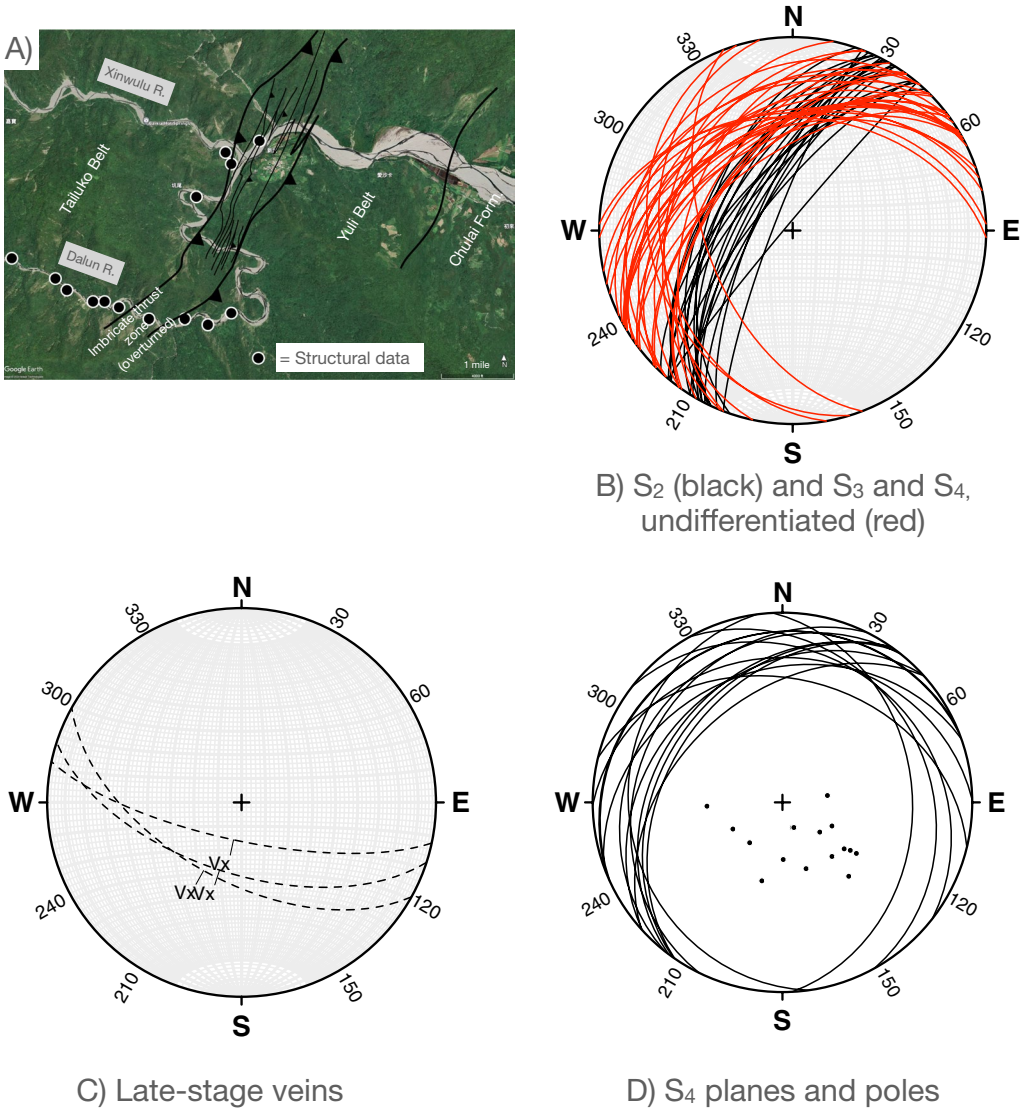

Fig. 13 Geology and structural orientation data around the Dalun and Xinwulu Rivers junction. **A** Google image and geologic map showing an imbricate thrust zone between the Tailuko and Yuli Belts (from Stanley et al. 1981) and data sites for this study. **B** Orientation data of S_2 (black great circles) and S_3 and S_4 undifferentiated (red great circles). Orientation data for late-stage veins (**C**) and S_4 (**D**)

albite grains display no sign of crystal plastic deformation. The trends of the interior and exterior foliations are also different by as much as 50° and indicate a top-to-the-southwest asymmetry. Strain shadows are infilled with chlorite, albite, and, less commonly, muscovite. Ilmenite porphyroblasts at a high angle to the foliation yield relatively large strain shadows, resulting in chlorite strain fringes with a low L:W ratio. Strings of fine-grained phyllosilicates in the fringes estimate the instantaneous stretching axis and indicate a top-to-the-southwest sense of shear. We therefore interpret the shear bands observed in the outcrop (Fig. 15A) as compressional structures (i.e., "S" surfaces) associated with top-to-the south-southwest shear (Fig. 15A, C).

5.6 Mugua River

Along the north bank of the Mugua River, in the northern exposures of the Yuli Belt (Fig. 1), a stretched pebble conglomerate provides additional insights into S_3 and S_4 (Fig. 17). The outcrop exposes a meter-thick shale-matrix conglomerate interlayered with sandstone, phyllite, and greenschist, preserving at least in part a stratigraphic succession. The units, however, are intensely deformed, and the pebbles, composed primarily of chert, appear flattened and highly elongated. The long axes of the pebbles parallel lithologic layering, the dominant foliation in the area, and plunge gently northwest (Fig. 17B). The shapes of the deformed clasts measured on oriented slabs yield similar values for Y/Z and X/Y, suggesting plane strain.

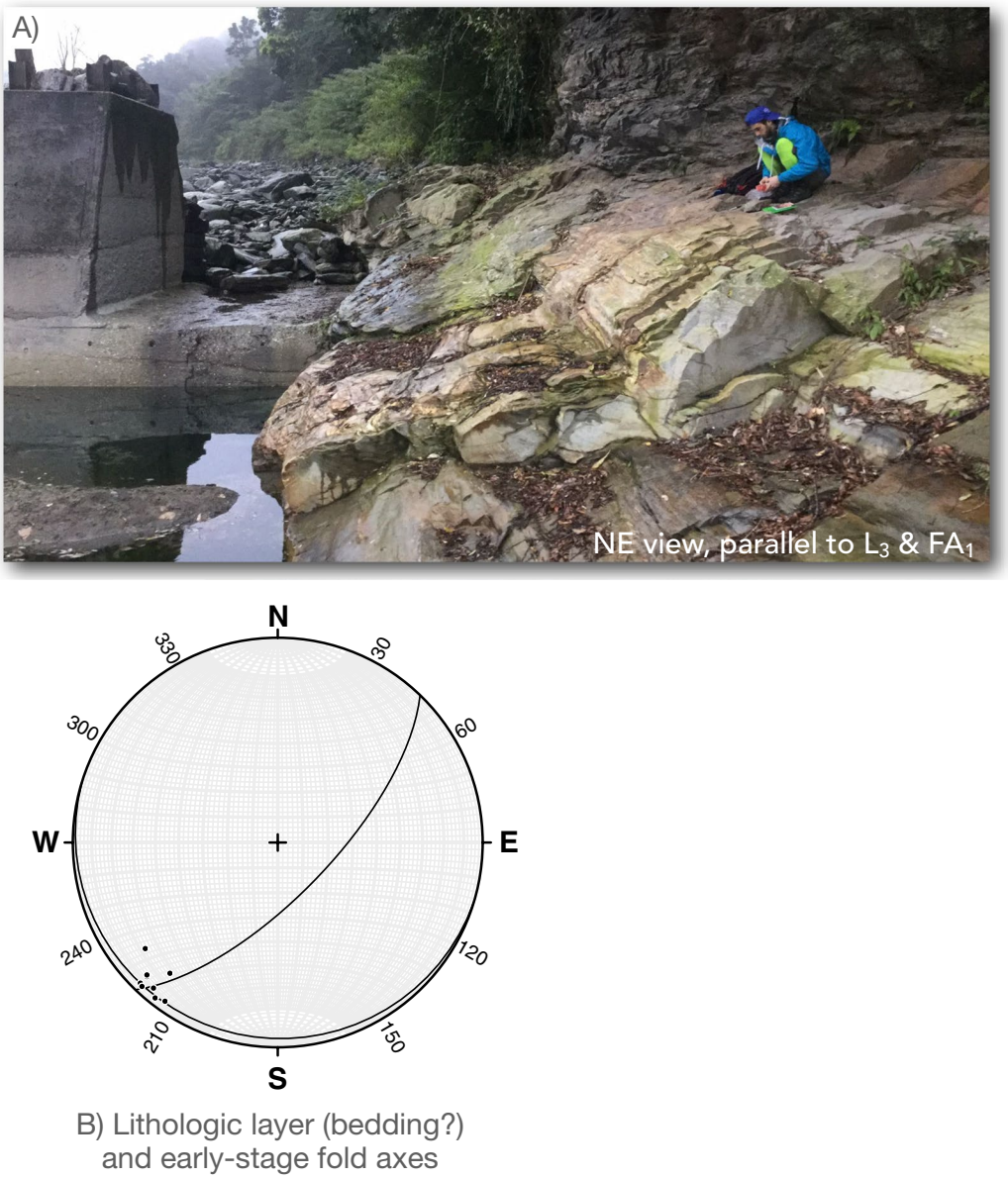

Fig. 14 Photograph and structural data of an outcrop-scale synform in the Yuli Belt along the Hongye River. **A** Synform fold axis trends northeast parallel to the change in slope where the person is sitting and axial surface dips moderately southeast (right). **B** Orientation of lithologic layering (bedding?) (black great circles) and fold axes of smaller folds associated with the synform

The primary foliation dips gently north and is locally cross-cut by a crenulation cleavage that dips gently northeast (Fig. 18). The intersection lineation also plunges gently northeast, approximately perpendicular to the long axis of the pebbles. The two foliations and the stretching direction provided by the elongated pebbles suggest an S–C relation. At this point, however, we have not confirmed whether the crenulation cleavage is "S," which indicates top-to-the-northwest, or C' an extensional crenulation cleavage, which would indicate top-to-the-southeast.

We also recognized a low-dipping foliation interpreted to be S_4, and a suite of late-stage veins (Fig. 19A, B) that appear unaffected by the S–C foliations. The veins are generally orthogonal to the low-dipping foliation, and to a weak mineral lineation on S_4, suggesting they are part of the late-stage structures recognized throughout the eastern Backbone Range.

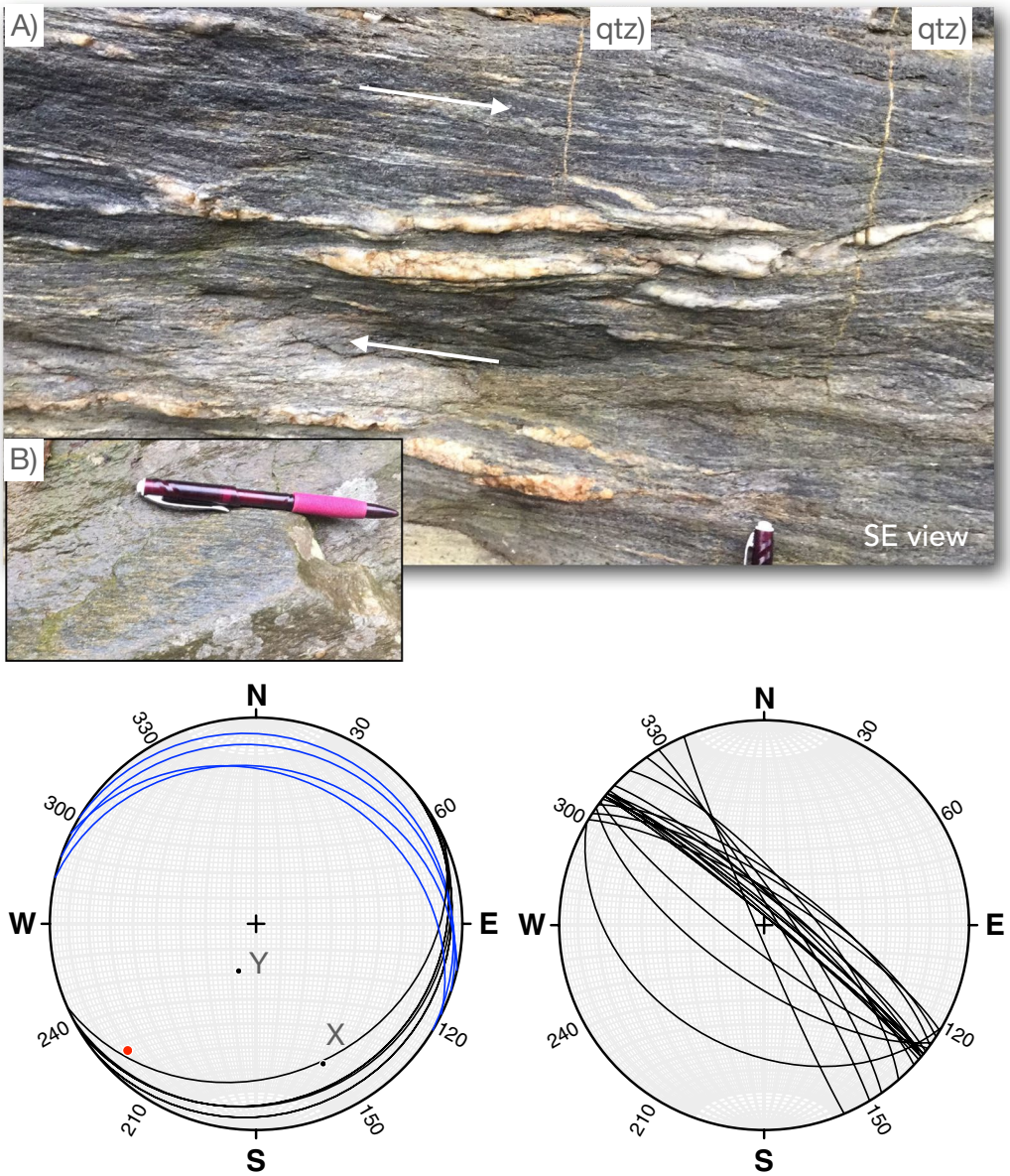

Fig. 15 Photograph of outcrops and orientation data associated with phyllonite along the gently dipping limb of the synform in Fig. 14. **A** Outcrop photograph of rock face approximately parallel to the *XZ* plane of youngest foliation, S_4. Inset **B** shows stretching lineation on the youngest foliation. Lineation trends southwest (**C**), approximately perpendicular to late-stage extensional veins in A and plotted in **D**. S–C fabrics, blue and black great circles in **C**, respectively, and rotated porphyroblasts (Fig. 16e, f) indicate a top-to-the south-southwest sense of shear. Based on correlations with fabrics observed in the western Chingsuei River the late fabrics are interpreted to be D_4 structures

5.7 Heping and Kukutsu areas

We completed reconnaissance fieldwork in the areas of the Heping River and Kukutsu Cliffs (Fig. 1) to confirm structural patterns identified by previous workers and collect additional structural data and samples for $^{40}Ar/^{39}Ar$ dating. The Heping River area exposes outcrops of the Tachoshui gneiss whereas the Kukutsu Cliffs exposed the Kanagan gneiss (Lin and Chen 2016). Both suites of rocks are interpreted to Cretaceous intrusions and display a well-developed north-northwest dipping

mylonitic foliation with an associated mineral stretching lineation that plunges gently west (Ho et al. 2022; Korren et al. 2017; Chen et al. 2022; Jiao 1991). Ho et al. (2022) consider the mylonite to be the second foliation, S_2, in the Tailuko Belt, and we follow their terminology here. Wang et al. (1998) obtained ages ranging from 4.1 to 3.0 Ma for the mylonite based on $^{40}Ar/^{39}Ar$ crystallization ages of biotite. The mylonite is cross-cut by pseudotachylite-lined normal faults (Korren et al. 2017) that yield 1.5 Ma ages using $^{40}Ar/^{39}Ar$ (Chen et al. 2017a), consistent with the older ages from the mylonite, which it cross-cuts.

The mylonites are also cut by north-striking, vertical veins and a penetrative but sparsely developed foliation that dips gently southwest (Figs. 20). The late-stage veins display a variety of thicknesses and contain quartz, calcite, chlorite, and, less commonly, adularia or sanidine, epidote, and phengite (Fig. 20A). A weak mineral stretching lineation, L_3, associated with the low-dipping foliation plunges moderately east-northeast, parallel to the extension direction inferred from the late veins (Fig. 20B, C). A late-stage extension shear zone less than a centimeter in thickness and associated with the late-stage foliation also yielded an east-side down sense of shear (Fig. 20D). These stretching lineations are also subparallel to striations associated with the formation of the pseudotachylite (Fig. 2, site B) (Korren et al. 2017). We interpret these late-stage lineations to be D_4 structures. Chen et al. (2022); (see also Wang 1998) obtained 1.1 and 1.5 Ma ages for two samples of adularia from the veins in this area based on $^{40}Ar/^{39}Ar$, and additional isotopic ages of adularia from these outcrops are discussed below. Following Chen et al. (2022), we infer that the extensional veins and pseudotachylite formed contemporaneously and propose that D_4 also formed at this time.

Finally, the Heping and Kukutsu areas are in the northern limb of the Backbone Range orocline, and late-stage structures appear to have rotated ~48° CW viewed down about a vertical axis relative to similar structures south of the orocline (Fig. 1). This rotation is consistent with GPS data from the RYUK block, which shows the northern limb of the orocline rotating at ~47°/Myr, suggesting that the orocline was initiated ~1 Ma. In our compilation of late-stage structures (Fig. 21), we show the observed orientation of the structures from Heping and Kukutsu and the orientation of the structures after 48° of rotation.

5.8 General characteristics of the late-stage foliation, S_4

On the regional scale, the youngest penetrative foliation in the eastern Backbone Range dips shallowly to moderately northwest or southeast, and a compilation of data collected along the eastern Backbone Range (Fig. 21) suggests a gently northeast plunging antiform. These results are consistent with mapping in the central part of the Yuli Belt that shows a broad, elongated antiform centered on the Yuli Belt (Gungfu area Yi et al. 2012) (Fig. 2) and with a limited number of more detailed studies in the Tailuko, Yuli and Slate Belts (Fig. 2) (Ho and Lo 2015; Lee 1995; Clark et al. 1992; Stanley et al. 1981) that suggest the youngest foliation forms one or more gently northeast plunging antiforms. The youngest foliation is also associated with a suite of late-stage extensional veins that consistently record northeast extension (Fig. 21). Northeast extension during the development of the youngest foliation is also consistent with limited observations of the finite strain. A geometrically and kinematically similar fabric also occurs in the lower-grade rocks that crop out south and east of the Yuli Belt and may represent shallow structural levels of a Late Miocene accretionary prism associated with the Yuli Belt (Chen et al. 2019). Finally, a systematic study of the kinematics associated with the youngest foliation suggests a slight bias toward a top-to-the-southwest sense of shear.

At an outcrop scale, the late-stage foliation ranges from a low-angle penetrative pressure solution cleavage in lower-grade units to a low-angle crenulation cleavage often parallel to axial surfaces of open-to-isoclinal folds.

(See figure on next page.)

Fig. 16 Photomicrographs of structures produced by D_4 deformation in the Yuli Belt along the Hongye River. Schematic in bottom left of each photograph illustrates the interaction of S_4 (red) with previous foliations or other structures. White arrow shows the coordinate direction, and plunge and trend indicate the view direction and pole to the plane of the thin section. See Fig. 15C for orientation data. **a**, **b** (XPL) show albite-rich (top) and albite-poor (bottom) domains defining the cleavage. **c** Quartz grains within microlithons that show grain shape preferred orientation, slight undulose extinction, and grain boundaries indicative of sub-grain rotation and grain boundary migration recrystallization. **d** Relationship between a relatively early formed lineation, defined by an aggregate shape preferred orientation (labeled L3-1, ASPO and a later lineation defined by a grain shape preferred orientation (labeled "L3, GSPO"). The early formed lineation is interpreted to represent D_2, whereas the later lineation is interpreted as L_4. Photograph is parallel to XY plane of S_4. **e** Albite porphyroblasts within a cleavage domain depicting an interior foliation and over-growth zoning. Acicular rutile with ilmenite coatings, tourmaline, and apatite inclusions are common, especially in grains with a deformed interior foliation. Locally, one coated ilmenite grain is isoclinally folded, while another depicts extension. **f** SEM-BSE image of image in **e**, depicting the variation in composition. Albite porphyroblasts contain ilmenite inclusions and are surrounded by chlorite and muscovite strain fringes. Different orientations of internal and external foliations indicate a top-to-the-right sense of shear, which in geographic coordinates is top-to-the-southwest. Orientation data are shown in Fig. 15

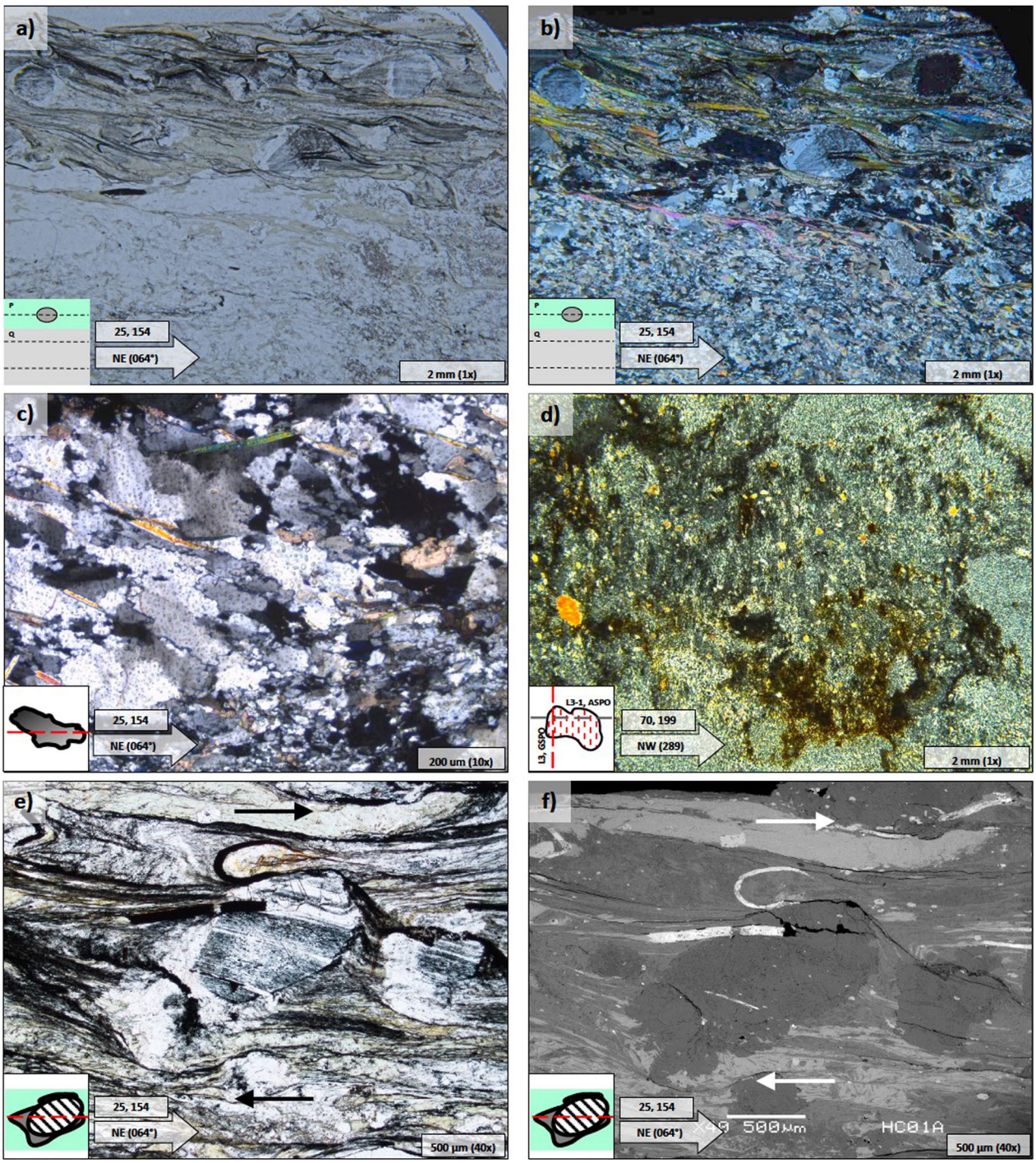

Fig. 16 (See legend on previous page.)

The folds can be inclined or recumbent depending on the initial orientation of the folded foliation (Fig. 22B). For example, in the Tailuko Belt, where the older foliations typically dip steeply to moderately west, D_4 folds are relatively common and are generally asymmetric with short limbs that appear to have rotated counterclockwise (when viewed to the north). Fold axes also plunge shallowly to the northwest (Ho et al. 2022), consistent with superposition of the low-dipping S_4 on steeply to moderately dipping layering. Folds are less common in the Yuli Belt, where the older foliations have more variable dips. The common occurrence of quartz- or mica-rich schists

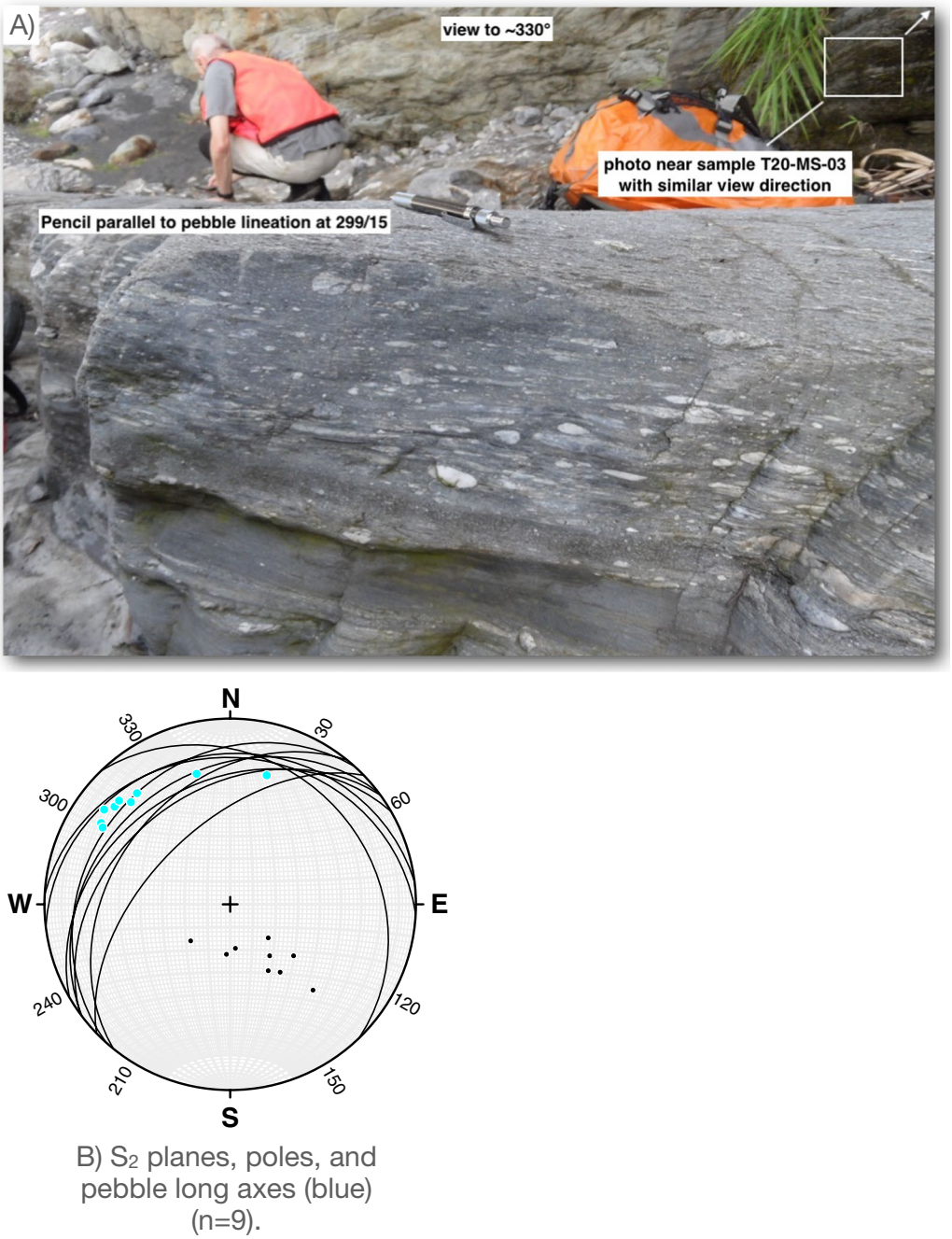

Fig. 17 Outcrop photograph (**A**) and orientation data (**B**) of a matrix-supported pebble conglomerate in the Yuli Belt along the north bank of the Mugua River

also results in a rough to dispersed cleavage rather than a planar pressure solution cleavage, making identifying S_4 more challenging.

In thin section, S_4 is defined by late-stage, ductile deformation, including continuous foliations, S–C foliations, extensional crenulation cleavages, and strain fringes around relatively rigid inclusions, including albite, pyrite, and ilmenite porphyroblasts (Fig. 16). S_4 is observable by ductile/brittle deformation and a retrograde mineral assemblage, including quartz + albite + muscovite + chlorite + others that often fill S_4-related strain fringes. Cleavage domains and high-strain zones

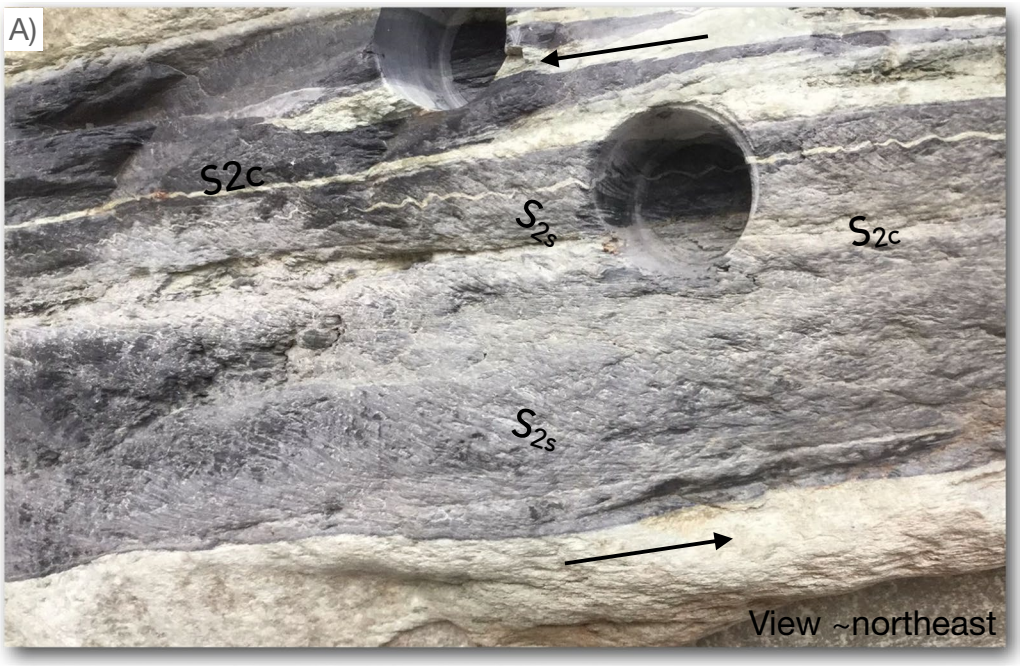

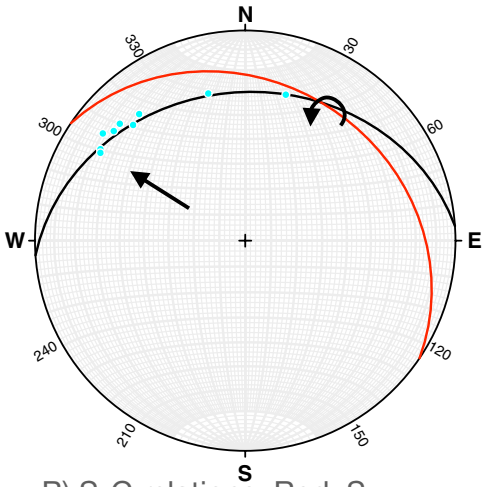

B) S-C relations: Red: S_{2s}, black: S_{2c} and pebble long axes, blue

Fig. 18 Outcrop photograph and orientation data of intercalated mudstone and greenschist capped by greenstone and interlayered with the pebble mudstone shown in Fig. 17. **A** Photograph of rock surface approximately parallel to *XZ* plane of S_2 strain ellipsoid. Interpreted S and C surfaces associated with S_2 are labeled. 1-inch drill hole for scale. **B** S–C relations for individual outcrop. Curved arrow: rotation axis interpreted from S–C intersection; black arrow: movement direction inferred to be perpendicular to S–C intersections and shows top-to-the-northwest. Blue dots show trend and plunge of pebble long axes (from Fig. 17)

contain muscovite, chlorite, albite, and graphite. Syn-S_4, mineral-filled, mode-I fractures are also common where S_3 is developed.

5.9 General characteristics of the late-stage veins

The late-stage, mineral-filled, mode-I fractures, or veins, track the distribution of the youngest penetrative

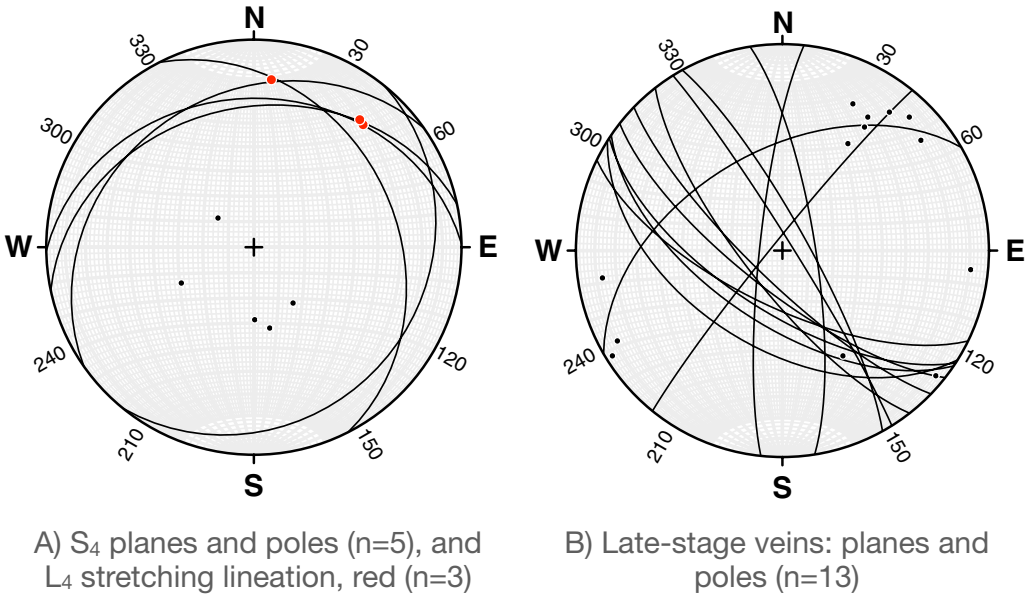

Fig. 19 Orientation data from the Yuli Belt along the north bank of the Mugua River (Fig. 18): **A** Late-stage foliation and associated stretching lineation and **B** quartz veins. Based on correlations with fabrics observed in the western Chingsuei River, the late fabrics are interpreted to be D_4 structures

foliation through the core and cover rocks. The veins consistently dip moderately to steeply southwest (Fig. 21), except in the northernmost sites where the Backbone Range has been rotated clockwise (Fig. 1). The veins generally range in thickness from 0.25 to 20 mm but can be up to 10–15 cm and are often filled or partially filled with quartz + albite + calcite +/− adularia. Rare mineral inclusions of muscovite and ilmenite were observed. In outcrop, the veins appear generally undeformed and cross-cut the major fabrics. However, closer inspection (e.g., hand lens and petrographic observations) reveals that they show slight ductile deformation and are locally offset by the penetrative foliation (Figs. 22, 23E, F).

In thin sections, the veins show evidence of brittle/ductile strain. The center of the fracture-fill displays euhedral to subhedral, equigranular arrays of quartz, albite, and adularia that show uncommon undulose extinction and grain boundaries indicative of bulging recrystallization and less common sub-grain rotation recrystallization. These grains also display elongate-blocky to fibrous vein mineral morphologies (Fig. 23A–D); (see, e.g., Bons 2000). Elongate grain morphologies perpendicular to the edge of the vein formed by the crack-seal mechanism (Ramsay 1980) and indicate the veins formed as repeated mode-I fractures as fluid pressure exceeded the tensile strength within the rocks (Secor 1965). The elongate crystals are generally quartz and albite, 50–200 μm in length, and optically continuous to each other. They show little to no undulose extinction, and inclusion trails parallel to the vein edge are common. The mode-I fractures most commonly display syntaxial growth morphologies, indicating the most recent growth was within the center of the vein.

5.10 Fluid inclusion analysis of late-stage vein materials

Fluid inclusion microthermometry on quartz and adularia crystals from the veins was also utilized to provide constraints on the pressure and temperature conditions, and estimates of the metamorphic fluid compositions during vein formation across the metamorphic core. Previous fluid inclusion microthermometry studies in the core are uncommon. On the westernmost edge of the Slate Belt, along the Lishan fault, amorphous quartz veins with two-phase fluid inclusions record homogenization temperatures between 208 and 225 °C and salinities of 4.9% NaCl (Chan et al. 2005). The continued mineralization of the quartz, as well as deeply sourced albite (sodium), potassium feldspar, and rare earth elements at cooler, epithermal conditions, was attributed to a steep fluid overpressure gradient maintained by the overlying slate cap-rock. On the eastern edge of the Slate Belt, near the contact with the Tailuko Belt and the CXIH, Craw et al. (2009) used fluid inclusion microthermometry on silicic, ankeritic, and chloritic veins from the Pingfengshang gold mine. Entrapment temperatures ranged from 240 to 350 °C at inferred depths ranging from < 1 km to 10 km. The workers combined temperature data with thermochronological data from Beyssac et al. (2007) to

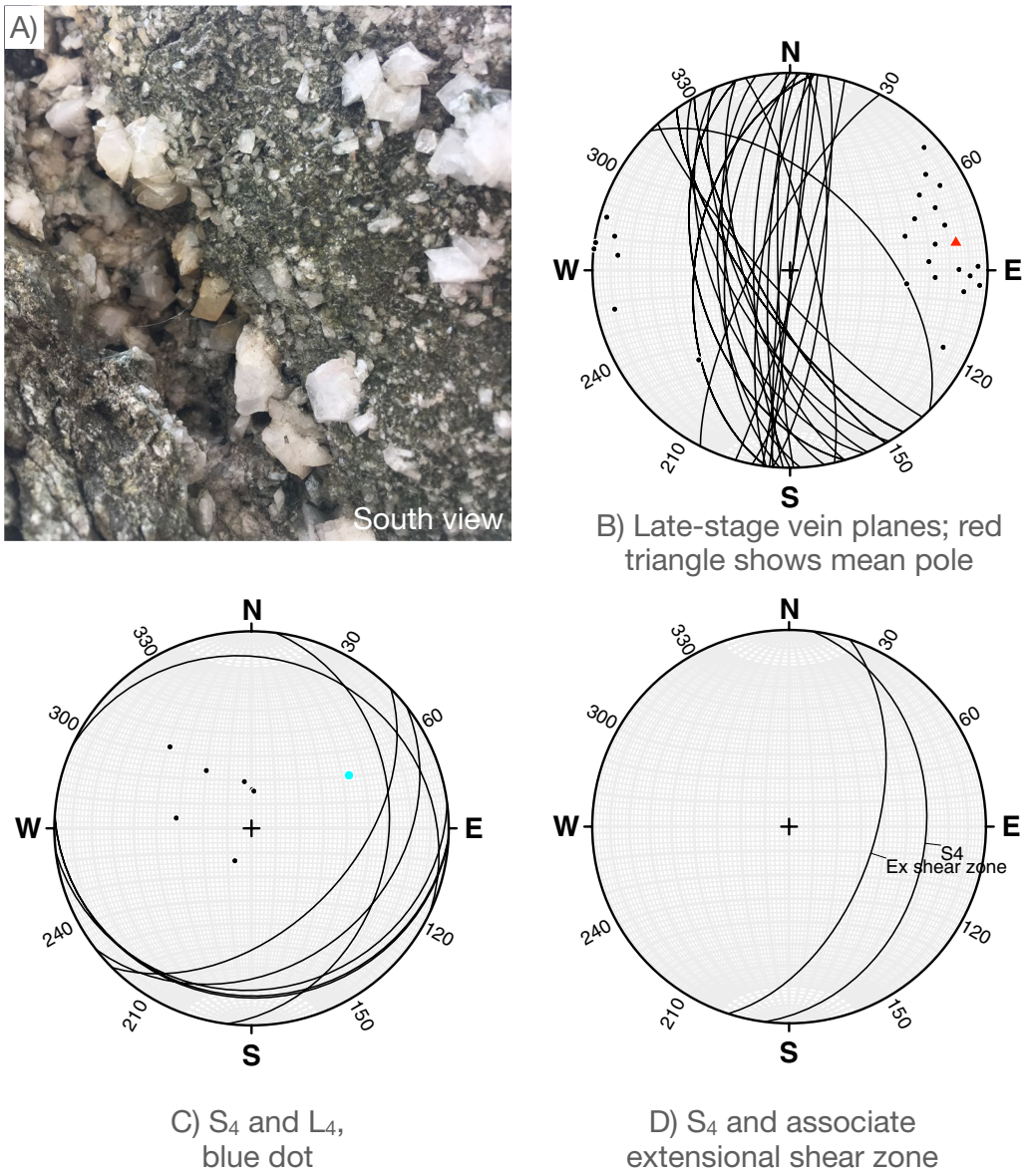

Fig. 20 Outcrop photograph and structural orientation data from Kukutsu Cliffs (Fig. 1 for location). **A** Photograph showing euhedral adularia crystals approximately 0.5 cm in width growing along the wall of a late-stage extensional vein. **B** and **C** show orientation data for late-stage veins and youngest penetrative foliation, respectively. **D** Orientation data for S4 and an associated extensional shear zone that indicate a top-to-the-east-southeast sense of shear. Based on correlations with fabrics observed in the western Chingsuei River, the late fabrics are interpreted to be D_4 structures. The Kukutsu Cliffs outcrops are located on the RYUK block (Fig. 1), which is rotating clockwise with respect to the central Backbone Range (Rau et al. 2008). See text for discussion

generate P–T–t paths and determine exhumation rates of 2 mm/yr for the rocks in the western slate belt. The orientation of late veins associated with conjugate kink bands at Pingfengshang are consistent with the orientation of the late-stage veins discussed here.

Our fluid inclusion microthermometry data (see also tables and fluid inclusion maps in Additional files 3, 4, 5, 6, 7, 8, 9, 10, 11, 12, 13, 14) indicate maximum temperatures during vein precipitation of between 200 and 450 °C. These temperatures are consistent with deformation textures of contain quartz and feldspar grains in cleavage microlithons that display undulose extinction and evidence of sub-grain rotation, bulging, and grain boundary migration recrystallization. These grain boundaries are consistent with deformation from approximately 350–500 °C (Fossen and Cavalcante 2017;

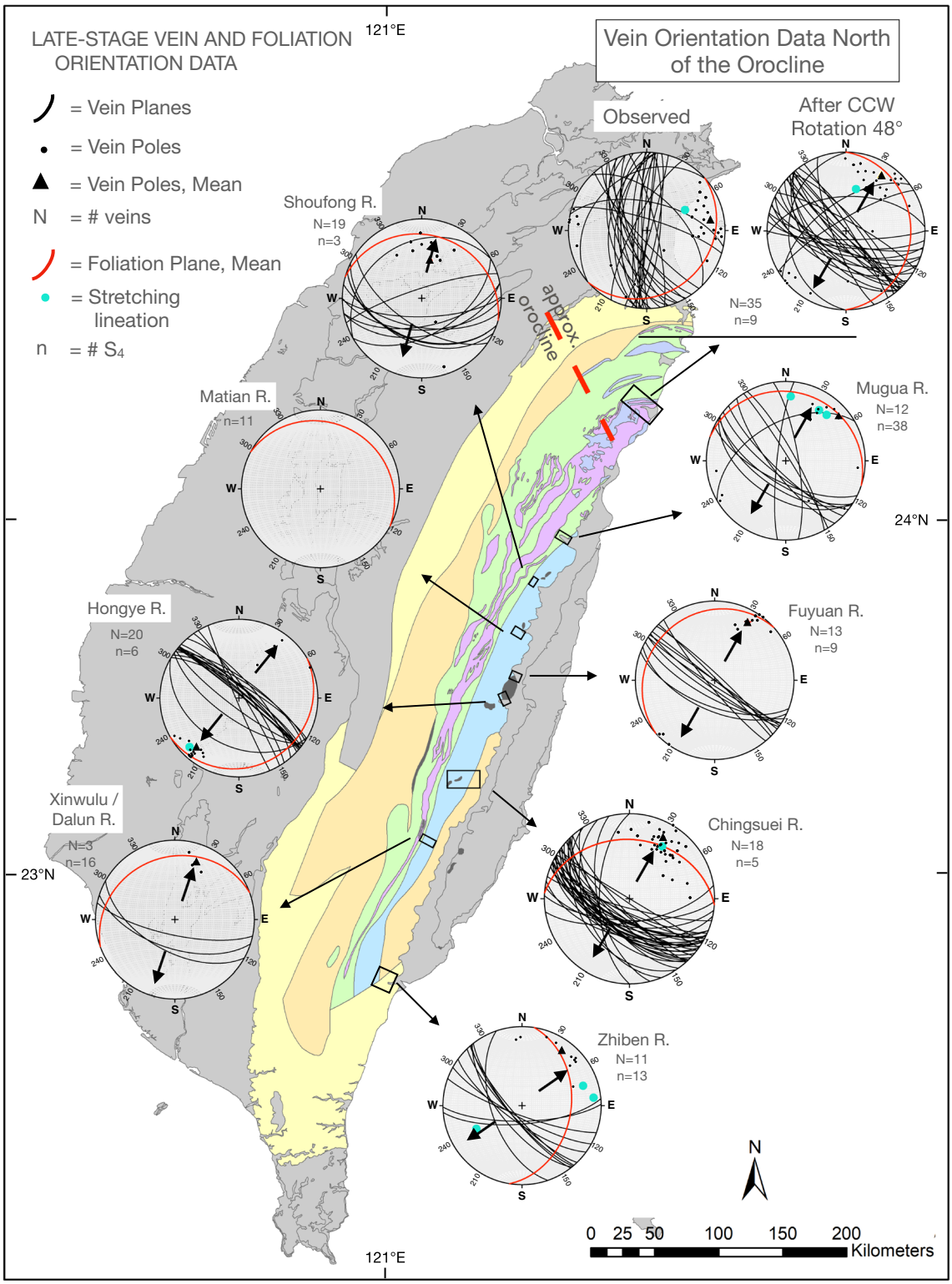

Fig. 21 Synthesis of new late-stage structural data from nine sites along the eastern Backbone Range. Data includes late-stage veins (planes, poles and mean poles), foliations and stretching lineations; not all sites have all types of data. Chingsuei River site is compilation of data along middle and western reaches. Northern most site shows orientation data for Kukutsu Cliffs and Heping River before and after rotation associated with the Backbone Range orocline. Arrows show extension direction inferred from vein orientations, stretching lineations and strain fringes

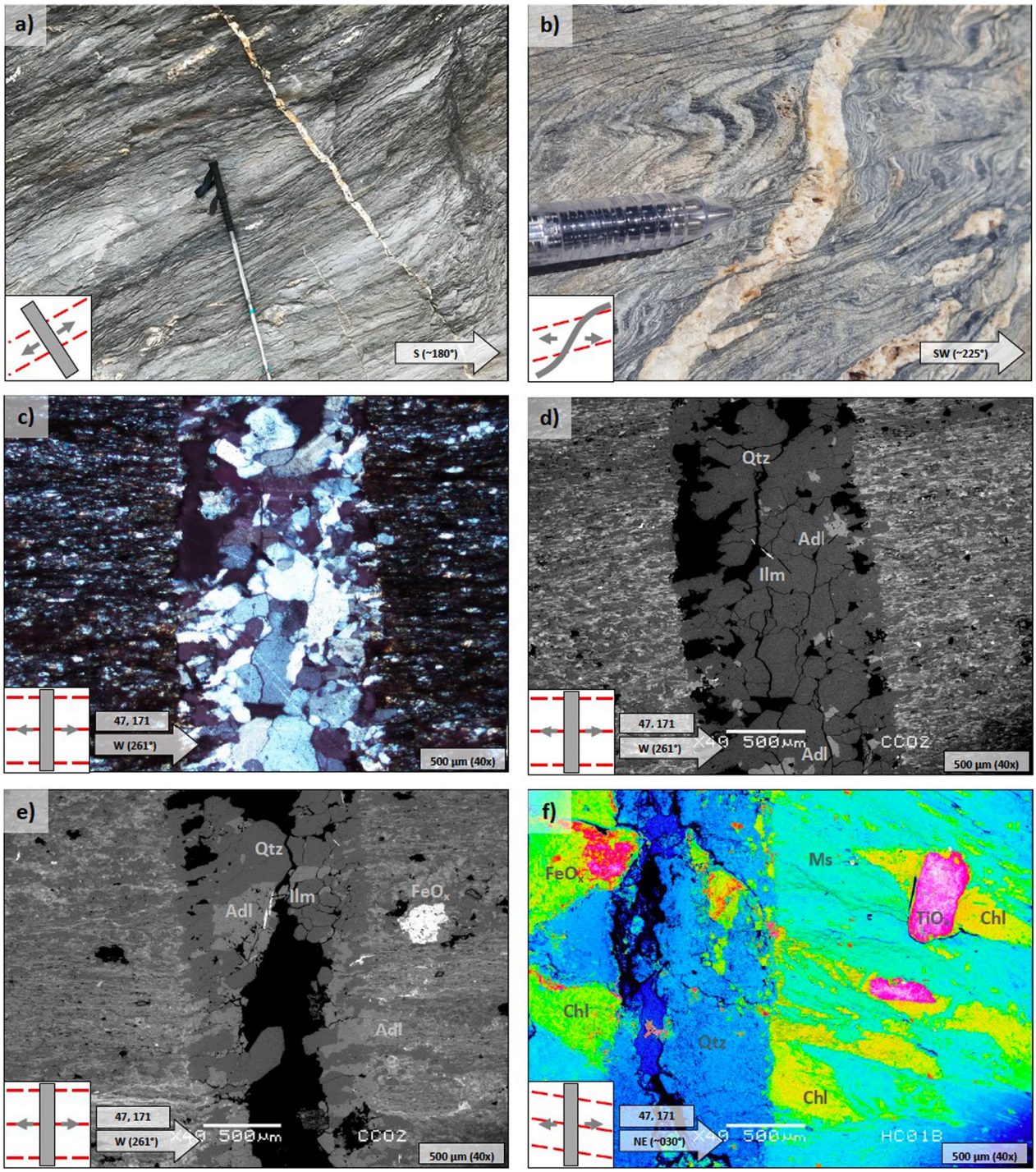

Fig. 22 Outcrop photographs and photomicrographs of veins from the Yuli Belt. White arrow shows the coordinate direction for photomicrographs; plunge and trend indicate the view direction and pole to the plane of the thin-section photomicrographs. Schematic in bottom left of each photograph illustrates the interaction of S_4 (red) with previous foliations or other structures. **a** Late-stage veins dipping south and cross-cutting S_4. **b** Late-stage vein cross-cutting S_2 and S_4 characterized by slight ductile deformation along S_4 planes. **c** XPL image of a late-stage vein at a high angle to S_4, featuring elongate, optically continuous albite grains. **d** SEM-BSE image of the late-stage vein in **c**. The vein contains quartz, adularia, and ilmenite. **e** SEM-BSE image of a late-stage vein containing quartz, adularia, and ilmenite featuring elongate to blocky grain morphologies. **f** SEM-BSE false color image of D_2/D_4 fabric, D_4 microstructures defined by the retrograde paragenesis in Ti-oxide strain shadows and of a late-stage vein at a high angle to the fabric. The vein contains quartz and chlorite

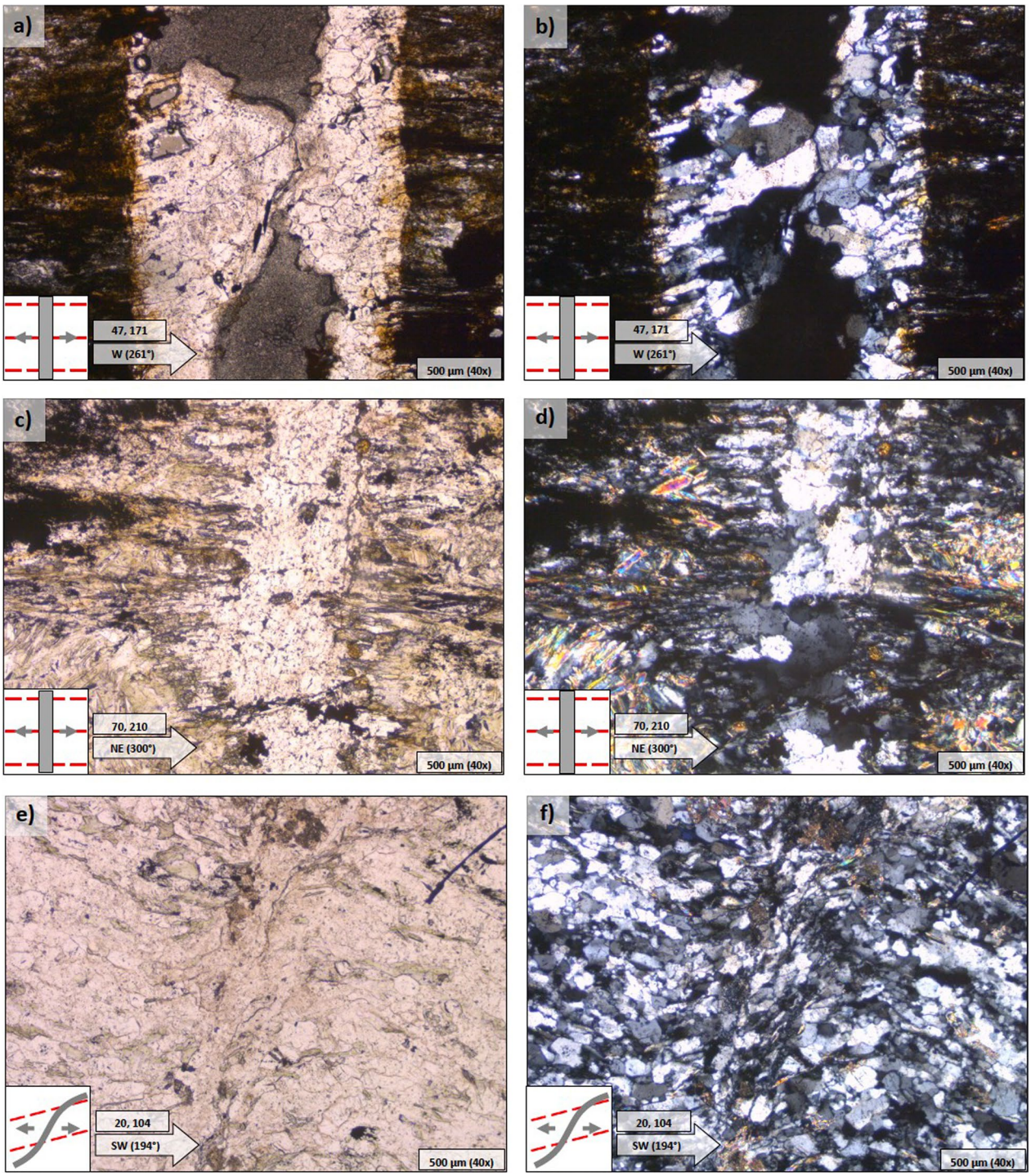

Fig. 23 Photomicrographs of veins from the Yuli Belt. White arrow shows the coordinate direction, and plunge and trend indicate the view direction and pole to the plane of the thin section. **a**, **b** (XPL)) Late-stage vein cross-cutting the S_4 fabric at a high angle. The vein features quartz, adularia, and ilmenite. Elongate grain morphologies are observable along the vein/wall rock contact, and blocky grains with slight undulose extinction are dominate in the center of the vein. **c**, **d** (XPL) Late-stage vein composed of quartz, albite, and uncommon chlorite cross-cutting S_4 characterized by ductile deformation along an S_4 cleavage domain. Elongate grain morphologies are observable along the vein/wall rock contact, and blocky grains with slight undulose extinction are dominant in the center of the vein. **e**, **f** (XPL) Thin vein with adjacent grains showing a grain preferred orientation indicating northeast-side-down normal offset

Passchier and Trouw 2005). Within the late-stage veins, evidence of grain boundary migration recrystallization is less common and may suggest slightly cooler temperatures during strain accumulation from the S_4 fabric (~< 400 °C).

The regional fluid system is composed of H_2O–CO_2–NaCl. High XCO_2, low XCO_2, and aqueous inclusions commonly occur in similar fluid inclusion assemblages or at least within the same sample chip. Homogenization temperatures range from 199 to 350 °C, and salinities range from 0.4 to 9.4 mass% NaCl. The variations in homogenization temperatures and salinities outlined below are attributed to the lithology or relative structural position of the country rock at each of the three sites.

Euhedral quartz and adularia crystals from the Kukutsu Cliffs, the northern site, preserve two-phase (LV, liquid and vapor), H_2O–NaCl inclusions ranging from < 5 to 50 μm in size, with an average of ~10 μm (Fig. 24a, b). Shapes were amorphous or negative crystal-polygonal in some adularia inclusions (Fig. 24A, B). Microthermometry was performed on twenty-eight fluid inclusions between two samples. Homogenization temperatures range from 199 to 229 °C +/− 5 °C with an average of 214 °C +/− 5 °C. Ice melting temperatures range from − 2 to − 0.2 °C +/− 3 °C with an average of − 0.87 °C +/− 3 °C. These melting temperatures correspond to salinities ranging from 0.4 to 3.4% mass NaCl (Fig. 25). The quartz and adularia samples from the northern site depict no compositional heterogeneity in SEM-CL. This suggests that all observed fluid inclusions are likely primary or pseudosecondary.

Quartz crystals from the central site along the Shoufeng River host primary and secondary, three-phase ($L_{aq}L_{CO2}$V) inclusions ranging from < 5 to 120 μm in size, with an average of ~40 μm; shapes are generally amorphous (Fig. 24c, d). Microthermometry was performed on eighty-eight fluid inclusions between two samples. Homogenization temperatures range from 240 to 350 °C +/− 5 °C with an average of 310 °C +/− 5 °C. The average CO_2 homogenization temperature was 30.1 °C +/− 5 °C. The melting temperature for the solid CO_2 phase was ~− 57.5 °C +/− 3 °C. Clathrate melting temperatures range from 4.7 to 9.4 °C +/− 3 °C with an average of 8.7 °C +/− 3 °C. Calculated salinities range from 0.4 to 9.4%mass NaCl (Fig. 25). The central samples depict rare growth zoning and common, post-formational, structural, and chemical heterogeneities observed as linear arrays of lower intensities in the CL image. Large, isolated inclusions and inclusions associated with growth zoning or no post-formational heterogeneities were interpreted as primary or pseudosecondary if along a compositionally homogeneous microcrack. Fluid inclusions associated with an assemblage parallel to linear heterogeneities in cathodoluminescence images were classified as secondary.

One quartz crystal from the southern site along the Xinwulu River hosts primary and secondary, two-phase (LV) inclusions ranging from < 5 to 75 μm in size, with an average of ~40 μm; shapes are generally amorphous (Fig. 24e, f). Microthermometry was performed on sixty fluid inclusions. Homogenization temperatures range from 282 to 340 °C +/− 5 °C with an average of 305 °C +/− 5 °C. Ice melting temperatures ranged from − 5.4 to − 1.5 °C +/− 3 °C. Calculated salinities range from 2.6 to 8.5%mass NaCl (Fig. 25). Distinct from the northern and central samples, the southern samples displayed conspicuous growth zoning parallel to crystal boundaries. A linear array of compositional heterogeneity was observed by cathodoluminescence in regions where growth zoning was less prevalent. The fracture-like arrays are < 500 μm in width and cross-cut growth zoning. Fluid inclusions in assemblages parallel to crystal boundaries or growth zoning observed by SEM-CL were classified as primary or pseudosecondary. Fluid inclusions within the cross-cutting, lower-intensity fracture pattern were classified as secondary.

The low magnitude and range of homogenization temperatures suggest that the D_4 fracture system was exposed to metamorphic to meteoric fluid along a hydrostatic to hydrothermal geothermal gradient. The range of pressure at constant temperatures for CO_2 inclusions (Fig. 26) suggests growth during protracted cooling under typical hydrostatic conditions with thermal gradients ranging from 30 to 80 °C/km. Salinities range from 0.4 to 9.4%, suggesting local mixing of surface fluids and fluids rising from the zone of regional metamorphism. Quartz crystals may locally contain chlorite habits or rare interstitial chlorite, which may have ions sourced from the zone of greenschist facies metamorphism connected by fluid advection. The depth of vein precipitation ranges from < 1 to 7 km (Fig. 26), which supports a dynamic, tectonic-hydrothermal fluid system and constrains the transition to brittle extension at a depth of ≤ 7 km.

5.11 $^{40}Ar/^{39}Ar$ analysis of adularia

Two samples of adularia were collected for $^{40}Ar/^{39}Ar$ dating from coastal exposures along the Kukutzu Cliffs (Fig. 1). The samples consisted of mm to cm-sized euhedral crystals collected by hand from late-stage veins in the Kanagan gneiss (Lin and Chen 2016). In one of the samples, however, the crystals were coated with microchlorite and appeared dark green. The second sample lacked the chlorite coating and displayed a pearl-white color, which is more typical of the adularia from these outcrops (Fig. 20A) (Huang 1953). Perhaps not surprisingly, the chlorite-coated sample yielded a complex

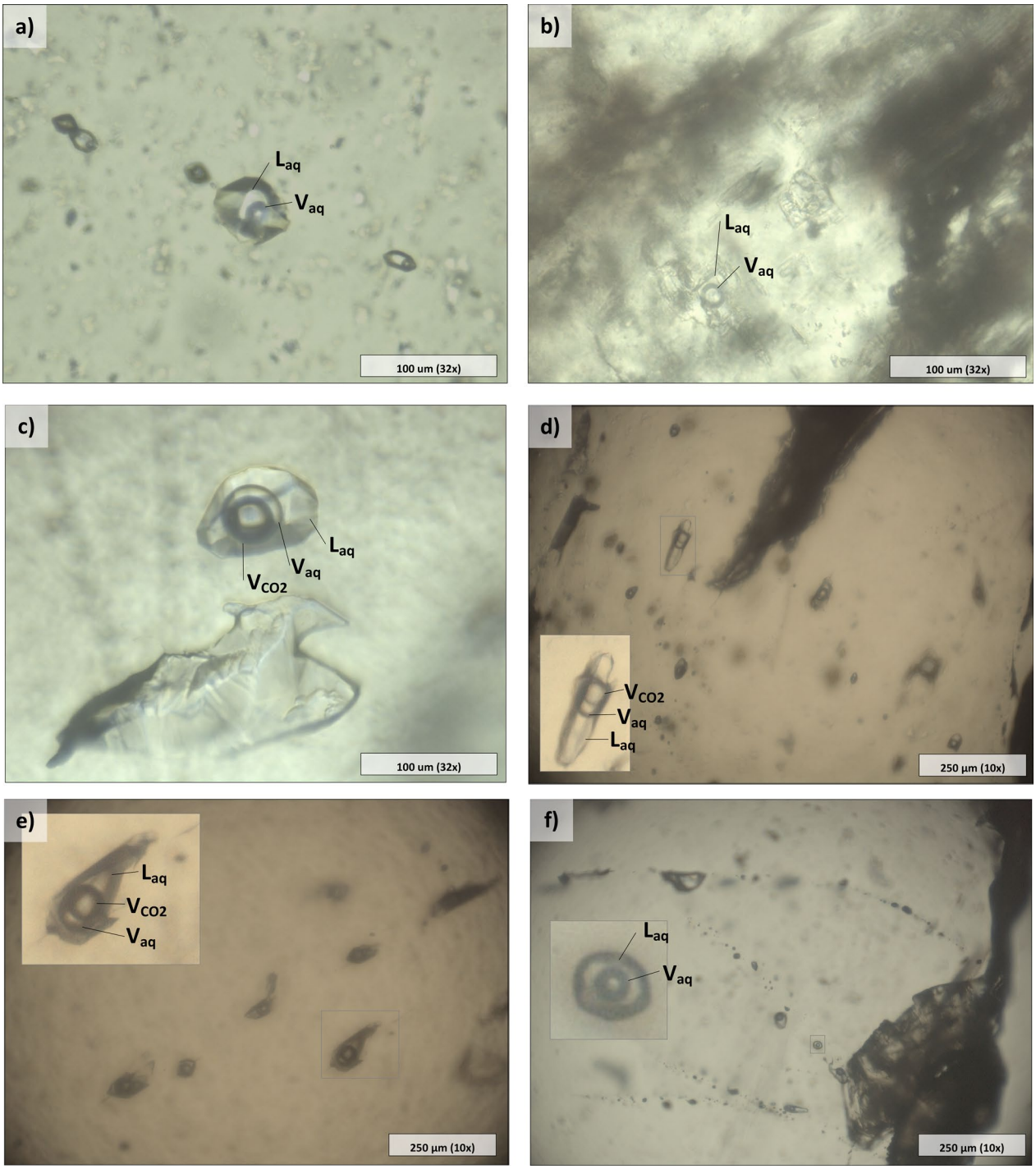

Fig. 24 Photomicrographs of fluid inclusion types found in quartz and adularia crystals from late-stage, D_4, veins from northern (**a** and **b**), central (**c** and **d**), and southern sites (**e** and **f**). Primary, two-phase H_2O-NaCl inclusions in quartz (**a**) and adularia (**b**) from the Kukutsu that display a negative crystal form. **c** and **d** show primary, three-phase H_2O–CO_2–NaCl inclusions in quartz from the central, Shoufeng River, site. One inclusion in **c** was locally decrepitated at 271 °C. Fluid inclusions in **d** show a planar fluid inclusion assemblage H_2O-CO_2–NaCl. **e** Linear fluid inclusion assemblage characterized by pseudosecondary three-phase H_2O–CO_2–NaCl inclusions from the southern, Xinwulu River, site. In **f**, also from the Xinwulu River site, planar fluid inclusion assemblages are characterized by pseudosecondary and sub-contemporaneous secondary two-phase, H_2O–NaCl inclusions

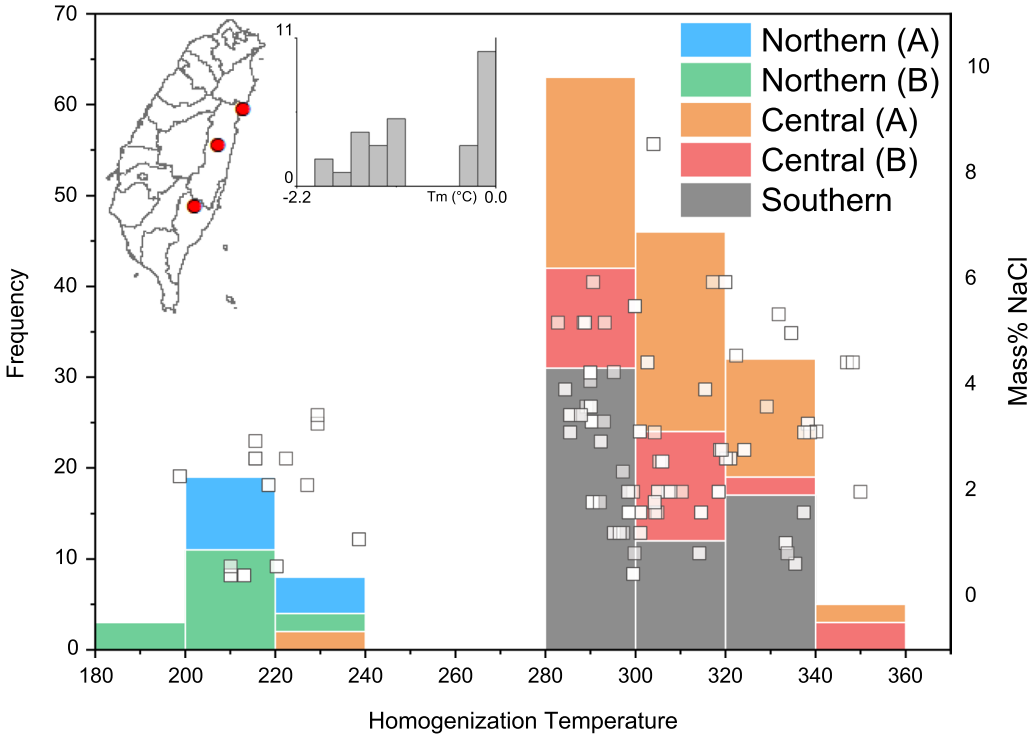

Fig. 25 Bar plot depicting the distribution of homogenization temperatures per sample, including H_2O–NaCl, and H_2O–CO_2 type inclusions, and a scatter plot depicting the weight% of NaCl for the bulk fluid inclusion as determined from the ice melting temperatures shown in the upper bar graph. The left inset map of Taiwan depicts the sample localities (see also red boxes Fig. 1)

degassing history and an inverse isochron with large errors and geologically unreasonable ages. The late-stage veins from which the adularia was sourced are oriented 357°/69° and S_4 dips 48° toward 334° in this area. Mineral paragenesis for the vein fill was commonly quartz + albite + calcite +/− adularia. Microstructural observations and CL imaging of the adularia suggest little post-formation deformation or strain accumulation within the crystal structure (Fig. 22). Sample data tables, step-heating experiments, and inverse isochrons for T19HC-03 are included in Additional file 15: Appendix SIII. All errors are quoted at the one sigma level.

Sample T19HC-01, which lacked the thin chlorite coating, yielded a mean age from three aliquots of 2.38 ± 0.15 (1σ) Ma (Fig. 27). Three single-grain aliquots were analyzed by step heating and resulted in relatively well-defined inverse isochrons with isochron statistically indistinguishable ages of 2.54 ± 0.13 Ma, 2.24 ± 0.13 Ma., and 2.37 ± 0.14 Ma with MSWDs = 2, 105, 7. Apparent age spectra from step-heating runs show older apparent ages within the first 10% of ^{39}Ar released. Intermediate stages show initially anomalously old step(s) followed by a loss profile. Minimum ages associated with the intermediate temperature steps that variably define argon-loss profiles are indiscernible but generally < 1 Ma. Although discordant, one aliquot yielded a weighted mean age of ca 2.3 Ma.

In conjunction with the geologic setting, the step-heating runs suggest that both samples, T19HC-01 and T19HC-03 were affected by partial resetting possibly associated with hot metamorphic fluids propagated through the fractures. Such an influx is also supported by the high geothermal gradients suggested by FIM on quartz and adularia and the lack of notable solid solutions within the adularia as suggested by CL analysis and the sub-concordant nature of the higher temperature steps for most of the runs.

Chen et al. (2022) also dated two samples of adularia from the area of the Kukutsu Cliffs using ^{40}Ar/^{39}Ar and obtained slightly younger inverse isochron ages of 1.09 ± 0.03 Ma and 1.5 ± 0.3 Ma. The available isotopic ages, therefore, show that horizontal extension occurred from c. 2.4–1.1 Ma.

5.12 Kinematics associated with the late-stage structures

A review of outcrop and thin-section observations suggests a low degree of non-coaxial strain (kinematic vorticity < 1.0) during D_4. At all field sites, late-stage veins are consistently at a high angle to S_4 and L_4, suggesting a thinning strain regime and the absence of a significant

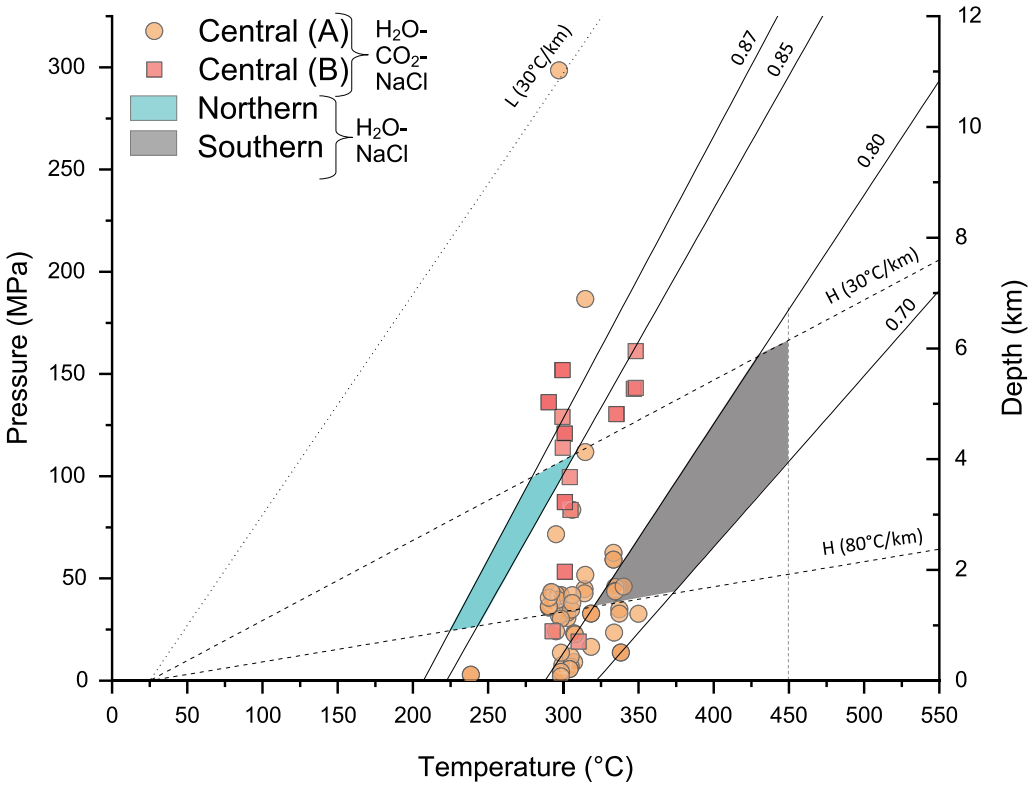

Fig. 26 Scatter plot depicting the minimum entrapment temperature and calculated pressure conditions for H_2O–CO_2–NaCl fluid inclusions. The linear plots are lines of constant density (isochores) for the average density plus/minus one standard deviation for the H_2O–NaCl inclusions with the density listed in g/cm^3. The dashed lines are hydrostatic (H) and lithostatic (L) thermobaric gradients for thermal gradients between 30 and 80 °C/km. The shaded areas define the statistical range (~1σ) of P–T conditions during which the H_2O–NaCl fluids were trapped. The peak temperature of the Yuli Belt is 550 °C (Kouketsu et al. 2019) based on RSCM, which we assume was the maximum entrapment temperature for the fluid inclusions. The maximum entrapment temperature for the southern site was constrained at 450 °C using RSCM (Beyssac et al. 2007). The depth was calculated using an overlying rock density of 2.7 g/cm^3

component of rotational strain (Ring et al. 1999; Feehan and Brandon 1999; Fossen and Cavalcante 2017). In addition, observations parallel to S_4 and L_4 show a sense of shear indicators that are generally weakly to moderately developed, but a top-to-the-south sense of shear is dominant (e.g., Fig. 16e, f). For example, 12 of 17 thin sections preserve well-defined indicators, with 9 recording top-to-the southwest, 2 recording top-to-the northeast, and 1 showing top-to-the northwest (Fig. 28). The sedimentary sequences south of the Yuli also appear to preserve a consistent top-to-the-south sense of shear (Lu and Lee 2001; Conand et al. 2020). The top-to-the-south-southwest sense of shear is consistent with asymmetric structures associated with the pseudotachylite in the northern Tailuko Belt but inconsistent with the sense of shear interpreted for the ductile shear zones in the Slate Belt north of the pseudotachylite (Fig. 2B), after rotations related to the orocline are removed.

6 Discussion

The late-stage veins, cleavages, and ductile shear zones that define the youngest penetrative deformation along the length of the eastern flank of the Backbone Range consistently show vertical shortening and north-to-northeast extension, suggesting that tectonic exhumation played a role in exhuming and cooling the metamorphic core. To evaluate this interpretation, we begin with a discussion of the age of late-stage structures and propose that the structures post-date the formation of S_2 and S_3 in the Tailuko Belt and pre-date the formation of the orocline in the northern Backbone Range. We then consider the transition from D_2, recorded by strike-slip deformation primarily in the Tailuko Belt, and the late-stage structures, delineated as D_4. We propose that this transition marks the westward extrusion of the high-pressure rocks mapped in the Yuli Belt. Extrusion was apparently accommodated by thrust faulting in the west, recognized

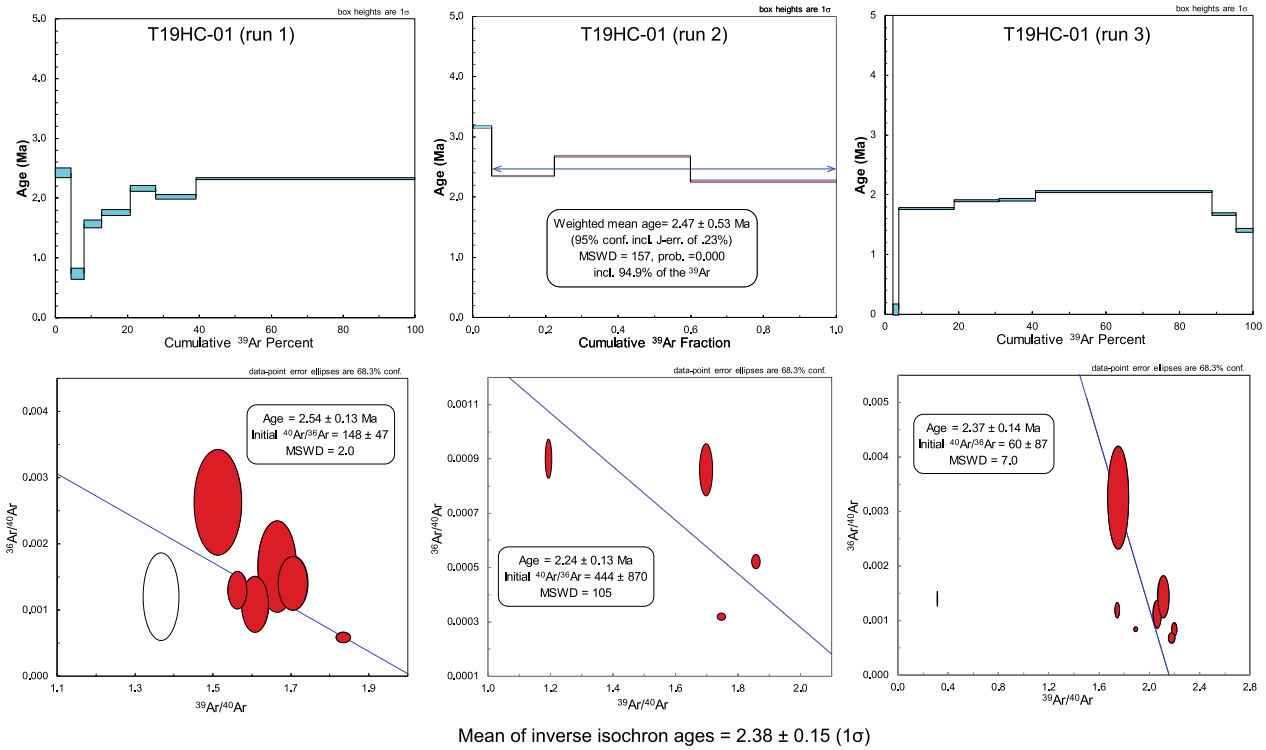

Fig. 27 Ar step-heating and inverse isochrones for three aliquots of sample T19HC-01. See text for discussion. Sample data tables, step-heating experiments, and inverse isochrons for T19HC-03 are included in Additional file 15: Appendix SIII

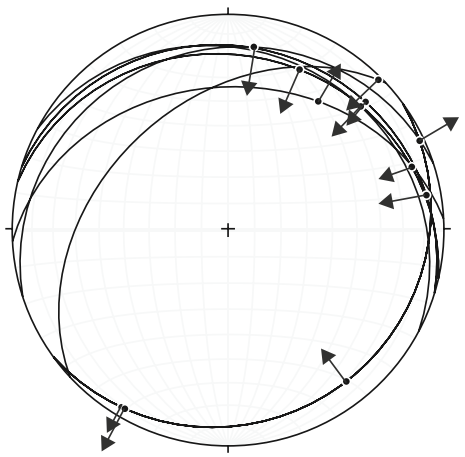

Fig. 28 Mean S_4, L_4 and shear sense associated with S_4/L_4 in XY planes at the river sites in Fig. 21. 12 of 17 samples yielded well-defined indicators, with 9 showing top-to-the-SW, 2 showing top-to-the-NE, and 1 showing top-to-the-NW. A top-to-the-southwest sense of shear is consistent with observations by Lu et al. (2001) and Conand et al. (2020) in the southern Backbone Range

as D_3, and displacement along an extensional shear zone in the east evidenced primarily by a low-dipping foliation and steeply dipping extensional veins, D_4. Although the extensional shear zone remains cryptic, the change from horizontal to vertical shortening throughout the metamorphic core argues that tectonic processes played an important role in the exhumation of the high-pressure rocks in the Yuli Belt.

6.1 Age of the youngest penetrative structures

The relative age of the youngest penetrative fabrics in the eastern Backbone Range varies across different tectonic units, although the fabrics have similar geometries and kinematics. For example, the sedimentary rocks south of the Yuli Belt, including the exposures along the Zhiben River and Domain II of Conand et al. (2020) preserve a single penetrative foliation and lineation, S_1 and L_1, and a suite of late-stage mineral-filled veins. Further north and east of the Yuli exposures, along the eastern section of the Chingsuei River, and along a short stretch of Hwy 30, the sedimentary sequences preserve two foliations that we interpret as S_1 and S_2. Mondro et al. (2017), mapping more regionally but in correlative rocks (i.e., the Chulai and Hsinkao Formations), also documented two penetrative events. The two events are recorded by two sets of fibrous strain fringes, with the early formed set recording generally west-northwest to east-southeast stretching and the later set recording east-northeast to west-southwest stretching. We propose that these stretching events

correlate with S_1 and S_2 documented along the eastern Chingsuei River. Further west in the higher-grade metamorphic rocks of the Yuli and Tailuko Belts, S_3 is also present, and the youngest foliation, S_4, dips gently north and is associated with northeast stretching.

Based primarily on the geometry and kinematics of the structural fabrics and the absence of detailed stratigraphic control, we propose an accretionary prism model where more deeply buried rocks are more deformed. During exhumation, units with more protracted deformation histories can be juxtaposed next to less deformed rocks, and both suites may then experience a relatively young deformation event that "stitches" the units. In this context, S_4 in the Yuli and Tailuko Belts is the "stitching" event recorded as S_2 in the Chulai and Hsinkao Formations and as S_1 in the low-grade rocks south of the Yuli.

Isotopic ages and cross-cutting relations of dated events constrain the absolute age of the youngest structures. For example, the gently dipping foliation, extensional shear zones, and veins consistently cross-cut the S_2 mylonite in the Tailuko Belt, which ranges in age from 4.0 to 3.1 Ma based on $^{40}Ar/^{39}Ar$ dating (Wang et al. 1998). We infer, therefore, that 3.1 Ma represents the maximum age of the youngest structures. Several of the structures included in the suite of youngest structures, e.g., a low-angle pressure solution fabric, extensional veins, and shear zones, have also been rotated by the orocline in northern Taiwan, which appears to have started forming ~1.0 Ma., providing a minimum age for the youngest structures. This range for the maximum and minimum age is consistent with three $^{40}Ar/^{39}Ar$ ages of adularia collected from the late-stage veins, 2.4 +/−, Ma (this study), 1.5 Ma +/− and 1.1 +/− Ma (Chen et al. 2022), with a $^{40}Ar/^{39}Ar$ determined age of pseudotachylite of 1.6 Ma that fills a suite of extensional fault zones (Chen et al. 2017a) and $^{40}Ar/^{39}Ar$ ages of mica from the Daguan shear zone, ~0.7 Ma which cross-cuts S_3 (redefined here as S_4) in the Yuli Belt (Yi et al. 2015). We therefore propose that the suite of relatively young structures in the eastern Backbone Range formed between ~2.4 and 0.7 Ma, with deformation possibly starting as early as ~3.1 Ma.

6.2 Exhumation history

A full understanding of the exhumation of the high-pressure rocks in the Yuli Belt from their estimated depth of ~50 km is beyond the scope of this paper. However, we recognize three processes that may have driven over thickening in the rear of the wedge and led to the transition to structural thinning implied by geometry and kinematics of the late-stage structures: (1) changes in local buoyancy by chemical and phase changes (e.g., hydrated blocks of mantle), (2) crustal-scale pressure gradients in a subduction channel during continuous subduction, and (3) changes to the thickness and composition of the subducting crust (Fossen 2010; Warren 2013). Our preference is for (3), although (1) and (2) may have also played a role. We favor (3) primarily because regional compilations of low-temperature geochronologic data from the metamorphic core show the formation of a major out-of-sequence thrust, the Tayuling thrust, at ~6 Ma (Fig. 2 site M)(Lee et al. 2022b), and the thrust carries the Tailuko Belt in its hanging wall, arguing for the incorporation of Eurasian continental crust (i.e., SE China) at this time (Lan and Liou 1981; Dewangga et al. 2021; Lee et al. 2022b). This interpretation is also consistent with the recent documentation of Taiwan-derived sediments arriving in the foreland basin in the Late Miocene to Early Pliocene, ~5–4 Ma (Hsieh et al. 2023). We, therefore, propose that subduction of thick continental crust (e.g., equivalent to the Tailuko Belt) ~6–5 Ma initiated exhumation of the high-pressure rocks (Yuli Belt). Continued exhumation is documented with isotopic ages of retrograde metamorphism, including a 4.4 ± 0.1 Ma age of phlogopite using $^{40}Ar/^{39}Ar$, (Lo and Yui 1996) and a 3.3 ± 1.7 Ma age for zircon in a clinozoisite vein in nephrite using U/Pb (Yui et al. 2014). This documented decrease in timing is followed by the initiation of structural thinning at ca. 2.4 Ma.

Fluid inclusion microthermometry, vein textures, and $^{40}Ar/^{39}Ar$ age analyses on adularia collected from the late-stage veins provide additional information on structural thinning during the ductile to brittle transition. For example, grain morphologies within the veins indicate they developed under an extensional stress regime between < 1 and 7 km, with a maximum depth for mineral precipitant ranging from 4 to 7 km. The decrease of pressure at constant temperatures, as recorded by FIM, suggests continued brittle/ductile deformation as the rock package was exhumed through the hydrothermal fluid system. Once the overburden was reduced enough to allow the fractures to remain open, well-developed euhedral crystals grew in open voids, or the veins were filled with equant blocky grain morphologies, probably at depths between 0 and 2 km depth. This transition is also suggested by the change from crack-seal vein material near the walls of the veins to euhedral crystals in the vein centers. Secondary fluid inclusions at similar trapping conditions were likely formed within the crystals during the protracted cooling. The cessation of the fluid system is represented by the deposition of soluble ions in the form of chlorite, ankerite, calcite, and gold deposits (Craw et al. 2009). If we assume that the adularia crystals formed before the transition to lithostatic to hydrostatic conditions (e.g., 2–7 km) at 2.38 Ma, tectonic thinning and erosion rates of between 0.8 and 3 km/Myr would be needed to remove the overburden. Using the younger

$^{40}Ar/^{39}Ar$ age of ~1.1 Ma for adularia growth suggests significantly faster rates of 1.8–6.3 km/Myr.

6.3 Extrusion and changing structural regimes

An important but often overlooked consequence of tectonic extrusion in a subduction zone is that the horizontal motions of the extruding blocks can add to the shortening associated with plate convergence (Chemenda et al. 1995; Warren et al. 2008). This additional shortening component could be accommodated in the fold-and-thrust belt and even equal the extension in the rear of the wedge (Chemenda et al. 1995; Warren et al. 2008). In Taiwan, tectonic exhumation of the Yuli Belt driven, for example, by pressure gradients in the subduction channel, could have accelerated slip along the decollement beneath the accretionary wedge west of the Yuli Belt, essentially pushing the wedge westward.

To better understand how this process may apply to Taiwan, we start with a reconstruction of the tectonic setting near the end of D_2 in the Tailuko Belt (Fig. 29A). We have removed the oroclines in northern and southern Taiwan and consider the orogen a relatively straight system consistent with regional-scale strike-slip (Ho et al. 2022). During D_2, highly oblique plate convergence was accommodated through deformation partitioning (Fitch 1972; McCaffrey 1992) with orogen-normal shortening in the Slate Belt and orogen-parallel strike-slip in the Tailuko Belt (Ho et al. 2022). For the D_2 strike-slip regime, we envision a relatively simple instantaneous strain state where the minimum stretch, S_3, trends northwest, parallel to the plate convergence vector, the intermediate stretch, S_2, is vertical, and the maximum stretch, S_1, trends northeast (Fig. 29C).

Near the end of D_2, we propose that the westward extrusion of the Yuli Belt caused a significant change in the tectonic regime (Fig. 29). In this interpretation, extrusion is accommodated by slip along two east-dipping, regional-scale structures: the Shoufeng thrust that crops out west of the Yuli Belt and carries the Yuli Belt in its hanging wall and a more cryptic extensional shear zone that we propose carries the Luzon forearc in its hanging wall (Fig. 29B). We also propose that extrusion of the Yuli Belt offset the pre-existing Tailuko shear zone left-laterally along a generally east–west trending fault, forming a regional-scale releasing bend (Fig. 29B). The Chouchi Fault in the central part of the Yuli Belt may represent a similar but less well-developed cross-structure ("G" in Fig. 2). As oblique convergence continued, the state of strain in area of the releasing bend changed from thrusting and thickening (i.e., large vertical stretch) (Fig. 29C, D_3) to vertical thinning and strike-parallel extension (Fig. 29C, D_4) . That is, formation of the releasing bend generated an area of low vertical stretch that accommodated vertical extrusion of the Yuli Belt.

In support of this proposed change in regimes, we note that slip on the Chaochou thrust (Fig. 2) may have accommodated the westward displacement associated with extrusion of the Yuli Belt. For example, the unusual north–south strike of the Chaochou Fault (see Figs. 1, 2) may reflect progressively lower slip, or slip rates, from north to south along the fault. The presence of a regional-scale, late-stage (i.e., post-cleavage) antiform in the northern extent of the Chaochou hanging wall (Huang and Byrne 2014) is consistent with larger slip along the fault in the north. Progressively lower slip north to south also correlates with the narrowing of exposures of the Yuli Belt in the core of the orogen consistent with the notion that westward extrusion of the Yuli Belt added to the slip along the Chaochou. Finally, cooling ages of reset detrital apatite grains from the hanging wall of the fault range from 3.6 to 2.4 Ma, which overlap with exhumation cooling ages in the Yuli Belt (Lo and Yui 1996) and slightly pre-date initiation of northeast extension recorded by the late-stage veins that date from 2.4 to 1.1 Ma (this paper and Chen et al. 2022).

(See figure on next page.)

Fig. 29 Generalized maps, cross sections, and strain states for the Tailuko and Yuli Belts as they are accreted/subducted and extruded. **A** ~6.0–3.0 Ma, accretion of Tailuko and Slate Belts and subduction of Yuli Belt as continental crust of Eurasia enters the Luzon subduction zone. Kinematics and strain partitioning along the plate boundary are from Ho et al. (2022). Schematic cross section *X*–*X'* at the time shown in **A**. **B** ~3.0–0.7 Ma, vertical and westward extrusion of the Yuli Belt accommodated by reactivation of the Tailuko strike-slip shear zone as a high-angle reverse fault, the Shoufeng shear zone (SSZ). Westward extrusion accelerates slip on the Chaochou Fault (CF in cross section) and offsets the left-lateral shear zone in the Tailuko Belt, creating a left-stepping releasing bend. Geochronologic data suggests northeast stretching (black arrows) started ca. 2.4 Ma (this study). The location of reconstructed units relative to Taiwan is for general reference. **C** General strain states for three deformation stages with "*S*" representing the stretch ($S = 1 +$ elongation) for each of the principal strains with $S_1 > S_2 > S_3$. D_2: strike-slip deformation in the Tailuko Belt during oblique convergence and strain partitioning (Ho et al. 2022). D_3: east-dipping high-reverse fault between Tailuko and Yuli Belts (represented by red dashed and continuous lines). Orientations and relative magnitude of stretches are poorly known, but maximum stretch S_1 is assumed to be nearly vertical. D_4: vertical thinning and extrusion of the Yuli Belt that minimizes the vertical stretch while the releasing bend during oblique convergence maximizes the horizontal stretch. Black dashed line represents late-stage foliation. Note that the maximum stretch trends northeast for D_2 and D_4

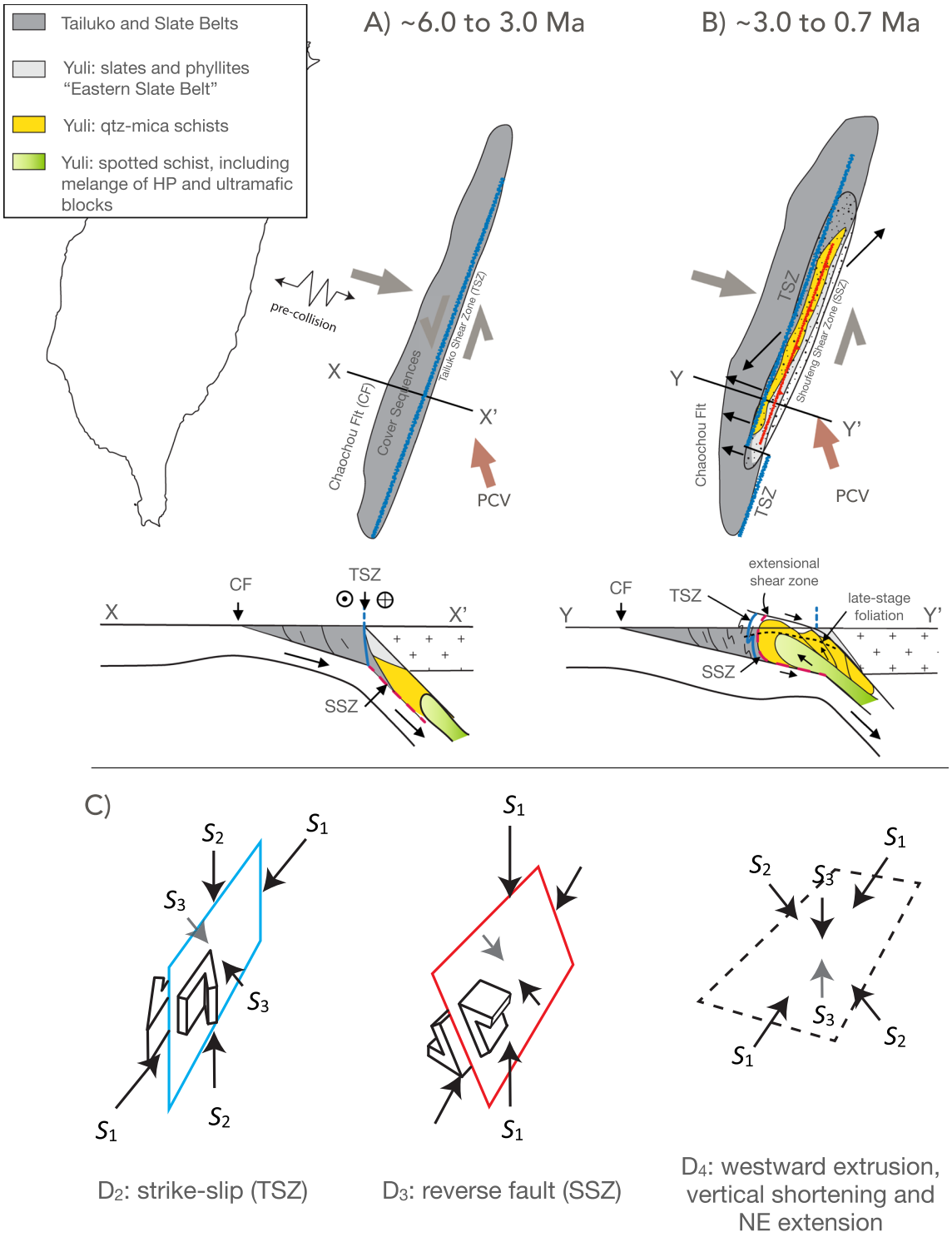

Fig. 29 (See legend on previous page.)

Westward displacement of the Tailuko shear zone as the Yuli Belt was extruded may also explain the limited evidence for left-lateral slip in the area south of the southernmost exposures of the Tailuko Belt. For example, the only detailed geologic map of this area that we are aware of (Usami and Matsumoto 1940) shows two left-lateral strike-slip faults on the east and west sides of the Tailuko outcrops (Fig. 2 site N). However, map-scale

offsets across the faults suggest that they accommodated relatively small displacements. The eastern fault displaces an anticline-syncline pair 2–3 km, and this fault is itself offset 1–2 km by the second left-lateral fault, suggesting a total slip of ~5 km. Conand et al. (2020) show a regional-scale, left-lateral fault that generally follows the west boundary of the Tailuko Belt, although only the northern and southern extents have been mapped. Several smaller, north-striking left-lateral faults have also been mapped in this area (Lu and Lee 2001; Mesalles 2014), but none of these faults have documented offset, and the ages of slip are generally unknown.

Considering that the Tailuko shear zone is interpreted to be part of a plate boundary, the total slip is expected to be much larger than the observed 5 km (Usami and Matsumoto 1940). One option is distributing displacements related to the Tailuko shear zone throughout the southern backbone range. Alternatively, the westward motion of the Chaochou, which carries the Tailuko Belt in its hanging wall, raises the possibility that the westward motion of the extruding Yuli Belt offset the Tailuko shear zone. This interpretation is attractive because the highly linear coastline in southeast Taiwan suggests a strike-slip deformation history. In fact, Zhang et al. (2022), following Lewis et al. (2015) have recently proposed that the Luzon Trough, which merges with the Longitudinal Valley in Taiwan, is, at least in part, a pull-apart basin between two left-lateral strike-slip faults. The western basin-bounding fault recognized by Zhang et al. (2022) is equivalent to the southern extent of the Tailuko shear zone we are proposing here. Westward offset of the Tailuko shear zone is an attractive interpretation because it would also result in a left-stepping, left-lateral fault system (Fig. 29B), which predicts northeast-southwest extension in the northeast quadrant (Fig. 29B), analogous to a pull-apart basin. This structural setting is consistent with the kinematics of D_4 in the Yuli and Tailuko Belts.

In summary, the late-stage structures in the Tailuko and Yuli Belts and parts of their sedimentary covers appear to reflect vertical shortening and horizontal extension associated with the extrusion of the Yuli Belt. Vertical shortening reflects the vertical ascent of the extruding mantle, probably accentuated by a pre-existing, steep strike-slip fault (see, e.g., Mann and Gordon 1996; Avé Lallemant and Guth 1990; Platt 1983). Horizontal extension developed as the Yuli Belt was extruded westward up the subduction zone, offsetting the north-striking Tailuko shear zone left-laterally. This new structural setting created a left-stepping, left-lateral shear zone and a regime of regional-scale extension in its northeast corner (Fig. 29). Westward extrusion of the Yuli Belt was accommodated by additional slip along the Chaochou thrust along the western flank of the orogen.

6.4 Structural thinning

The magnitude of tectonic exhumation during the youngest penetrative event can be estimated using the finite strain values obtained in the lower-grade sequences of the metamorphic core (Mondro et al. 2017), although the uncertainties are relatively large. The strain data show a mean, generally horizontal stretch of 4, which, assuming constant volume and plane strain, is equivalent to a vertical stretch of 0.25 and indicates vertical shortening of 75%. Assuming a 30 km thick accretionary prism, a sub-horizontal foliation, and a uniformly distributed vertical strain rate, vertical shortening would account for over 20 km of tectonic exhumation. The relatively young event also appears to have been active for ~1.3 Myr (i.e., from ~2.4 to 1.1 Ma), indicating an exhumation rate of ~15.4 km/Myr, which seems unreasonably high.

There are several critical unknowns in estimating tectonic exhumation from the strain data. Ring and Kumerics (2008) and Feehan and Brandon (1999) argue that strain values collected from exposed high-pressure terranes typically significantly overestimate the amount of crustal thinning. This is because we know very little about strain rate laws or the distribution of strain at depth, and rocks can travel relatively quickly through zones of high strain rates as they are exhumed. For example, Ring and Kumerics, (2008) used a strain rate law that increased proportionally with depth to estimate the exhumation of high-pressure rocks in the Alboran Sea (exhumed from 40 km, Platt et al. 1998) and concluded that vertical stretches of 0.03 were required. This relatively high value implies strain ratios of ~1000, which Ring and Kumerics considered unrealistic.

Although the vertical stretch observed in Taiwan, 0.25, is substantially lower than the calculated value for high-pressure rocks in the Alboran Sea, the estimated exhumation rates in Taiwan of ~15.4 km/Myr are unreasonable. If we assume vertical shortening started at the end of mylonitization associated with S_2 in the Tailuko Belt, or about 3.1 Ma, the tectonic exhumation rate for a 30 km thick crust would still be 10 km/Myr, which is also relatively high.

One alternative is to assume that vertical shortening represents strain associated with a regional-scale detachment or shear zone with a finite width (e.g., Fig. 29C, D_4). If we assume, for example, that the observed horizontal stretch value, ~4, represents strain that accumulated as the rocks moved through the range of pressures and temperatures indicated by the fluid inclusion data, ~5 km, a horizontal stretch of 4 would remove 3.75 km of overburden and imply an exhumation rate of 2.9 km/Myr. This rate is comparable to modern rates of erosion in Taiwan (Dadson et al. 2003; Derrieux et al. 2014).

A regional-scale, east-dipping detachment, as shown in Fig. 29C, D_4, is attractive as it provides an explanation for CW rotation (north view) of older fabrics (e.g., red dashed line in Fig. 29B) (Crespi et al. 1996), the CW rotation of the Yuli-Chulai contact (see Fig. 5, Stanley et al. 1981) and the top-to-the-east shear observed the lower-graded metamorphosed sedimentary rocks east and southeast of the Yuli Belt (Lu and Lee 2001). Remnants of the detachment may also be preserved at the base of the mafic/ultramafic blocks at Wanrong (Fig. 2 between the Shoufeng and Hongye Rivers) and Ruisui (Fig. 2 at the latitude of the Hongye River) that are mapped as tectonic klippe perched anomalously above other members of the Yuli Belt (Lin 1999b; Yen 1983; Yang and Wang 1985). Finally, a gently dipping detachment with a normal sense of shear would accentuate exhumation cooling.

6.5 Implications for topographic growth

Considering the possible importance of both tectonic and surface processes in exhumation, we evaluate the possibility that these processes outpaced rock uplift and limited the topographic growth of the orogen, at least to the end of the youngest, penetrative deformation in the Tailuko and Yuli Belts, ~0.7 Ma. We evaluate this possibility by showing a correlation between the age of the late-stage deformation in the metamorphic rocks and the results of a recent study documenting the paleotopography of the Backbone Range (Fig. 30) (Chang et al. 2023). The paleotopography analysis used the H isotope record of n-alkanes with 29 carbon atoms (δ^2H_{nC29}) preserved in leaf waxes collected from exposed sedimentary rocks in the Coastal Range. The sediments form part of an uplifted forearc basin that accumulated sediments derived from both the magmatic arc to the east and the emerging orogenic belt to the west from ~4.0 to 0.7 Ma. A younger terrace deposit < 0.5 Ma was also sampled. The δ^2H_{nC29} values are consistently high from 3.0 to 1.25 Ma with a mean of -160 ($^0/_{00}$) and decrease slightly to a mean of ~− 180 ($^0/_{00}$) ~1.0 Ma. A final drop to − 200 ($^0/_{00}$) at 0.3 Ma (Fig. 30). Chang et al. (2023) modeled the H data using a modern Taiwan reference and proposed that mean source elevation grew from a few hundred meters 3.0–1.25 Ma, to 1.5 km ~1.0 Ma and reached its current mean elevation of just over 2.5 km < 0.5 Ma (Fig. 30). These data strongly argue that topographic growth was limited despite clear evidence of significant erosion (e.g., high deposition rates) during this time. One interpretation, therefore, is that tectonic thinning of the eastern Backbone Range played an important role in limiting topographic growth.

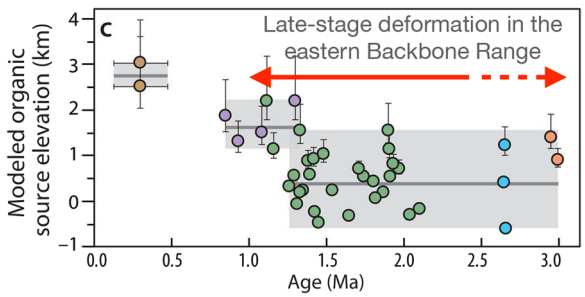

Fig. 30 Modeled elevation for the source of organic materials versus age (from Chang et al. 2023). The age range of late-stage deformation in the eastern Backbone Range is based on isotopic ages and bending of the northern Backbone Range orocline (this study)

A relatively low elevation for the Backbone Range until very recently is also consistent with preserving areas of anomalously low relief in the Backbone Range, some perched at high elevations today. The areas of anomalous topographic relief were first described by Japanese researchers a century ago (Lin 1957 and references therein). They ascribed the surfaces to the decay and rejuvenation of tectonic activity, generally following ideas proposed by Davis (1899). Lin (1957) resurrected this hypothesis, and Ouimet et al. (2013), based on ^{10}Be isotope data from the surfaces and the steep scarps often surrounding the surfaces, documented extremely low erosion rates on the surfaces and extremely high rates on the eroding flanks. Yang et al. (2015) proposed that the low-relief surfaces could form during stream piracy and headwater migrations, although Whipple et al. (2017) questioned the significance of these processes. More recently, Hsieh et al. (2018) presented one of the most detailed studies of one of the largest surfaces in Taiwan, the Alishan surface, and showed that the surface formed > 50 ky ago (the maximum age of 14C), probably during the last glacial period. They propose that during relatively dry glacial periods, river downcutting decreases and hillslopes degrade, potentially forming areas of relatively low relief. Similar processes may have been operating throughout Taiwan, including the eastern Backbone Range, where tectonic exhumation may have played a role in limiting surface uplift. However, the low-relief surfaces in the Backbone Range remain undated, and additional research is needed to verify their origin (Additional file 16).

7 Conclusions

Integration of previous studies of the metamorphic core in the Taiwan orogen with new structural, geochronologic, and thermometric data suggests a new interpretation for the arc-continent collision. We propose a two-stage process for exhuming the high-pressure metamorphic rocks of the core of the orogen. In the initial stage, exhumation is driven primarily by pressure gradients in a subduction channel, possibly enhanced by

partial subduction of continental crust. During this stage, exhuming rocks are tectonically extruded up the subduction channel with vertical and horizontal components. The horizontal component drives the second stage. During this stage, a previously recognized, margin-parallel, left-lateral strike-slip system is offset, forming a left-stepping extensional bend as oblique convergence continued. The extruding high-pressure rocks filled this extensional zone as the hanging wall was structurally thinned.

The primary evidence for the new interpretation is the regional distribution of a late-stage, gently dipping penetrative foliation and a suite of sub-vertical veins. Isotopic dating and cross-cutting relations indicate this exhumation stage extended from ca. 2.4 to < 1.0 Ma when the Backbone Range orocline started to form. Combined tectonic and erosional processes may have limited the topographic growth of the orogen from ~3.0 to < 1.0 Ma. We propose that the late-stage, gently dipping foliation and steeply dipping veins formed in the footwall of a regional-scale, extensional shear zone rooted to the east beneath the forearc (Fig. 29B). Normal slip on the detachment accounts for CW rotation (north view) of older foliations that represent the eastern half of an apparent cleavage fan in the Backbone Range (red dashed line in Fig. 29B, cross section) and the local occurrence of top-to-the-east shear previously interpreted as evidence for back thrusting.

The proposed hypothesis could be further developed and tested with additional structural and geochronological data. In particular, the southern Backbone Range, where the margin-parallel strike-fault appears to be offset, is ripe for more detailed, integrated studies. Perhaps one of the most challenging areas of future study is identifying and mapping remnants of the proposed extension shear zone that accommodated the westward extrusion of the orogenic wedge. Future studies incorporating low-temperature geochronometers and surface processes could also better define the link between the inactive structures described here and active structures that define the tectonic regimes of modern Taiwan. Finally, we assumed highly oblique plate convergence throughout the different deformation regimes because it is consistent with strike-slip deformation during D_2, northeast extension during D_4, and recent reconstructions based on tomographic data (Wu et al. 2016; Sibuet et al. 2021). Presumably, highly oblique convergence transitioned to the modern, more orthogonal convergence before the northern Backbone Range orocline was initiated ~1 Mya. Linking plate motions to past and modern tectonic regimes is also an area ripe for more detailed studies.

Abbreviations

AFT	Fission track dating of apatite grains
AHe	U-Th/He dates of apatite grains
C	Centigrade
CCW	Counterclockwise
CW	Clockwise
CF	Chaochou fault
CL	Cathodoluminescence
CR	Coastal range
CXIH	Central Cross-Island Highway
D_x	Deformation event with $x=1$, 2, 3, or 4, reflecting the relative age of different deformation events that include various tectonic structures, except S_0, which represents bedding
EUR	Eurasian Plate
FIM	Fluid inclusion microthermometry
L/V	Liquid/vapor
Ma	Millions of years before present
Myr	Millions of years
PCV	Plate convergence vector
PSP	Philippine Sea Plate
RA	Ryukyu arc
RSCM	Ramen spectrometry of carbonaceous material
SEM-BSE	Scanning electron microscope and backscattered electrons
SEM-CL	Scanning electron microscope with cathodoluminescence
SEM–EDS	Scanning electron microscope and energy-dispersive X-ray spectroscopy
S_x (italics S)	Stretch direction with $S=1+e$ and $e=$(final length-initial length)/initial length and $S_1>S_2>S_3$
S_x	Foliations with $x=0$, 1, 2, 3, or 4, reflecting the relative age of different foliations
SXIH	South Cross-Island Highway
TSZ	Tailuko Shear Zone
X, Y, and Z	Principal strain axes
XPL	Cross-polarization
ZrnFT	Fission track dating of zircon grains
ZrnHe	U-Th/He dating of zircon grains

Supplementary Information

The online version contains supplementary material available at https://doi.org/10.1186/s40645-024-00627-w.

Additional file 1. Appendix I: Methods for collecting samples and structural and petrographic analyses.

Additional file 2. Appendix II: Methods for fluid inclusion microthermometry (FIM).

Additional file 3. Appendix II: FIM Table 1a, fluid inclusion petrographic and microthermometric observations.

Additional file 4. Appendix II: FIM Table 1b, fluid inclusion petrographic and microthermometric observations.

Additional file 5. Appendix II: FIM Table 1c, fluid inclusion petrographic and microthermometric observations.

Additional file 6. Appendix II: FIM Table 2a, fluid inclusion microthermometry results as calculated in fluids.

Additional file 7. Appendix II: FIM Table 2b, fluid inclusion microthermometry results as calculated in fluids.

Additional file 8. Appendix II: FIM Table 2c, fluid inclusion microthermometry results as calculated in fluids.

Additional file 9. Appendix II: Description of maps used to approximate the shape of each sample chip used for FIM.

Additional file 10. Appendix II: Map 1, sample T19H-Q, northern domain.

Additional file 11. Appendix II: Map 2, sample T19H-ADL, northern domain.

Additional file 12. Appendix II: Map 3, sample S1-A (quartz), central domain.

Additional file 13. Appendix II: Map 4, sample S1-B (quartz), central domain.

Additional file 14. Appendix II: Map 5, sample Xin05 (quartz), southern domain.

Additional file 15. Appendix III: 40Ar/39Ar step-heating and inverse isochrons for the chlorite-coated adularia sample T19HC-03.

Additional file 16. Appendix III: 40Ar/39Ar data tables for adularia sample 19THC-01.

Acknowledgements
The authors are extremely grateful for the support and encouragement from our friends and colleagues in Taiwan. This has been a multi-year project with many logistical and scientific challenges. We are especially grateful to Dr. Wen-Yen Chang, Dean of the School of Environment at National Dong Hwa University, who helped secure a very comfortable office and apartment for TB in 2021. A long-weekend car rental was also appreciated. Graduate students at NDHU were especially inviting and patient during research meetings in their research lab. Chih-Ying Yeh, in particular, was a great help as she transitioned from graduate student to lab technician. Ph.D. students Wen-Han Lo and Dominikus Deka Dewangga at NDHU kindly shared their research ideas and observations, and Wen-Han led a critical expedition to the deepest parts of the high-grade rocks along the Chingsuei River. Dr. Sun-Lin Chung, Director of the Institute of Earth Sciences, provided much-needed logistical support and encouragement to work on "S3" in the Yuli Belt. Wei-Hao Hsu and Chiou-Lien Chang "Zinc," graduate students at National Taiwan University, helped with collecting samples at Kukutsu Cliffs. Chi-Hsiu Pang and Kai-Hsiang Yang, graduate students at the Institute of Earth Sciences helped in the field on several occasions and provided stimulating discussions on the geology of Taiwan, and the Yuli Belt in particular. Lindsey Adam Cromwell, Lauren Donati, Ross Bolesta, Susie Adams, Morgan Spatz, and Ben Falvo, all enthusiastic undergraduate students at IUP, assisted in the field for at least two field seasons while supported by NSF award EAR1650157 to JCL. Many additional undergraduate students from universities and academic institutions in Taiwan also participated in the field expeditions and always provided comfortable and entertaining field excursions. Professional field guides secured our safety on many occasions and made delicious meals, often on the bank of the river in the middle of nowhere. Rick Allmendinger's *Stereonet* program was an essential tool throughout the study and is greatly appreciated. Blake Restelli, RJ Lee Group, and Emily Peterman, Bowdoin College, provided professional guidance in preparing sections for SEM and CL analysis. Christopher McDonald, Arizona State University, provided critical assistance in interpreting the Ar/Ar geochronology.

Author contributions
TB, JCL, and J-CL conceived and designed various aspects of the research. MC collected field and thin-section data and analyzed the fluid inclusions. G-RH collected field data, led field expeditions, and participated in data interpretations. Y-HL and E-CY collected field data and provided critical insights into the structural history of the Yuli and Tailuko Belts. C-H Tsai provided expertise in metamorphic petrology and assistance and guidance in the SEM lab at NDHU. ME assisted in fluid inclusion analysis and interpretation. LW collected and analyzed the 40Aar/39Ar data. TB led the writing with contributions from MC, JW, J-CL, ME, C-HT, and LW.

Funding
The research was supported by Grants from the Ministry of Science and Technology (MOST) of Taiwan (MOST 107-2116-M-001-026-MY3; MOST 110-2116-M-001-004 to Jian-Cheng Lee and MOST 109-2811-M-259-513 to Chin-Ho Tsai) and the US National Science Foundation (EAR-1220453 to Byrne; EAR-1650157 to Lewis).

Availability of data and materials
The article and the appendices include the data supporting the conclusions presented here.

Declarations

Competing interests
The authors declare no competing interests.

Received: 4 September 2023 Accepted: 6 April 2024
Published online: 17 April 2024

References

Avé Lallemant HG, Guth LR (1990) Role of extensional tectonics in exhumation of eclogites and blueschists in an oblique subduction setting: northwestern Venezuela. Geology 18:950–953. https://doi.org/10.1130/0091-7613(1990)018%3c0950:ROETIE%3e2.3.CO;2

Baziotis I, Tsai CH, Ernst WG, Jahn BM, Iizuka Y (2016) New P-T constraints on the Tamayen glaucophane-bearing rocks, eastern Taiwan: Perple_X modelling results and geodynamic implications. J Metamorph Geol 35:35–54

Beyssac O, Simoes M, Avouac J-P, Farley K, Chen Y-G, Chan Y-C, Goffe B (2007) Late Cenozoic metamorphic evolution and exhumation of Taiwan. Tectonics 26:TC6001. https://doi.org/10.1029/2006TC002064

Bons PD (2000) The formation of veins and their microstructures. In: Stress, strain and structure: a volume in honor of W. D. Means, vol 2. Australia. https://doi.org/10.3809/jvirtex.2000.00007

Chan Y-C, Okamoto K, Yui T-F, Iizuka Y, Chu H-T (2005) Fossil fluid reservoir beneath a duplex fault structure within the Central Range of Taiwan: implications for fluid leakage and lubrication during earthquake rupturing process. Terra Nova 17(6):493–499. https://doi.org/10.1111/j.1365-3121.2005.00636.x

Chang C-P, Angelier J, Lu C-Y (2007) Polyphase deformation in a newly emerged accretionary prism: folding faulting and rotation in the southern Taiwan mountain range. Tectonophysics. https://doi.org/10.1016/j.tecto.2007.11.002

Chang CP, Angelier J, Huang CY (2009) Evolution of subduction indicated by melanges in Taiwan. In: Lallemand S, Funiciello F (eds) Subduction zone geodynamics. Springer, Berlin, pp 207–225. https://doi.org/10.1007/978-3-540-87974-9

Chang Q, Hren M, Lai LS-H, Dorsey R, Byrne T (2023) Rapid topographic growth of the Taiwan orogen since 1.5 Ma. Sci Adv. https://doi.org/10.1126/sciadv.ade6415

Chemenda AI, Mattauer M, Malavieille J, Bokun A (1995) A mechanism for syn-collisional rock exhumation and associated normal faulting: Results from physical modelling. Earth Planet Sci Lett 132:225–232

Chen C-H (2000) Geologic Map of Taiwan. Central Geological Survey, Ministry of Economic Affairs

Chen WS, Chen YC, Yu NT, Yen IC, Yang BCC, Shih TS (2005) Stratigraphic and tectonic geomorphic studies along the Chao Chou fault, Southern Taiwan-Reevaluating fault characteristics and location. Spec Publ Cent Geol Surv 16:75–90

Chen C-T, Wu C-Y, Lo C-H, Chu H-T, Yui T-F (2017a) Dating palaeo-seismic faulting in the Taiwan Mountain Belt. Terra Nova 30:146–151. https://doi.org/10.1111/ter.12319

Chen WS, Chung S-L, Chou H-Y, Zugererbai Z, Shao W-Y, Lee Y-H (2017b) A reinterpretation of the metamorphic Yuli belt: evidence for a middle-late Miocene accretionary prism in eastern Taiwan. Tectonics. https://doi.org/10.1002/2016TC004383

Chen W-S, Yeh J-J, Syu S-J (2019) Late Cenozoic exhumation and erosion of the Taiwan orogenic belt: new insights from petrographic analysis of foreland basin sediments and thermochronological dating on the metamorphic orogenic wedge. Tectonophysics 750:56–69. https://doi.org/10.1016/j.tecto.2018.09.003

Chen C-T, Lo C-H, Wang P-L, Lin L-H (2022) Extensional mountain building along convergent plate boundary: insights from the active Taiwan mountain belt. Geology 50:1245–1249. https://doi.org/10.1130/G50311.1

Clark MB, Fisher DM, Lu C-Y (1992) Strain variations in the Eocene and older rocks exposed along the central and southern cross-island highways. Taiwan Acta Geol Taiwan 30:1–10

Conand C, Mouthereau F, Ganne J, Lin AT-S, Lafhid A, Daudet M, Mesalles L, Giletycz S, Bonzani M (2020) Strain partitioning and exhumation in Taiwan oblique collision: role of rift architecture and plate kinematics. Tectonics. https://doi.org/10.1029/2019TC005798

Craw D, Upton P, Yu B-S, Horton T, Chen Y-G (2009) Young orogenic gold mineralisation in active collisional mountains, Taiwan. Miner Depos 45:631–646

Crespi J, Chan Y-C, Swaim M (1996) Synorogenic extension and exhumation of the Taiwan hinterland. Geology 24(3):247–250
Dadson SJ, Hovius N, Chen H, Dade WB, Hsieh M-L, Willett SD, Hu J-C, Horng M-J, Chen M-C, Stark CP, Lague D, Lin J-C (2003) Links between erosion, runoff variability and seismicity in the Taiwan orogen. Nature 426:648–651
Davis WM (1899) The geographical cycle. Geogr J 14:481–504
Derrieux F, Siame L, Bourlés D, Chen R-F, Braucher R, Léanni L, Lee J-C, Chu H-T, Byrne T (2014) How fast is the denudation of the Taiwan Mountain belt? J East Asian Sci. https://doi.org/10.1016/j.jseaes.2014.03.012
Dewangga DD, Tsai C-H, Iizuka Y, Kouketsu Y, Sakaguchi IT, Chung S-L, Chen H-F (2021) Origins and metamorphism of serpentinites in the Yuli belt, eastern Taiwan. In: Geologica Society of Taiwan, Taipei
Ernst WG (1977) Olistostromes and included ophiolitic debris from the Coastal Range of eastern Taiwan. Mem Geol Soc China 2:97–114
Faure M, Lu C-Y, Chu H-T (1991) Ductile deformation and Miocene nappe-stacking in Taiwan related to motion of the Philippine Sea Plate. Tectonophysics 198:95–105
Feehan JG, Brandon MT (1999) Contribution of ductile flow to exhumation of low-temperature, high-pressure metamorphic rocks: San Juan, Cascade nappes, NW Washington State. J Geophys Res 104:10883–10902
Fitch TJ (1972) Plate convergence, transcurrent faults, and internal deformation adjacent to Southeast Asia and the Western Pacific. J Geophys Res 77(23):4432–4460
Fossen H (2010) Structural geology. Cambridge University Press, Cambridge
Fossen H, Cavalcante GCG (2017) Shear zones—a review. Earth Sci Rev 171:434–455
Fuller C, Willett SD, Fisher DM, Lu C-Y (2006) A thermomechanical wedge model of Taiwan constrained by fission-track thermochronometry. Tectonophysics 425:1–24
Grujic D, Casey M, Davidson C, Hollister LS, Kündig R (1996) Ductile extrusion of the Higher Himalayan Crystalline in Bhutan: evidence from quartz microfabrics. Tectonophysics 260:21–43
Ho CS (1986) A synthesis of the geologic evolution of Taiwan. Tectonophysics 125:1–16
Ho CS (1988) An introduction to the geology of Taiwan–explanatory text of the geologic map of Taiwan, 2nd edn. Ministry of Economic Affairs, Taipei
Ho G-R, Lo W (2015) Structural analysis in Shoufengsi area of Tananao complex, Eastern Taiwan. Terr Atmos Ocean Sci 26(5):557–569
Ho G-R, Byrne TB, Lee J-C, Mesalles L, Lin C-W, Lo W, Chang C-P (2022) A new interpretation of the metamorphic core in the Taiwan orogen: a regional-scale, left-lateral shear zone that accommodated highly oblique plate convergence in the Plio-Pleistocene. Tectonophysics 833:229332. https://doi.org/10.1016/j.tecto.2022.229332
Hsieh M-L, Hogg A, Kang S-C, Chou C-Y (2018) The preservation of last-glacial (N50 to 40 ka) colluvium on low-relief surfaces in Alishan, an actively uplifting mountain in southwestern Taiwan. Geomorphology 322:159–174. https://doi.org/10.1016/j.geomorph.2018.08.041
Hsieh AI, Dashtgard SE, Wang P-L, Horng C-S, Su C-C, Lin AT, Vaucher R, Löwemark L (2023) Multi-proxy evidence for rapidly shifting sediment sources to the Taiwan Western Foreland Basin at the Miocene-Pliocene transition. Basin Res 35(3):932–948. https://doi.org/10.1111/bre.12741
Hsu W-H, Byrne TB, Ouimet W, Lee Y-H, Chen Y-G, van Soest M, Hodges K (2016) Pleistocene onset of rapid, punctuated exhumation in the eastern Central Range of the Taiwan orogenic belt. Geology 44(9):719–722. https://doi.org/10.1130/G37914.1
Hu J-C, Yu S-B, Angelier J (2002) Transition tectonics of northern Taiwan induced by convergence and trench retreat. Geol Soc Am Spec Pap. https://doi.org/10.1130/0-8137-2358-2.147
Huang CK (1953) Adularia from Kukutzu, Taiwan. Acta Geol Taiwanica 5:27–34
Huang C, Byrne T (2014) Tectonic evolution of an active tectonostratigraphic boundary in accretionary wedge: an example from the Tulungwan-Chaochou Fault system, southern Taiwan. J Struct Geol. https://doi.org/10.1016/j.jsg.2014.06.007
Huang C-Y, Yuan P, Tsao S-J (2006) Temporal and spatial records of active arc-continent collision in Taiwan: a synthesis. Geol Soc Am Bull 118(3/4):274–288. https://doi.org/10.1130/B25527.1
Huang H-H, Wu YM, Song X, Chang C-H, Lee S-J, Chang T-M, Hsieh H-H (2014) Joint Vp and Vs tomography of Taiwan: implications for subduction-collision orogeny. Earth Planet Sci Lett 392:177–191. https://doi.org/10.1016/j.epsl.2014.02.026
Huang P, Wei C, Dong J, Zhang J (2023) Two-stage exhumation of high–P rocks from the Yuli Belt, Eastern Taiwan: insights from the metamorphic evolution in subduction channels. Lithos 440–441:107056. https://doi.org/10.1016/j.lithos.2023.107056
Jahn BM, Liou JG, Nagasawa H (1981) High-pressure metamorphic rocks of Taiwan: REE geochemistry, Rb–Sr ages and tectonic implications. Mem Geol Soc China 4:497–520
Jiao ZH (1991) The geologic structure and evolution of the hoping area in Eastern Taiwan. National Taiwan University, Taipei
Keyser W, Tsai CH, Iizuka Y, Oberhänsli R, Ernst WG (2016) High-pressure metamorphism in the Chinshuichi area, Yuli belt, eastern Taiwan. Tectonophysics 692:191–202
Kirstein L, Fellin M, Willett S, Carter A, Chen Y-G, Garver J, Lee D (2009) Pliocene onset of rapid exhumation in Taiwan during arc-continent collision: new insights from detrital thermochronometry. Basin Res 22:270–285. https://doi.org/10.1111/j.1365-2117.2009.00426.x
Korren C, Ferre E, Yeh E-C, Chou Y-M, Chu H-T (2017) Seismic rupture parameters deduced from a pliocene-pleistocene fault pseudotachylyte in Taiwan. In: Thomas MY, Mitchell TM, Bhat HS (eds) Fault zone dynamic processes: evolution of fault properties during seismic rupture, vol Geophysical Monograph 227. Wiley, New York, pp 21–35
Kouketsu Y, Tsai CH, Enami M (2019) Discovery of unusual metamorphic temperatures in the Yuli belt, eastern Taiwan: new interpretation of data by Raman carbonaceous material geothermometry. Geology 47(6):522–526. https://doi.org/10.1130/G45934.1
Kuiper KF, Deino A, Hilgen FJ, Krijgsman W, Renne PR, Wijbrans AJ (2008) Synchronizing rock clocks of Earth history. Science 320(5875):500–504
Lallemand S, Liu C-S, Dominguez S, Schnürle P, Malavieille J, Crew AS (1999) Trench-parallel stretching and folding of forearc basins and lateral migration of the accretionary wedge in the southern Ryukyus: a case of strain partition caused by oblique convergence. Tectonics 18(2):231–247
Lallemand S, Theunissen T, Schnürle P, Lee C-S, Liu C-S, Font Y (2013) Indentation of the Philippine Sea plate by the Eurasia plate in Taiwan: details from recent marine seismological experiments. Tectonophysics. https://doi.org/10.1016/j.tecto.2013.03.020
Lan C-Y, Liou JG (1981) Occurrence, petrology and tectonics of serpentinites and their associated rodingites in the Central Range, Taiwan. Mem Geol Soc China 4:343–389
Lan C-Y, Liou JG (1984) Mineral chemistry of metamorphosed ocean rocks in the Yuli belt of the Tananao schist. Taiwan Mem Geol Soc China 6:153–179
Lee Y-H (1995) A study of the stress field system evolution of the Taiwan mountain belt, Central Cross-Island Highway and surrounding areas. Trans Cent Geol Surv, MOEA, Taiwan 10:51–89
Lee C-T, Wang Y (1988) Quaternary stress changes in northern Taiwan and their tectonic implication. Proc Geol Soc China 31:154–168
Lee Y-H, Yang CN (1994) Structural evolution in the Tayulin area of the central range. Bull Cent Geol Surv 9:77–106
Lee JY, Marti K, Severinghaus JP, Kawamura K, Yoo HS, Lee JB, Kim JS (2006) A redetermination of the isotopic abundances of atmospheric Ar. Geochim Cosomochim Acta 70(17):4507–4512
Lee Y-H, Byrne T, Lo W, Wang S-J, Tsao S-J, Chen C-H (2022a) Out of sequence faulting in backbone range and its implication to exhumation process of the Taiwan Orogen. In: Japan Geosciences Union/American Geophysical Union, Chiba, Japan (hybrid). vol SIT20-10. Japan Geosciences Union
Lee Y-H, Byrne TB, Lo W, Wang S-J, Tsao S-J, Chen C-H, Yu H-C, Tan X, van Soest M, Hodges K, Mesalles L, Robinson H, Fosdick JC (2022b) Out of sequence faulting in the backbone range, Taiwan: implications for thickening and exhumation processes. Earth Planet Sci Lett 594:117711. https://doi.org/10.1016/j.epsl.2022.117711
Lewis JC, O'Hara DJ, Rau R-J (2015) Seismogenic strain across the transition from fore-arc slivering to collision in southern Taiwan. J Geophys Res: Solid Earth 120(6):4539–4555. https://doi.org/10.1002/2015JB011906
Lin C-C (1957) Topography of Taiwan. Publication of the Taiwan Provincial Documentary Committee, Taipei (**in Chinese**)

Lin M-L (1999a) Existence of the Chouochi transverse fault reconfirmed in southeastern Taiwan and its tectonic implication. J Geol Soc China 42(1):69–84
Lin M-L (1999b) Litho-Stratigraphy and structural geology of the Wanjung area, eastern Taiwan and their tectonic implications. J Geol Soc China 42(2):247–267
Lin CW, Chen W-S (2016) Geololgic map of Taiwan. Geological Society of Taiwan, Taiiwan
Lin M-L, Yang CN, Wang Y (1984) Petrotectonic study on the Yuli Belt of the Tananao Schist in the Chinshuichi area, Eastern Taiwan. Acta Geol Taiwan 22:151–188
Liou JG (1981) Petrology of metamorphosed oceanic rocks in the Central Range of Taiwan. Mem Geol Soc China 4:281–342
Liou JG, Lan CY, Suppe J, G. EW, (1977) The East Taiwan Ophiolite, its occurrence, petrology, metamorphism and tectonic setting. Min Res Serv Organ Spec Rep 1:212p
Liu T-K (1982) Tectonic implication of fission track ages from the Central Range, Taiwan. Proc Geol Soc China 25:22–37
Liu T-K, Hsieh S, Chen Y-G, Chen W-S (2001) Thermo-kinematic evolution of the Taiwan oblique-collision mountain belt as revealed by zircon fission track dating. Earth Planet Sci Lett 186:45–56
Liu YC, Chen PT, Huang C, Yen IC, Lu ST (2009) Resent survey results of Chaochou fault. Annu Rep Cent Geol Surv 2008:35–36
Lo C-H, Onstott TC (1995) Rejuvenation of K-Ar systems for minerals in the Taiwan Mountain Belt. Earth Planet Sci Lett 131:71–98
Lo C-H, Yui T-F (1996) 40Ar/39Ar dating of high-pressure rocks in the Tananao basement complex, Taiwan. J Geol Soc China 39:13–30
Lo Y-C, Chen C-T, Lo C-H, Chung S-L (2020) Ages of ophiolitic rocks along plate suture in Taiwan orogen: fate of the South China Sea from subduction to collision. Terr Atmos Ocean Sci 31:383–402. https://doi.org/10.3319/TAO.2019.06.19.01
Lu C-Y, Lee J-C (2001) Structural evolution of the southeastern Central Range, Taiwan. West Pac Earth Sci 1(2):213–226
Lu C-Y, Wang Lee C (1986) The sheath folds in the Tananao group between Tienshiang and Tailuko, east-west cross-island highway, Taiwan. Tectonophysics 125(1):125–131. https://doi.org/10.1016/0040-1951(86)90010-7
Ludwig KR (2003) User's manual for isoplot 3.00: a geochronological toolkit for microsoft excel
Malavieille J (2010) Impact of erosion, sedimentation, and structural heritage on the structure and kinematics of orogenic wedges: analog models and case studies. GSA Today. https://doi.org/10.1130/GSATG48A.1
Malavieille J, Trullenque G (2009) Consequences of continental subduction on forearc basin and accretionary wedge deformation in SE Taiwan: insights from analogue modeling. Tectonophysics 466(3–4):377–394. https://doi.org/10.1016/j.tecto.2007.11.016
Mann P, Gordon MB (1996) Tectonic uplift of blueschist belts along transpressional strike-slip faults. In: Bebout GE, Scholl DW, Kirby SH, Platt JP (eds) Subduction top to bottom, vol 96. Am. Geo. U. Geophys. Monograph, 96 edn. AGU, pp 143–154
McCaffrey R (1992) Oblique plate convergence, slip vectors, and forearc deformation. J Geophys Res 97(B6):8905–8915
Mccaffrey R (2002) Crustal block rotations and plate coupling. In: Plate boundary zones, pp 101–122. https://doi.org/10.1029/GD030p0101
Mesalles L (2014) Mountain building at a subduction-collision transition zone, Taiwan: insights from morphostructural analysis and thermochronological dating. Université Pierre et Marie Curie - Paris VI, Creative Commons, Paris
Mesalles L, Mouthereau F, Bernet M, Chang C-P, Tien-Shun Lin A, Fillon C, Sengelen X (2014) From submarine continental accretion to arc-continent orogenic evolution: the thermal record in southern Taiwan. Geology 42(10):907–910. https://doi.org/10.1130/g35854.1
Mesalles L, Lee Y-H, Ma T-C, Tsai W-L, Tan X-B, Lee H-Y (2020) A Late-Miocene Yuli belt? New constraints on the eastern Central Range depositional ages. Terr Atmos Ocean Sci 31(4):403–414. https://doi.org/10.3319/TAO.2019.06.24.01
Min K, Mundil R, Renne PR, Ludwig KR (2000) A test for systematic errors in 40Ar/39Ar geochronology through comparison with U/Pb analysis of a 1.1-Ga rhyolite. Geochim Cosomochim Acta 64(1):73–98
Mondro C, Fisher D, Yeh E-C (2017) Strain histories from the eastern Central Range of Taiwan: a record of advection through a collisional orogen. Tectonophysics. https://doi.org/10.1016/j.tecto.2017.03.007
Osozawa S, Shinjo R, Armid A, Watanabe Y, Horiguchi T, Wakabayashi J (2012) Palaeogeographic reconstruction of the 1.55 Ma synchronous isolation of the Ryukyu Islands, Japan, and Taiwan and inflow of the Kuroshio warm current. Int Geol Rev 54(12):1369–1388. https://doi.org/10.1080/00206814.2011.639954
Ouimet W, Byrne T, Siame L, Bierman P, Rood DH (2013) Slow erosion rates, increasing relief and transient landscape evolution within the Central Range of Taiwan. In: Fall Meeting. American Geophysical Union, San Francisco
Page BM, Suppe J (1981) The Pliocene Lichi melange in Taiwan: its plate tectonic and olistostromal origin. Am J Sci 281:193–227
Passchier C, Trouw RAJ (2005) Microtectonics, 2nd edn. Springer, Berlin. https://doi.org/10.1007/3-540-29359-0
Pelletier B, Hu HN (1984) New structural data along two transects across the southern half of the Central Range of Taiwan. Mem Geol Soc China 6:1–19
Platt JP (1983) Progressive refolding in ductile shear zones. J Struct Geol 5(6):619–622
Platt JP (1993) Exhumation of high-pressure rocks: a review of concepts and processes. Terra Nova 5(2):119–133. https://doi.org/10.1111/j.1365-3121.1993.tb00237.x
Platt JP, Soto J-I, Whitehouse MJ, Hurford AJ, Kelley SP (1998) Thermal evolution, rate of exhumation, and tectonic significance of metamorphic rocks from the floor of the Alboran extensional basin, western Mediterranean. Tectonics 17(5):671–689. https://doi.org/10.1029/98TC02204
Pulver MH, Crespi JM, Byrne TB (2002) Lateral extrusion in a transpressional collisional zone: an example from the pre-Tertiary metamorphic basement of Taiwan. In: Byrne TB, Liu C-S (eds) Geology and geophysics of an arc-continent collision, Taiwan. Geological Society of America, Special Paper 358, pp 107–120
Ramsay JG (1980) The crack-seal mechanism of rock deformation. Nature 284:135–139
Rau R-J, Ching K-E, Hu J-C, Lee J-C (2008) Crustal deformation and block kinematics in transition from collision to subduction: GPS measurements in northern Taiwan, 1995–2005. J Geophys Res. https://doi.org/10.1029/2007JB005414
Ring U, Brandon M (1999) Ductile deformation and mass loss in the Franciscan Subduction Complex: implications for exhumation processes in accretionary wedges. In: Ring U, Brandon M, Lister G, Willett S (eds) Exhumation proceses: normal faulting, ductile flow and erosion, vol 154. Geological Society of London, London, pp 55–86
Ring U, Kumerics C (2008) Vertical ductile thinning and its contribution to the exhumation of high-pressure rock: the Cycladic blueschist unit in the Aegean. J Geol Soc Lond 165:1019–1030. https://doi.org/10.1144/0016-76492008-010
Ring U, Brandon MT, Lister G, Willett S (1999) Exhumation processes: normal faulting, ductile flow and erosion. Special Publication, vol 154. Geological Society of London, London
Rutte D, Becker TA, Deino AL, Reese SR, Renne PR, Schickler RA (2018) The new CLOCIT irradiation facility for 40Ar/39Ar geochronology: characterisation, comparison with CLICIT and implications for high-precision geochronology. Geostand Geoanal Res 42(3):301–307
Sandmann S, Nagel HJ, Froitzheim N, Ustaszewski K, Münker C (2015) Late miocene to early pliocene blueschist from Taiwan and its exhumation via forearc extraction. Terra Nova 27:285–291. https://doi.org/10.1111/ter.12158
Secor DT (1965) Role of fluid pressure in jointing. Am J Sci 263:633–646
Shan Y, Nie G, Ni Y, Chang C-P (2014) Structural analysis of a newly emerged accretionary prism along the Jinlun-Taimali coast, southeastern Taiwan: from subduction to arc-continent collision. J Struct Geol 66:248–260. https://doi.org/10.1016/j.jsg.2014.06.002
Shen T-T, Liu T-K, Huang S-Y, Hsieh P-S, Wu C-Y (2020) Post-collisional exhumation and geotherm pattern in northern Tananao Complex, northeastern Taiwan. Terr Atmos Ocean Sci 31:369–381. https://doi.org/10.3319/TAO.2019.04.06.01
Shepherd TJ, Rankin AH, Alderton DHM (1985) A practical guide to fluid inclusion studies. Blackie, Barcelona

Shyu B, Sieh K (2005) Neotectonic architecture of Taiwan and its implications for future large earthquakes. J Geophys Res. https://doi.org/10.1029/2004JB003251
Sibuet J-C, Hsu S-K, Shyu C-T, Liu C-S (1995) Structural and kinematic evolutions of the okinawa trough backarc basin. In: Taylor B (ed) Backarc basins: tectonics and magmatism. Springer, Boston, pp 343–379. https://doi.org/10.1007/978-1-4615-1843-3_9
Sibuet J-C, Deffontaines B, Hsu S-K, Thareau N, Le Formal J-P, Liu C-S (1998) Okinawa trough backarc basin: early tectonic and magmatic evolution. J Geophys Res: Solid Earth 103(B12):30245–30267. https://doi.org/10.1029/98JB01823
Sibuet J-C, Zhao M, Wu J, Lee C-S (2021) Geodynamic and plate kinematic context of South China Sea subduction during Okinawa trough opening and Taiwan orogeny. Tectonophysics 817:229050. https://doi.org/10.1016/j.tecto.2021.229050
Simoes M, Beyssac O, Chen Y-G (2012) Late Cenozoic metamorphism and mountain building 1 in Taiwan: a review. J Asian Earth Sci 46:92–119
Stanley RS, Hill AB, Chang HC, Hu HN (1981) A transect through the metamorphic core of the Central Mountains, southern Taiwan. Mem Geol Soc China 4:443–473
Stoenner RW, Schaeffer OA, Katcoff S (1965) Half-lives of argon-37, argon-39, and argon-42. Science 148(3685):1325–1328
Suppe J (1981) Mechanics of mountain building and metamorphism in Taiwan. Mem Geol Soc China 4:67–89
Suppe J (1984) Kinematics of arc-continent collision, flipping of subduction and back-arc spreading near Taiwan. Mem Geol Soc China 6:21–33
Tan LP, Wang Lee C, Chen CC, Tien PL, Tsui PC, Yui TF (1978) A mineralogical study of the Fengtien nephrite deposits of Hualien: Taiwan. Natl Sci Counc Spec Publ 1:81
Teng LS (1990) Geotectonic evolution of late Cenozoic arc-continent collision in Taiwan. Tectonophysics 183:57–76
Teng LS, Lee C-T, Peng C-H, Chen W-F, Chu C-J (2001) Origin and geological evolution of the Taipei Basin, northern Taiwan. West Pac Earth Sci 1(2):115–142
Tobisch OT, Paterson SR (1988) Analysis and interpretation of composite foliations in areas of progressive deformation. J Struct Geol 10(7):745–754. https://doi.org/10.1016/0191-8141(88)90081-8
Touret JLR (2001) Fluids in metamorphic rocks. Lithos 55:1–25
Tsai C-H, Iizuka Y, Ernst WG (2013) Diverse mineral compositions, textures, and metamorphic P-T conditions of the glaucophane-bearing rocks in the Tamayen mélange, Yuli belt, eastern Taiwan. J Asian Earth Sci 63:218–233. https://doi.org/10.1016/j.jseaes.2012.09.019
Usami M, Matsumoto T (1940) Geologic map of Taiwan: Daibuzan Sheet. Bureau of Produce Industry, Government Gen, Taiwan
Ustaszewski K, Wu Y-M, Suppe J, Huang H-H, Chang C-H, Carena S (2012) Crust–mantle boundaries in the Taiwan–Luzon arc-continent collision system determined from local earthquake tomography and 1D models: Implications for the mode of subduction polarity reversal. Tectonophysics 578:31–49. https://doi.org/10.1016/j.tecto.2011.12.029
Van Avendonk HJA, McIntosh KD, Kuo-Chen H, Lavier LL, Okaya DA, Wu FT, Wang C-Y, Lee C-S, Liu C-S (2015) A lithospheric profile across northern Taiwan: from arc-continent collision to extension. Geophys J Int 204(1):331–346. https://doi.org/10.1093/gji/ggv468
von Hagke C, Philippon M, Avouac JP, Gurnis M (2016) Origin and time evolution of subduction polarity reversal from plate kinematics of Southeast Asia. Geology 44(8):659–662. https://doi.org/10.1130/G37821.1
Wang PL (1998) K-feldspar40Ar/39Ar thermochronology and its applications. National Taiwan University, Taipei
Wang PL, Lin LH, Lo CH (1998) 40Ar/39Ar dating of mylonitization in the Tanano Schist, eastern Taiwan. J Geol Soc China 159–183:1
Wang Lee C (1979) Preliminary notes on the time relations of metamorphic rocks, Loshao–Tailuko area, eastern Taiwan. Mem Geol Soc China 3:249–252
Wang Lee C, Lu C-Y (1984) Field trip guide to the eastern section of the Cross Island Highway. In: Paper presented at the Field guidebook for the Sino-French Colloquium on Geodynamics of the Eurasian-Philippine Sea Plate Boundary, Taiwan
Warren CJ (2013) Exhumation of (ultra-)high-pressure terranes: concepts and mechanisms. Solid Earth 4:75–92. https://doi.org/10.5194/se-4-75-2013
Warren CJ, Beaumont C, Jamieson RA (2008) Deep subduction and rapid exhumation: role of crustal strength and strain weakening in continental subduction and ultrahigh-pressure rock exhumation. Tectonics. https://doi.org/10.1029/2008TC002292
Wei K-Y, Chen Y-G, Liu T-K (1998) Sedimentary history of the Taipei Basin with constraints from thermoluminescence dates. J Geol Soc China 41:109–125
Whipple KX, DiBiase RA, Ouimet WB, Forte AM (2017) Preservation or piracy: diagnosing low-relief, high-elevation surface formation mechanisms. Geology 45:91–94. https://doi.org/10.1130/G38490.1
Willett S, Fisher DM, Fuller C, Yeh E-C, Lu C-Y (2003) Erosion rates and orogenic-wedge kinematics in Taiwan inferred from fission-track thermochronometry. Geology 31(11):945–948
Wu J, Suppe J, Lu R, Kanda R (2016) Philippine Sea and East Asian plate tectonics since 52 Ma constrained by new subducted slab reconstruction methods. J Geophys Res. https://doi.org/10.1002/2016JB012923
Yang GS (1986) A geomorphological study of active faults in Taiwan–especially on the relation between active faults and geomorphic surfaces. Chinese Culture University, Taipei
Yang CN, Wang Y (1985) Petrotectonic study on the Yuli blet of the Tananao schist in the Juisui area. East Taiwan Acta Geol Taiwanica 23:153–180
Yang R, Willett SD, Goren L (2015) In situ low-relief landscape formation as a result of river network disruption. Nature 520:526–529
Yeh E-C, Wu Y-M, Shyu JBH, Chang C-H (2016) Tectonic implication of the 5th March 2005, doublet earthquake in Ilan, Taiwan. Terr Atmos Ocean Sci 27:799–805
Yen TP (1963) The metamorphic belts within the Tananao schist terrain of Taiwan. Proc Geol Soc China 6:72–74
Yen TP (1970) Structural analysis of the Slate Formation of Taiwan. Bull Geol Surv Taiwan 21:1–54
Yen TP (1983) Late Cenozoic faulting in the Juisui area, eastern Taiwan. Bull Inst Earth Sci Acad Sin 3:149–154
Yi D, Cheng ZY, Lin CW (2012) The geological sheet map "Guangfu," scale 1:50,000, and its explanatory text. Central Geological Survey, MOEA, New Taipei City
Yi D-C, Lin C-W, McAleer R, Kunk M, Wintsch R (2015) Exhumation of Metamorphic rocks during the Taiwan Orogeny: A Study on the Soufeng Fault. In: American Geophysical Union Fall Meeting. American Geophysical Union, San Francisco
Yui TF, Lu C-Y, Lo CH (1990) Tectonic evolution of the Tananao Schist Complex of Taiwan. In: Aubouin J, Bourgois J (eds) Tectonics of circum-Pacific continental margins. VSP, Utrecht, pp 193–209
Yui T-F, Huang FE, Xu J (1996) Raman spectrum of carbonaceous material a possible metamorphic grade indicator for low-grade metamorphic rocks. J Metamorph Geol 14:115–124
Yui TF, Okamoto K, Usuki T, Lan CY, Chu HT, Liou JG (2009) Late Triassic-Late Cretaceous accretion/subduction in the Taiwan region along the eastern margin of South China—evidence from zircon SHRIMP dating. Int Geol Rev 51(4):304–328. https://doi.org/10.1080/00206810802636369
Yui TF, Maki K, Lan CY, Hirata T, Chu HT, Kon Y, Yokoyama TD, Jahn BM, Ernst WG (2012) Detrital zircons from the Tananao metamorphic complex of Taiwan: implications for sediment provenance and Mesozoic tectonics. Tectonophysics 541–543:31–42. https://doi.org/10.1016/j.tecto.2012.03.013
Yui T-F, Usuki T, Chen C-Y, Ishida A, Sano Y, Suga K, Iizuka Y, Chen C-T (2014) Dating thin zircon rims by NanoSIMS: the Fengtien nephrite (Taiwan) is the youngest jade on Earth. Int Geol Rev 56(16):1932–1944. https://doi.org/10.1080/00206814.2014.972994
Zhang R, Li S, Suo Y, Liu J, Cao X, Zhou J, Jiang Z, Li X (2022) A forearc pull-apart basin under oblique arc-continent collision: insights from the North Luzon Trough. Tectonophysics 837:229461. https://doi.org/10.1016/j.tecto.2022.229461

Publisher's Note